Faculty of Physics and Astronomy

University of Heidelberg

Diploma thesis

in Physics

submitted by

Sabrina Ludmann

born in Quakenbrück

January 2007

Aircraft Based Measurements of Sulfur Dioxide Pollution Plumes in the Free Troposphere

This diploma thesis has been carried out by Sabrina Ludmann at the
Max-Planck-Institute for Nuclear Physics, Heidelberg
(Atmospheric physics division)
under supervision of
Prof. Dr. Frank Arnold

Aircraft Based Measurements of Sulfur Dioxide Pollution Plumes in the Free Troposphere

Sulfur dioxide pollution plumes have been investigated in the free troposphere onboard a research aircraft, using Chemical Ionization Mass Spectrometry (CIMS). The measurements have been carried out during the MEGAPLUME campaign in spring 2006 at the German Aerospace Center (DLR, Oberpfaffenhofen, Germany), and during the international African Monsoon Multidisciplinary Analysis (AMMA) campaign in August 2006 in West Africa (Ouagadougou, Burkina Faso). Sulfur dioxide is an important precursor gas of sulfuric acid which strongly contributes to aerosol formation. Aerosol particles directly and indirectly affect our climate in various ways.

Two different pollution plumes will be discussed in this work: a plume from Southeast Asia that had reached Europe after crossing the Pacific and Atlantic ocean, and an extended biomass burning layer off the coast of Ghana. The upward transport of sulfur dioxide in large convective thunderstorms during the African Monsoon has been investigated as another part of the AMMA campaign.

Fluggestützte Messungen von Schwefeldioxid-Verschmutzungsplumes in der freien Troposphäre

Schwefeldioxidverschmutzungen in der freien Troposphäre wurden mit chemischer Ionisations-Massenspektrometrie (CIMS) anhand von flugzeuggestützten Messungen untersucht. Die Messungen waren Teil der MEGAPLUME Kampagne im Frühjahr 2006 , die am Deutschen Zentrum für Luft- und Raumfahrt (DLR, Oberpfaffenhofen) durchgeführt wurde, sowie der Kampagne Afrikanischer Monsun – Multidisziplinäre Analyse (AMMA) im August 2006 in Westafrika (Ouagadougou, Burkina Faso). Schwefeldioxid ist ein wichtiges Vorläufergas für Schwefelsäure, die wiederum stark zur Bildung von Aerosolpartikeln beiträgt. Aerosolpartikel beeinflussen unser Klima direkt und indirekt auf vielfältige Weise.

Zwei unterschiedliche Verschmutzungsplumes werden in dieser Arbeit untersucht: eine Verschmutzung, die von Südostasien über den Pazifik und Atlantik nach Europa gelangte, und eine ausgedehnte Schicht von Verschmutzung aus Biomassenverbrennung vor der Küste Ghanas. Als weiterer Teil der AMMA Kampagne wurde der Vertikaltransport von Schwefeldioxid in konvektiven Gewittern während des Afrikanischen Monsuns untersucht.

Contents

Chapter 1

Introduction

Our climate is not only influenced by greenhouse gases but also by small particles in the atmosphere. These so-called aerosol particles enter the atmosphere directly as dust, soot and sea salt particles, or they are formed by nucleation of atmospheric gases. Aerosol particles influence the radiation budget of the Earth directly by scattering sunlight back into space, or they influence the cloud cover of the planet and thus change the surface and albedo properties. The effects on cloud properties include changes of the size and number concentration of cloud droplets, and modifications of the cloud lifetime and precipitation characteristics.

A very important aerosol precursor gas is sulfuric acid (H_2SO_4), which nucleates easily due to its low saturation vapor pressure. A sufficient supersaturation of H_2SO_4 is reached at low concentrations, especially in the cold free troposphere. This nucleation involves water vapor and (if available) ammonia. In the case of large numbers of pre-existent aerosol particles, H_2SO_4 condensates onto their surfaces, contributes to their growth and changes their physical and chemical properties. Both, nucleation and condensation, lead to the formation of cloud condensation nuclei and affect the properties of clouds in sulfur-polluted areas. The removal of sulfuric acid by precipitation is commonly known as acid rain.

Aerosol particles arise from pollution in the planetary boundary layer — in cities or industrial regions — and affect human health when they are inhaled. The particles can damage the sensitive lung tissue after inhalation if they are acidic, and they can transport carcinogenic substances into the bloodstream and cells.

Gaseous sulfur compounds are emitted into the atmosphere from a variety of sources. Biological processes that emit sulfur gases include anaerobic bacteria and oceanic plankton. The strongest natural source is volcanism which mostly emits sulfur dioxide (SO_2) and hydrogen sulfide. Combustion processes are the overall most important contributor of sulfur components. These emissions, from fossil fuel combustion and to a smaller part from biomass burning, are mainly anthropogenic and release large amounts of SO_2 into the atmosphere.

Sulfur dioxide is an important precursor gas for H_2SO_4. Most reduced sulfur components are oxidized to SO_2 and further to H_2SO_4 or sulfate before being removed from the atmosphere. The residence time of SO_2 in the free troposphere is limited by oxidation processes and uptake in droplets and aerosol. An average SO_2 lifetime of about a week (due to oxidation) allows the transport over long distances and the distribution of SO_2 pollution on a global scale.

Our group has mainly been concerned with the measurement of SO_2 during the research campaigns that will be described in chapters 4 and 5. This special interest is due to the importance of SO_2 for the formation of H_2SO_4. The mechanisms for this oxidation will be discussed in chapter 2. Other topics of this chapter are the atmospheric sulfur cycle and climate effects of aerosol.

The measurements involved an aircraft-borne ion trap mass spectrometer. The instrument was employed onboard the research aircraft *Falcon* which is operated by the German Aerospace Centre (Deutsches Zentrum für Luft- und Raumfahrt — DLR) in Oberpfaffenhofen, Germany. The detection method of Chemical Ionization Mass Spectrometry (CIMS) and the instrumental setup will be described in chapter 3. The data discussed in this work concentrate on SO_2 pollution events in the free troposphere at altitudes of up to 12 km.

Chapter 4 is concerned with a pollution plume that experienced transport from Southeast Asia across the Pacific, North America and the Atlantic before reaching Europe during the spring 2006 MEGAPLUME campaign. A different pollution plume from biomass burning was encountered during the African Monsoon Multidisciplinary Analysis (AMMA) campaign which is the topic of chapter 5. An extended pollution layer off the coast of Ghana in West Africa displayed a strong SO_2 pollution from biomass burning.

The upward transport of trace gases like SO_2 in Mesoscale Convective Systems (MCS) during the African monsoon was also investigated as part of the AMMA campaign. The results of these measurements will be discussed in chapter 5.

Chapter 2

Sulfur and Aerosol Particles in the Atmosphere

A very dynamic part of our environment is the atmosphere which contains our weather and climate and affects human health, as well as we have affected our environment by interfering with its complex dynamic processes. The anthropogenic influence on the atmosphere has increased rapidly since the industrial revolution which started at the end of the 18th century. The fossil fuel that we are using as primary energy source today is a natural deposit of micro-biologically decomposed organic matter and contains the sulfur that prehistoric plants and micro-organisms had incorporated in their cells.

One of the major issues in climate change is the anthropogenic greenhouse effect. It adds to the natural greenhouse effect that increases the Earth´s average temperature by about 15°C and thus allowed the formation of life on our planet. Trace gases, of which CO_2 is only one important representative, show vibrational modes in the energy range of infrared radiation (asymmetric stretching and bending at wavelenghts of roughly $4\,\mu$m and $15\,\mu$m for CO_2), absorbing and emitting the Earth´s heat radiation that would otherwise escape into space.

Anthropogenic emissions do not only include gases of different quantities but also a variety of small particles that take part in atmospheric processes. These so-called aerosol particles and their physical and chemical properties play an important role in our climate. Therefore their properties and impact need to be further investigated to gain a better understanding of meteorological processes and to improve models and predictions concerning our weather and global climate change. Aerosol particles increase the Earth´s albedo by reflecting sunlight and create a cooling effect that counteracts the greenhouse effect. The albedo is the relative reflectivity of a planet as seen from space [Roedel, 1994]. (For climate effects see section 2.2.3).

The formation of new particles and their growth is strongly influenced by the atmospheric sulfur content, though trace gases containing sulfur have typical low mole fractions of less than 1 ppbv[1]. Sulfur dioxide is the most important precursor of atmospheric gaseous sulfuric acid, which condenses and nucleates easily due to its low saturation vapor pressure and thus leads to the formation of aerosol particles (see sections 2.2.1 and 2.2.2).

A visible and therefore more obvious candidate for influencing the climate is the cloud cover of our planet, adding its effect to those of trace gases and aerosol particles. Clouds cover roughly 50 % of the Earth´s surface [Zhao et al., 2006] and may have a cooling or warming effect on climate, depending on cloud type and altitude. They increase the planet´s albedo but also act as a warming blanket over the surface by reflecting heat radiation back to the ground. The influence of atmospheric sulfur on clouds is described in section 2.2. The climate effects of aerosol and clouds will be discussed in section 2.2.3.

2.1 Sources of Sulfur Dioxide in the Atmosphere

Anthropogenic sulfur mainly enters the atmosphere through biomass burning and fossil fuel combustion. Additionally there are natural sources such as volcanic activity or biological processes. Either sulfur dioxide (SO_2, containing sulfur in the oxidation state S(+IV)) is released directly by these anthropogenic or natural sources, or other reduced sulfur components (oxidation states as low as S(-II), e.g. sulfides like DMS and H_2S) undergo oxidation and chemical conversion to SO_2. Sulfur dioxide is a major intermediate in sulfuric acid (H_2SO_4) formation.

---

[1] ppmv = parts per million (volume) = 10^{-6}= 1 μl/l
ppbv = parts per billion (volume) = 10^{-9}= 1 nl/l
pptv = parts per trillion (volume) = 10^{-12}= 1 pl/l
ppqv = parts per quadrillion (volume) = 10^{-15}= 1 fl/l

H_2SO_4 strongly contributes to aerosol formation and growth. Deposition of sulfur and thus removal from the atmosphere mostly happens in the form of sulfate (SO_4^{2-}) aerosol, where sulfur has the highest oxidation state S(+VI). While the emissions of sulfur generally include reduced gaseous species, deposition mostly occurs in the oxidized form S(+VI).

An overview of the atmospheric sulfur cycle with the most important sulfur species and their pathways is given in **figure 2.1**. The paths of sulfur components from their source to their conversion or removal are denoted by arrows. The arrow label numbers denoting the different steps are explained in the following text.

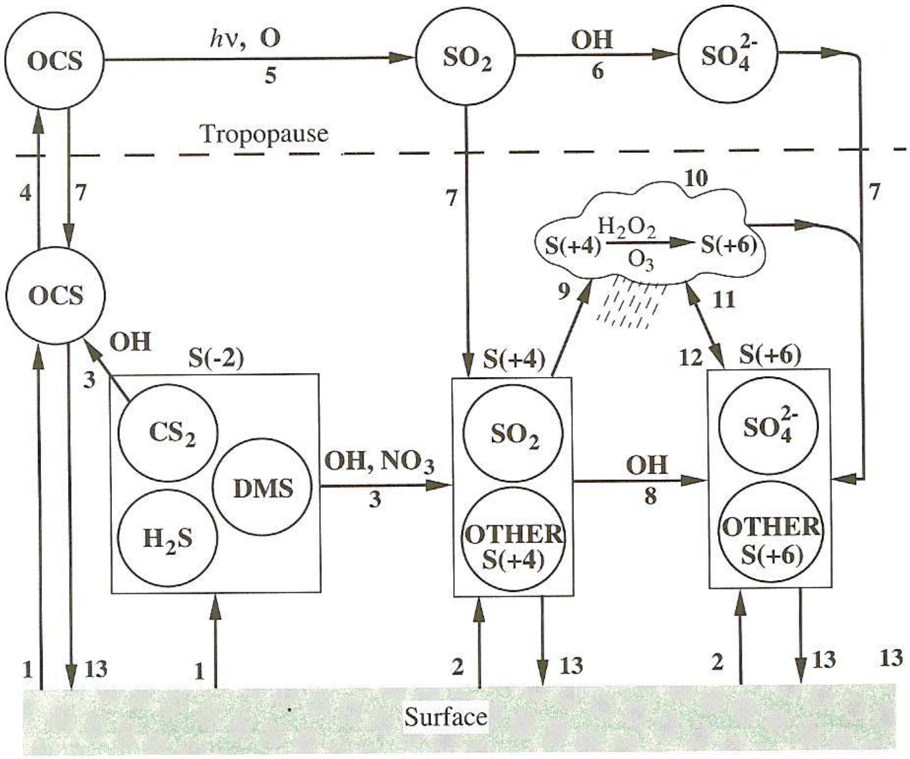

Figure 2.1: A schematic view of the major atmospheric sulfur components and their reaction paths in the atmospheric sulfur cycle. The arrow labels are explained in the text below. Numbers like S(+4) denote the oxidation state. "Surface" represents all surface related sources and sinks of the displayed sulfur species, e.g. industry, vegetation and ocean. Figure and statements (1)–(13) taken from [Berresheim et al., 1995] if not denoted differently.

(1) The surface emits reduced sulfur species such as dimethyl sulfide (DMS, $(CH_3)_2S$), hydrogen sulfide (H_2S), carbon disulfide (CS_2), and carbonyl sulfide (OCS). DMS originates mainly from the ocean and from vegetation processes and is further described in section 2.1.1. H_2S has a major source in anaerobic processes in wetlands (tidal flats, coastal wetlands, swamp regions) as well as in volcanic activity. It is also emitted from biomass burning and vegetation activity. An anthropogenic source of H_2S is the paper and cellulose industry. CS_2 and OCS are emission products from vegetation and oceans. Another source of CS_2 are industrial processes, OCS also originates from biomass burning [Brasseur et al., 1999]. (See table 2.1 for emission sources.)

(2) Sulfur of higher oxidation states (S(+IV) and S(+VI)) is mostly emitted in the form of SO_2 and H_2SO_4. A major direct emission source of these components is fossil fuel combustion, but SO_2 also originates from biomass burning or biofuel combustion, smeltering works and volcanism.

(3) The reduced sulfur species DMS, H_2S and CS_2 undergo oxidation by the hydroxyl radical (OH) in the troposphere. OH chemistry is discussed in section 2.2.1. DMS is also oxidized by nitrogen trioxide (NO_3) at night when OH chemistry ceases. The major oxidation product in both cases is SO_2. CS_2 reacts with OH (reaction 2.6) and hereby acts as the major chemical source of OCS, a species with a long lifetime due to its low reactivity.

(4) OCS experiences transport to the stratosphere, where an environment that allows its decomposition is given. The input of OCS in the stratosphere is considered responsible for the maintainance of the stratospheric sulfate aerosol layer [Brasseur et al., 1999].
(see section 2.2.3)

(5) OCS in the stratosphere is either photolysed by solar radiation or it reacts with an oxygen atom $O(^3P)$ to form SO_2 [Berresheim et al., 1995]. Oxygen atoms originate from oxygen molecules (O_2) or ozone (O_3) through photolytic processes in these altitudes [Seinfeld and Pandis, 1998, Brasseur et al., 1999] (see reaction 2.16 in section 2.2.1 for ozone photolysis). OCS is an important source of stratospheric SO_2 and undergoes the following reactions:

$$OCS + h\nu \longrightarrow CO + S \quad , \lambda < 388\,\text{nm}, (71\,\%) \tag{2.1}$$

$$OCS + O \longrightarrow CO + SO \quad , k = 1.6 \cdot 10^{-11} \exp\,(-2150/T)\ \text{cm}^3\ \text{s}^{-1}, (22\,\%) \tag{2.2}$$

$$OCS + \cdot OH \longrightarrow CO_2 + HS \quad , k \approx 2 \cdot 10^{-15}\ \text{cm}^3\ \text{s}^{-1}, (7\,\%) \tag{2.3}$$

$$S + O_2 \longrightarrow SO + O \quad , k = 2.1 \cdot 10^{-12}\ \text{cm}^3\ \text{s}^{-1} \tag{2.4}$$

$$SO + O_2 \longrightarrow SO_2 + O \quad , k = 1.4 \cdot 10^{-13} \exp\,(-2280/T)\ \text{cm}^3\ \text{s}^{-1} \tag{2.5}$$

(T is the temperature (in K) and k the specific rate coefficient of the reaction.)

The lifetime of OCS in the stratosphere is of the order of 10 years with respect to reactions 2.1 to 2.3. The majority (91 %) of the OCS transported into the stratosphere returns to the troposphere [Berresheim et al., 1995, Seinfeld and Pandis, 1998, Brasseur et al., 1999].

(6) SO_2 in the stratosphere is oxidized by OH radicals to form SO_3 and H_2SO_4 (reactions 2.13 to 2.15). At altitudes above 20 km photolysis of SO_2 is also possible [Brasseur et al., 1999].

(7) Stratospheric trace gases like OCS and SO_2 as well as sulfate aerosol are transported downwards into the troposphere. The lifetime in the stratosphere due to downward transport is of the order of two years [Brasseur et al., 1999].

(8) SO_2 and other S(+IV) compounds undergo gas phase oxidation by OH in the troposphere to yield S(+VI) e.g. in H_2SO_4. The oxidation of SO_2 is a central aspect of the sulfur cycle and is further discussed in section 2.2.1.

(9) S(+IV) species (mainly SO_2) can be absorbed in the liquid phase of hydrosols[2]. The relative amount of SO_2 that is dissolved in the aqueous phase of clouds is about 7.2 % at 293 K, decreasing to 1.4 % at 268 K [Brasseur et al., 1999].

(10) SO_2 shows high reactivity in hydrosol particles and droplets. Liquid phase oxidation of S(+IV) occurs by reaction with H_2O_2(aq) and O_3(aq). A different pathway of oxidation by O_2 in the presence of sufficient levels of catalytic metal ions is also known. Details about the liquid phase reactions of SO_2 can be found in section 2.2.1.

---

[2] hydrosols are cloud, fog or rain droplets and moist aerosol particles

(11) Nucleating gases containing S(+VI) form new particles. Condensable gases that are not capable of nucleating condense on pre-existent surfaces. Dry aerosol (mainly sulfate) forms hydrosol particles in the presence of condensable gases (see section 2.2.2).

(12) Evaporation of water leaves dry sulfate aerosol behind. This is the reversed process to path (11).

(13) Deposition of S(+IV) and S(+VI) species occurs through precipitation or sedimentation (wet or dry deposition). Sulfate and oxidized sulfur species reach the surface, where e.g. biological processes may lead to their reduction again, followed by further participation in the sulfur cycle. OCS for example has a relatively long lifetime of four years in the troposphere. The reaction with OH is its only important chemical sink here, removing about 22 % of OCS. Another 71 % are assimilated by vegetation.

Compound	FFC^a + Industry	BB^b	Oceans	Wetlands	Plants + Soils	Volcanoes
DMS		—	15-25	0.003–0.68	0.05–0.16	—
H_2S	(Total reduced	< 0.01?	< 0.3	0.006–1.1	0.17–0.53	0.5–1.5
CS_2	Sulfur: 2.2)	< 0.01?	0.08	0.0003–0.06	0.02–0.05	—
OCS		0.08	0.17	0.00006–0.12	0.01–0.03	0.01
SO_2	70	2.8	—	—	...	7–8
SO_4^{2-}	2.2	0.1	40–320	—	2–4	2–4
Total	71–77 (mid-1980s)	2.2–3.0	15-25^a	0.01–2	0.25–0.78^b	9.3–11.8

Table 2.1: Global estimates of sulfur emissions in Tg sulfur per year. The total anthropogenic emissions range from 73–80 Tg S year^{-1}, the total natural emissions^{cd} yield 25–40 Tg S year^{-1}. Table from [Seinfeld and Pandis, 1998].
^{a}Fossil Fuel Combustion
^{b}Biomass Burning
^{c}Excluding sea salt spray contributions
^{d}Excluding soil dust contributions

An overview of average measured mole fractions of sulfur species at different locations is given in table 2.2. The overview is adopted from [Seinfeld and Pandis, 1998], but further references concerning the data sets can be found in a more detailed table in [Berresheim et al., 1995]. The data reflects the most important sources of each compound as seen in table 2.1: DMS from the ocean, H_2S from vegetation, CS_2 from the ocean, vegetation and anthropogenic sources and SO_2 mostly from anthropogenic and industrial activity. The even distribution of OCS is due to its long lifetime.

Compound	Location	Average Mole Fraction (pptv)
DMS	Marine surface layer	80–110
	Continental surface layer	8–60
	Free troposphere (2–5 km)	1.5-15
H_2S	Marine surface layer	3.6–7.5
	Coastal regions	65
	Forests	35-60
	Wetlands	450-840
	Urban areas	365
	Free troposphere (2–5 km)	6-8.5
CS_2	Marine surface layer	2–18
	Continental surface layer	35–120
	Free troposphere (2–5 km)	5-7
OCS	Marine surface layer	500
	Continental surface layer	545
	Free troposphere (2–5 km)	500
SO_2	Marine surface layer	20
	Free troposphere (>5 km)	
	– Europe/North Sea/Arctic	50
	North America clean continental	160
	Coastal Europe	260
	Polluted continental air	1500

Table 2.2: Observed mole fractions of the most important atmospheric sulfur components. Table from [Seinfeld and Pandis, 1998].

Figure 2.2 shows the most important sulfur reservoirs in the global biogeochemical cycle. It illustrates that the amounts of sulfur stored in soils or the ocean e.g. exceed the sulfur content of the atmosphere by several orders of magnitude. The exchange mechanisms between the different reservoirs of sulfur that **figure 2.1** summarizes as "surface" are highly complex, and the atmospheric sulfur cycle has to be considered as only one aspect of the global biogeochemical cycle. The atmosphere is a highly mobile part of this overall cycle, distributing sulfate and gaseous sulfur species over large areas and thereby ensuring the supply of essential

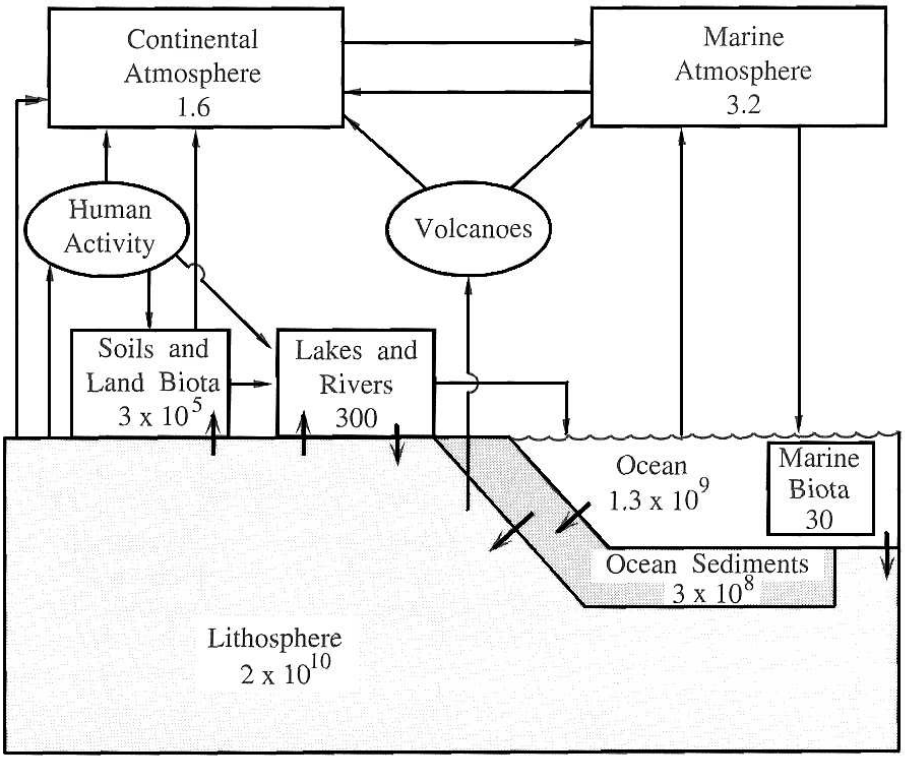

Figure 2.2: The major reservoirs of sulfur in the global biogeochemical sulfur cycle, in Tg sulfur. Figure taken from [Seinfeld and Pandis, 1998].

nutrients to the biosphere, where plants and micro-organisms reduce sulfur components as part of their digestion and growth [Berresheim et al., 1995].

2.1.1 Natural Sources of Sulfur Dioxide

Natural emissions of sulfur components contribute about 30 % of the total sulfur emissions into the atmosphere (according to table 2.1 sulfate injection by sea salt spray and soil dust are ignored in this estimate) [Berresheim et al., 1995]. The most important natural source of SO_2 is volcanism. Sulfur emissions from natural sources such as bacteria, biomass burning, livestock or vegetation may originate in human activity such as land use, farming or deforestation as well as natural phenomena. Still, they will be described as natural emissions in the following sections. The overlap between natural and anthropogenic sources of sulfur should be kept in mind nevertheless.

Volcanism

Volcanic activity is quantitatively the most important entirely natural source of SO_2. Other sulfur containing gases and SO_2 precursors from volcanoes are H_2S, OCS and CS_2. The total amount of emitted volcanic sulfur is suggested to be of the order of 10 % of the total anthropogenic sulfur flux to the atmosphere [Berresheim et al., 1995].

Volcanoes also emit large quantities of water vapor, CO_2, sulfate ashes and halogen compounds such as BrO, HCl or HF. They are mostly located alongside the edges of tectonic plates in remote areas, their global distribution following the borders of these plates and thus being of a highly inhomogeneous kind. Not only are the locations of volcanoes distributed inhomogeneously, their eruptions also occur irregularly and emit large amounts of gases and material in a short time span, depending on the intensity of the specific eruption, instead of constantly emitting over long periods of time. Even the composition of the emitted gas mixture can vary with the type of volcano and eruption. Estimates about the average emission of volcanid SO_2 range from 1.5–50 Tg sulfur per year [Bluth et al., 1993]. Table 2.1 implies a tighter range of about 9.3–11.8 Tg sulfur per year, which emphasizes the uncertainties that are associated with these estimates.

A specialty of volcanic trace gas and aerosol emission is the chance of injecting these climate active compounds into the stratosphere (not obligatory for all eruptions). The composition of the injected gas is very variable, but it typically consists of 70 % H_2O, 20 % CO_2 and 6 % SO_2 [Brasseur et al., 1999]. Volcanoes can thus directly influence the stratospheric aerosol layer (see section 2.2.3). The second most emitted sulfur gas is H_2S. It carries $\sim 1/4$ of the overall emitted sulfur, while the majority of $\sim 3/4$ is emitted in the form of SO_2. Volcanic sulfur emissions are of the order of at least 10 % of the anthropogenic contributions, but their sulfur emission can sporadically exceed even the anthropogenic contribution in the area surrounding the erupting volcano – for example at Mount Etna on the island of Sicily [Berresheim et al., 1995, Graf et al., 1997].

Biosphere and Ocean

Oceanic algae and zooplankton are a major source of DMS (see table 2.1). The rate of their emission is influenced by annual and diurnal cycles. The oxidation processes of DMS with OH (during daytime), NO_3 (at night) or halogen radicals are very fast. The oxidation mechanism is rather complex and its pathways strongly depend on pH levels, temperature, and availability of reaction partners. It is further discussed in [Berresheim et al., 1995]. Major products of DMS oxidation are SO_2 and MSA, among others.

The Ocean provides an average of 15–25 Tg sulfur to the atmosphere each year (see table 2.1), while DMS estimates range from 12–51 Tg sulfur per year [Berresheim et al., 1995]. Other sulfur components emitted by the oceanic eco-system apart from DMS are CS_2 and OCS as well as sulfate. CS_2 is the most important precursor gas for OCS, which again yields stratospheric SO_2 (reactions 2.1 to 2.5). The oxidation of CS_2 with OH is complex and involves the reversible addition of the hydroxyl radical. The product of the addition (CS_2OH) reacts with O_2 and yields both sulfur species SO_2 and OCS [Brasseur et al., 1999]:

$$
\begin{aligned}
\mathrm{CS_2} + \cdot\mathrm{OH} &\rightleftharpoons \mathrm{CS_2OH} && (2.6)\\
\mathrm{CS_2OH} + 2\mathrm{O_2} &\longrightarrow \mathrm{HO_2} + \mathrm{SO_2} + \mathrm{OCS} \quad , 80-85\,\% && (2.7)\\
&\longrightarrow \mathrm{HCO} + 2\,\mathrm{SO_2} \quad , 15-20\,\% && (2.8)
\end{aligned}
$$

The oxidation of CS_2 generates about 30 % of the total OCS in the atmosphere.

On continents and especially in swamp regions anaerobic micro-organisms use sulfate ions (SO_4^{2-}) to produce H_2S, which partly enters the atmosphere. Most of the H_2S does not leave the soil instantly though, since it reacts to form iron(II)sulfide (FeS) or dissolves in water and thus enters the hydrological cycle. The dissolved H_2S may be released from the liquid phase to the atmosphere later. The oxidation with OH yields a H_2S lifetime of about 2.4 days and produces SO_2 via four elementary steps [Berresheim et al., 1995]:

$$\mathrm{H_2S} + \cdot\mathrm{OH} \longrightarrow \cdot\mathrm{SH} + \mathrm{H_2O} \quad , \; k = 4.8 \cdot 10^{-12}\ \mathrm{cm^3\ s^{-1}} \tag{2.9}$$

$$\cdot\mathrm{SH} + \mathrm{NO_2} \longrightarrow \mathrm{HSO}\cdot + \mathrm{NO} \quad , \; k = 5.8 \cdot 10^{-11}\ \mathrm{cm^3\ s^{-1}} \tag{2.10}$$

$$\mathrm{HSO}\cdot + \mathrm{NO_2} \longrightarrow \mathrm{HSO_2} + \mathrm{NO}\cdot \quad , \; k = 9.6 \cdot 10^{-12}\ \mathrm{cm^3\ s^{-1}} \tag{2.11}$$

$$\mathrm{HSO_2} + \mathrm{O_2} \longrightarrow \mathrm{SO_2} + \mathrm{HO_2} \quad , \; k = 3.0 \cdot 10^{-13}\ \mathrm{cm^3\ s^{-1}} \tag{2.12}$$

Another possibility is the rapid reaction with ozone instead of NO_2 in reactions 2.10 and 2.11 [Brasseur et al., 1999].

This four-step-mechanism leads to the formation of SO_2 from H_2S, but the intermediate products may also react differently with other oxidants such as halogen atoms, oxygen or ozone as the reaction proceeds. These reactions are listed in [Berresheim et al., 1995].

When hydroxyl radical chemistry stops at night (see section 2.2.1) the oxidation of H_2S can occur via NO_3 instead of OH in reaction 2.9. Nitric acid (HNO_3) is then formed instead of H_2O. The rate constant of this competing oxidation path is as low as $k < 8{\cdot}10^{-16}$ cm^3 s^{-1} and does not have any influence during daytime [Berresheim et al., 1995].

The estimated 2 Tg sulfur per year emitted from wetlands include about 57 % H_2S and 34% DMS. According to [Berresheim et al., 1995] further sulfur components contribute about 6 % (OCS) or 3 % (CS_2).

Plants in general need sulfur to build amino acids and proteins, therefore taking up and reducing sulfate from the soil. Some products of this biological activity enter the atmospheric sulfur cycle, for example H_2S, DMS, CS_2 and OCS with relativ amounts of 68 %, 21 %, 7 % and 4 %, respectively [Berresheim et al., 1995].

The land biosphere (including vegetation and soils) emits about 0.4–1.2 Tg sulfur per year into the atmosphere, mainly in tropical and subtropical regions, where large quantities of biomass are located. An even larger vegetation-related source with 2–4 Tg sulfur per year is the burning of vegetation [Brasseur et al., 1999].

Biomass Burning

Berresheim et al. [1995] state that around 95 % of biomass burning is human–initiated and could also be understood as an anthropogenic emission source though it is closely related to the biosphere topic. Nevertheless, it is deliberately mentioned at this point, if only to emphasize the common misconception that fires mostly occur naturally. Biomass burning mainly releases the sulfur compounds SO_2 and OCS into the atmosphere, while the amounts of CS_2 and H_2S probably only range in the region of a few percent of the OCS emissions. An estimate of about 0.1 Tg sulfur per year is injected into the atmosphere from biomass burning. Such estimates are highly inaccurate though, since even the total burning area is only known with an uncertainty of about ± 50 % [Berresheim et al., 1995]. Further remarks on biomass burning, especially during the AMMA campaign, will be made in section 5.2.

2.1.2 Anthropogenic Emissions of Sulfur Dioxide

The amount of man-made emissions of sulfur has changed dramatically since the combustion of fossil fuels started. Petroleum, natural gas and coal naturally contain sulfur, the specific amounts depend on the formation processes. Anthropogenic sulfur emissions, which predominantly consist of SO_2 (94 %, as estimated in [Berresheim et al., 1995], see table 2.1), also include contributions from creating usable agricultural areas via deforestation, or emissions from agriculture and farming. In general all changes of vegetation and land usage have an influence on the emission of climate active trace gases from that area.

The overall amount of global anthropogenic emissions adds up to 73–80 Tg sulfur per year and exceeds the natural contribution at least twice (see table 2.1). Anthropogenically emitted sulfur compounds apart from SO_2 include H_2SO_4, sulfate and CS_2, and from biomass burning OCS and H_2S [Seinfeld and Pandis, 1998, Brasseur et al., 1999].

Fossil fuel combustion is the overall biggest source of sulfur in the atmosphere, representing roughly 90 % of anthropogenic sulfur emissions. This combustion mostly happens in the planetary boundary layer or in the lower troposphere [Berresheim et al., 1995].

The amount of emitted sulfur varies with the kind of fuel that is used: Heavy fuel oil contains up to 5 % sulfur, air traffic kerosene only contains a mass mixing ratio of 350 ppmM[3] sulfur and desulfurized Diesel fuel is restricted by EU directives to less than 50 ppmM sulfur content.

Airtraffic is one of the few anthropogenic sulfur sources that can inject its emissions directly into the upper troposphere and lower stratosphere (others are e.g. industrial sites at very high altitudes). This kind of emission has a strong influence on the aerosol concentration in the middle and upper troposphere. The sulfur content of the used kerosene is low, but pre-existent aerosol in the upper troposphere and lower stratosphere is rare, so new particle formation by H_2SO_4 is favored. The effects of enhanced sulfur content and aerosol formation in this region of the atmosphere will be discussed in sections 2.2 and 2.2.3.

Ship emissions pollute the clean marine boundary layer. The only other direct source of aerosol particles in these regions is sea salt spray that yields sulfate aerosol. Combustion of heavy oil with a high natural sulfur content favors the formation of cloud condensation nuclei (CCN) and clouds, especially along frequently used ship traffic routes. See section B.1 for an example of airborne measurements of SO_2 over the English Channel.

2.2 Sulfur Dioxide and Aerosol Particles

Aerosol particles are generally found in the size range of some nm to tens of μm. They contain sulfates, nitrates, ammonium, organic material, minerals, sea salt, hydrogen ions and water [Seinfeld and Pandis, 1998]. The highest number concentration of aerosol particles is found at ground level in cities. The concentrations reach values of $10^5\,\mathrm{cm}^{-3}$ and decrease rapidly with increasing altitude [Roedel, 1994]. Aerosol particles are either emitted directly as soot, mineral dust or in the marine boundary layer as sea salt particles, or they are formed via condensation processes. These direct and indirect sources of aerosol will be discussed in the following sections.

SO_2 is oxidized to H_2SO_4, which condenses on the surface of pre-existent aerosol particles and leads to their growth, or it contributes to the formation of new particles. Typical concentrations of H_2SO_4 range from 10^5–$10^7\,\mathrm{cm}^{-3}$, which corresponds to mole fractions

---

[3] ppmM = parts per million (mass) = 10^{-6}= 1 μg/g
pptM, ppbM and ppqM similar to pptv, ppbv and ppqv

of 4–400 ppqv at 1013 hPa and 293 K. These mole fractions are rather small due to the low saturation vapor pressure of sulfuric acid, which leads to rapid condensation of H_2SO_4. This saturation vapor pressure ranges from about 10^{-5} torr ($1.3 \cdot 10^{-5}$ hPa) at 300 K to 10^{-7} torr ($1.3 \cdot 10^{-7}$ hPa) at 270 K, decreasing further with decreasing temperature. All numbers from [Seinfeld and Pandis, 1998].

Recently particulate matter (Feinstaub) from city traffic emissions has been a major issue of discussion. Measurements of sulfuric acid in the exhaust of Diesel engines by our group contribute to a better understanding of the amount of micro-particle formation, especially through the oxidation of SO_2 in modern catalytic converters.

2.2.1 SO_2 Oxidation Chemistry

One of the central aspects of the atmospheric sulfur cycle is the oxidation of sulfur from species with low oxidation numbers (e.g. S(-II) in H_2S) to those with oxidation state S(+VI), mainly sulfate and H_2SO_4. The deposition of sulfur and thus the removal from the atmosphere generally (but not exclusively) happens in the form of S(+IV).

Gas Phase Reactions

The gas phase oxidation of SO_2 with oxygen molecules O_2 is generally possible, but very slow without catalysation [Seinfeld and Pandis, 1998]. It can be neglected compared to the dominant oxidation through OH radicals in the presence of water vapor. This radical reaction follows the so-called Stockwell Calvert mechanism:

$$\begin{aligned} SO_2 + \ \cdot OH + M &\longrightarrow HOSO_2 \cdot + M \quad , \ k = 9 \cdot 10^{-13}\ \mathrm{cm}^3\ \mathrm{s}^{-1} && (2.13) \\ HSO_3 \cdot + O_2 &\longrightarrow SO_3 + \ HO_2 \cdot \quad , \ k = 4.3 \cdot 10^{-13}\ \mathrm{cm}^3\ \mathrm{s}^{-1} && (2.14) \\ SO_3 + \ H_2O + \ M &\longrightarrow H_2SO_4 + \ M \quad , \ k \approx 1.2 \cdot 10^{-15}\ \mathrm{cm}^3\ \mathrm{s}^{-1} && (2.15) \end{aligned}$$

The first step (2.13) is pressure and temperature dependent and is the limiting step for the formation of H_2SO_4 after Stockwell and Calvert. The indicated values for the rate coefficients k are valid for a pressure of 1000 hPa and a temperature of 295 K [Brasseur et al., 1999, Seinfeld and Pandis, 1998]. The mechanism of reactions 2.13–2.15 has been proposed by Stockwell and Calvert, while our group confirmed the reaction path in laboratory experiments.

The lifetime of SO_2 with respect to reaction 2.13 is about a week, with typical atmospheric OH radical concentrations of about 5–10 $\cdot 10^6\,\mathrm{cm}^{-3}$ [Seinfeld and Pandis, 1998].

High humidity and strong radiation at small wavelengths favor the formation of OH from water by excited oxygen atoms $O(^1D)$, which are the product of the photolysis of ozone at $\lambda \leq 320\,\mathrm{nm}$ after reaction 2.16 [Seinfeld and Pandis, 1998]. (The ground state atom $O(^3P)$ is produced by ozone photolysis at $\lambda \leq 1180\,\mathrm{nm}$.)

$$\begin{aligned}
\mathrm{O_3} + \mathrm{h}\nu &\longrightarrow \mathrm{O(^1D)} + \mathrm{O_2} && , \lambda \leq 320\,\mathrm{nm} && (2.16)\\
\mathrm{O(^1D)} + \mathrm{H_2O} &\longrightarrow 2\ \cdot\mathrm{OH} && , k = 2.2 \cdot 10^{-10}\,\mathrm{cm^3\ s^{-1}} && (2.17)\\
\mathrm{O(^1D)} + \mathrm{M} &\longrightarrow \mathrm{O(^3P)} + \mathrm{M} && && (2.18)
\end{aligned}$$

Highest production rates for excited $O(^1D)$ are thus expected in the tropics. For example: at 298 K and a relative humidity of 50 %, about 1/5 of the available $O(^1D)$ atoms yield OH radicals, when they react with water molecules after (2.17). Most of the excited $O(^1D)$ atoms lose their energy by collision with O_2 or N_2 and yield $O(^3P)$. M represents these collision partners in reaction 2.18 [Seinfeld and Pandis, 1998].

Another photolytical source of OH is the dissociation of nitrous acid (HONO) at wavelengths of $\lambda < 400\,\mathrm{nm}$ [Seinfeld and Pandis, 1998], or OH may be recycled from HO_2, the product of reaction 2.14, by the reaction with NO (reaction 2.19).

$$\mathrm{NO} + \mathrm{HO_2}\cdot \longrightarrow \mathrm{NO_2} + \cdot\mathrm{OH} \qquad (2.19)$$

A comparison of these mechanisms can be found in [Seinfeld and Pandis, 1998] (OH from O_3, HONO and HO_2).

Radical chemistry involving the hydroxyl radical stops at night, since the production of OH involves photochemistry of O_3 or NO_2 (yielding NO at $\lambda < 424\,\mathrm{nm}$). The average lifetime of a HO_x radical ($OH + HO_2$) is 45 seconds, with recycling of HO_2 occuring every 9 seconds, and an average of 5 cycles before the removal of HO_x [Seinfeld and Pandis, 1998].

For SO_3 the reaction with water in the gas phase (as in reaction 2.15) is by far dominant due to the excessive amounts of liquid or gaseous water available in the atmosphere while SO_3 is known to stick to aqueous surfaces. The gas phase reaction of SO_3 with water to form H_2SO_4 is thought to involve two water molecules, but the reaction is not yet fully understood [Brasseur et al., 1999].

[Reiner and Arnold, 1994] measured this reaction in laboratory experiments. Increased concentrations of H_2O resulted in an exponential decrease in SO_3 and increase in H_2SO_4, such that an averaged rate constant of the reaction in the gas phase could be deduced with an error of 17 % (see reaction 2.15).

Liquid Phase Reactions / Cloud Processes

Sulfur dioxide is moderately soluable in water (see comment (9) of the sulfur cycle in section 3.18). But the solubility is positively influenced by the formation of the bisulfite ion HSO_3^-. Raoult´s law states that the lower the mole fraction of a component in a solution is, the more the vapor pressor of the gas over the solution drops [Seinfeld and Pandis, 1998]. Thus, when SO_2 is converted to bisulfite, its mole fraction in the solution decreases and allows for more SO_2 to enter the liquid phase. The overall solubility of S(+IV) (including SO_2, HSO_3^- and the sulfite ion SO_3^{2-}) is strongly dependent on the solutions pH and increases with increasing pH, when the equilibrium is shifted to the right of equation 2.21. HSO_3^- is the dominant compound for pH between 2 and 7, as it is the case in atmospheric droplets. At even more alkaline $pH > 7$ as in sea salt particles the concentration of SO_3^{2-} exceeds that of HSO_3^- [Seinfeld and Pandis, 1998].

The formation of the bisulfite ion and the sulfite ion from SO_2 proceeds as follows [Seinfeld and Pandis, 1998]:

$$SO_2(g) + H_2O \rightleftharpoons SO_2 \cdot H_2O \tag{2.20}$$

$$SO_2 \cdot H_2O \rightleftharpoons HSO_3^- + H^+ \tag{2.21}$$

$$HSO_3^- \rightleftharpoons SO_3^{2-} + H^+ \tag{2.22}$$

For pH values less than 5 the oxidation of HSO_3^- by H_2O_2 is favored, since the rate constant for this reaction is found to increase exponentially with decreasing pH values. H_2O_2 is also highly soluable with a ratio of $1:6.4$ for molecules in the gaseous vs liquid phase at 293 K, decreasing to $1:0.8$ at 268 K. The intermediate product of reaction 2.23 is believed to be the peroxymonosulfurous acid ion SO_2OOH^- [Brasseur et al., 1999].

$$HSO_3^- + H_2O_2 \longrightarrow SO_2OOH^- + H_2O \tag{2.23}$$

$$SO_2OOH^- + H^+ \longrightarrow H_2SO_4 \tag{2.24}$$

H_2O_2 is highly soluable in water, but the solubility of the next important oxidant ozone is very low in comparison. The relative amount of O_3 dissolved in the aqueous phase of clouds compared to O_3 in the gas phase is about $9.1 \cdot 10^{-8} : 1$ at 293 K, increasing to $1.9 \cdot 10^{-7} : 1$ at 268 K. Oxidation of S(+IV) compounds by ozone is rapid though, particularly in alkaline solution, where the rate constants for reactions 2.25 and 2.26 increase strongly with increasing pH values. Sea salt aerosol for example has a typical pH of 8, which favors the oxidation by ozone in the marine boundary layer [Brasseur et al., 1999].

$$HSO_3^- + O_3 \longrightarrow HSO_4^- + O_2 \tag{2.25}$$

$$SO_3^{2-} + O_3 \longrightarrow SO_4^{2-} + O_2 \tag{2.26}$$

The SO_2 originating from oceanic DMS may thus be rapidly taken up and oxidized in sea salt aerosol of the lower marine boundary layer (since high pH values also favor the formation of the bisulfit ion). This aspect is a reason for controversial discussions about the influence of

DMS on SO_2 generation and further enhanced formation of CCN by H_2SO_4, not to mention the uncertainties concerning the complex oxidation mechanisms of DMS itself.

In polluted air there is another important pathway for the oxidation of SO_2. The metals Fe(+III) and Mn(+II) are strong catalysts and support oxidation of SO_2 by oxygen molecules in the liquid phase. Soot has also been found to catalyse the auto-oxidation of SO_2. The liquid phase oxidation mechanisms are further explained in [Berresheim et al., 1995, Seinfeld and Pandis, 1998].

After oxidation in droplets SO_2 can be removed from the atmospheric part of the sulfur cycle by wet deposition through precipitation.

2.2.2 Sulfuric Acid as a Source of Aerosol Particles

Oxidation of SO_2 that yields H_2SO_4 is a major indirect source of CCN and fine sulfate aerosol. These small particles have lifetimes of a few days up to a week in the troposphere and are not subject to fast sedimentation, due to their small diameters of sub–micrometers [Berresheim et al., 1995, Ramanathan et al., 2001]. Berresheim et al. [1995] also estimate that globally only a small fraction of 6 % of anthropogenically emitted SO_2 leads to CCN via H_2SO_4 nucleation (as opposed to the condensation of H_2SO_4 on pre-existent particles or other SO_2 sinks like dry deposition). Still, H_2SO_4 is considered to play an important role in aerosol formation, and with it its most important precursor gas SO_2, especially in remote clean areas or in the upper and colder troposphere, where little pre-existent aerosol is found and nucleation of H_2SO_4 occurs. The following sections are concerned with the nucleation and condensation of H_2SO_4, and with the formation and growth of aerosol. Climate effects of aerosol will also be discussed in more detail.

Condensation, Nucleation and Growth

Particles are either directly injected into the atmosphere as primary aerosol or being formed by nucleation from the gas phase. Normally more than one chemical species take part in atmospheric nucleation processes (as opposed to homomolecular homogeneous nucleation, involving only one chemical species): a high supersaturation, which is usually not given under atmospheric conditions, is needed for self nucleation of a single compound like gaseous

H_2SO_4. Nucleation occurs by formation of molecular clusters from the gas phase that may contain less than 20 molecules. The most important homogeneous nucleation processes in the atmosphere are heteromolecular and involve H_2SO_4 and water vapor (binary nucleation e.g. in industrial plumes) or H_2SO_4, NH_3 and water vapor (ternary nucleation e.g. in the continental boundary layer) [Kulmala, 2003].

The condensation of polarizable molecules is strongly favored by the presence of ions that act as a trigger for this ion-induced nucleation. Mole fractions of ions in the upper troposphere and stratosphere are high enough to make this process dominating in these atmospheric regions. Low temperatures decrease the saturation vapor pressure of H_2SO_4 even further, and few pre-existent aerosol particles take up H_2SO_4 by condensation. Thus the rate of new particle formation in these altitudes is especially sensitive to additional SO_2 injections, e.g. from air traffic, which effectively yield H_2SO_4 through cosmic ray photochemistry (hydroxyl radical formation from ozone). Investigations about the influence of cosmic rays on ion induced nucleation have recently been conducted at the CERN laboratories in Geneva, and were supported by our group through highly accurate measurements of H_2SO_4 inside a nucleation chamber.

Other laboratory experiments had been performed by our group before to deduce the influence of ions (H^+ and HSO_4^- in this case) on molecule cluster formation which leads to aerosol formation. The ion induced binary nucleation involving H_2SO_4 and water was investigated, and a high enrichment of H_2SO_4 in small negative cluster ions was found, while positive clusters were enriched in H_2O. Large ion clusters of different charge recombine to form neutral H_2SO_4–H_2O aerosol particles. These neutral clusters are able to further grow via condensation of gaseous H_2SO_4 [Wilhelm et al., 2004, Sorokin et al., 2006].

The growth of stable molecular clusters by condensation competes with their coagulation, where the number concentration of aerosol particles decreases when clusters collide and stick together. The faster the condensation onto the newly nucleated particles, the larger the number of surviving new particles. The low saturation vapor pressure of H_2SO_4 contributes to this fast condensation.

Due to the Kelvin effect larger droplets will grow at the expense of smaller ones, because the saturation vapor pressure over the curved surface of the droplet increases with its diameter and favors condensation onto the larger droplets [Seinfeld and Pandis, 1998, Brasseur et al., 1999].

A scheme of particle nucleation and growth is shown in **figure 2.3**. Organic compounds, indicated in the figure as larger black spheres, also play an important role in the formation of CCN as they condense on the initially inorganic clusters and undergo chemical reactions on their surfaces [Kulmala, 2003]. These organic compounds contribute to the content of carcinogenic substances in aerosol particles, which makes them a health hazard at inhalation.

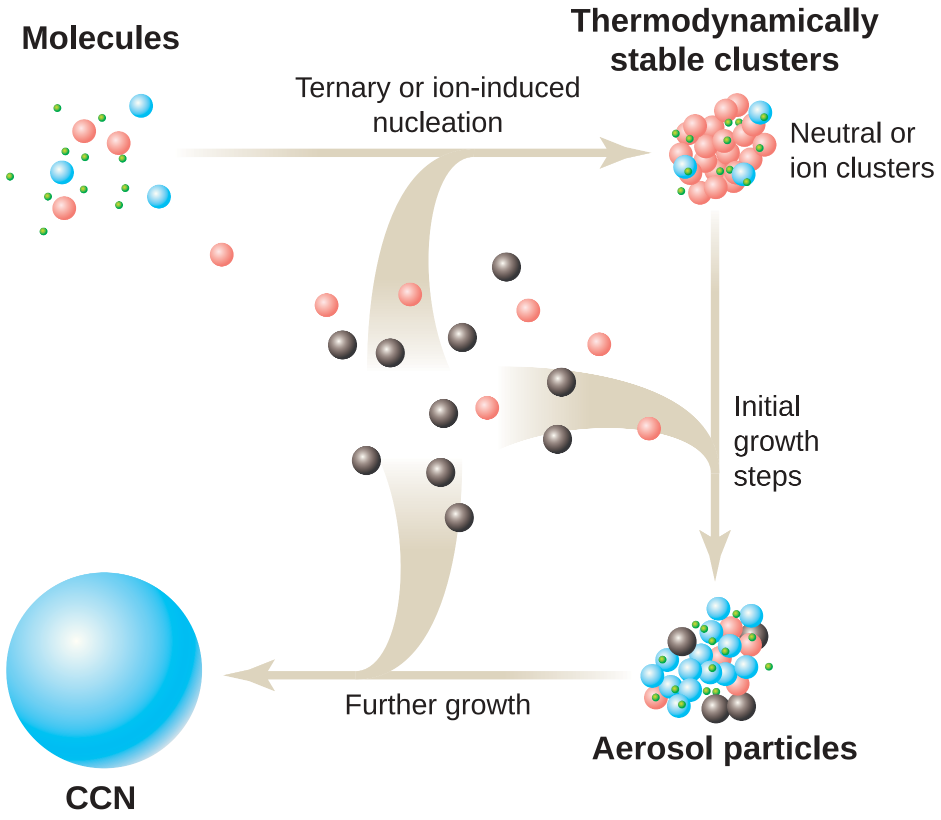

Figure 2.3: Scheme for the nucleation and growth of particles [Kulmala, 2003].

The condensation on the surface of pre-existent droplets and aerosol particles (heterogeneous condensation) is the main removal mechanism for gas phase H_2SO_4 and known as acid rain. H_2SO_4 is protonated in the droplet and yields bisulfate and sulfate ions in the liquid phase or — after evaporation of the droplet water — in the remaining dry aerosol particle.

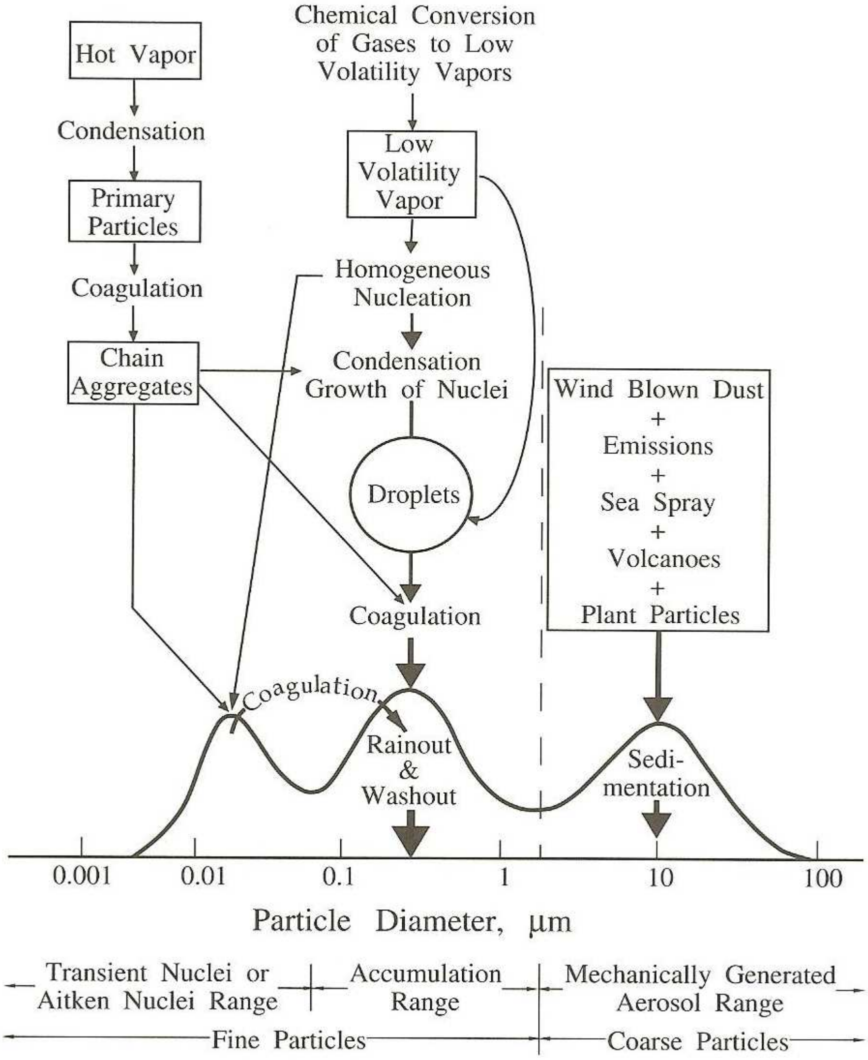

Figure 2.4: Schematic distribution of particle surface area vs diameter. Principal modes, sources, and particle formation and removal mechanisms are indicated [Seinfeld and Pandis, 1998].

The main deposition processes of aerosol particles are washout through precipitation (wet deposition) and sedimentation, especially of larger particles (dry deposition without precipitation). Aerosol particles generally populate three modes. The number concentration of each mode depends on the evolution of the aerosol population. Smaller particles and droplets can be hindered from growing to full size and stick to one another or to larger particles (coagulation) before they experience depositon. Growth and coagulation processes change the particle size distribution of the specific particle population to larger diameters and reduce the total number of particles as time proceeds. This mechanism produces an increased number of so-called accumulation mode particles of larger diameters that will mainly experience wet deposition.

Figure 2.4 gives an overview of the major formation and removal processes of aerosol particles in the atmosphere. The coarse mode particles have diameters of about 10 μm, mainly consisting of primarily injected aerosol: sea salt particles and mineral dust. Fine particles in the nucleation mode have diameters just above 10 nm. These fine particles include the majority of particles, refering to their number, while the total mass of a particle population is dominated by the amount of larger particles. The accumulation mode consists of particles that have grown from newly created particles through condensation or coagulation to diameters of $< 1\,\mu$m.

Other Sources for Aerosol Particles

Most of the sulfate that is directly injected into the atmosphere consists of relatively large sized particles in the diameter range of micrometers (see **figure 2.4** for the size ranges of aerosol particles). These larger particles are usually deposited at the surface via sedimentation after they have travelled distances of typically a few hundred kilometers. The smaller submicron aerosol particles can have atmospheric lifetimes of a few days in the troposphere and a few years, if they reach the stratosphere [Berresheim et al., 1995].

Aerosol particles that are directly emitted initially consist of sea salt, mineral dust, sulfate, black carbon (soot) and organic carbon particles. The individual particles consist of a composite misture of the listed core materials and a coating of sulfates, nitrates and organics [Ramanathan et al., 2001]. Sea salt particles originate from bursting salt water bubbles of ocean spray. They are found exclusively over the ocean where concentrations typically range from 5–10 cm^{-3}. Concentrations strongly decrease with altitude until there is almost no sea salt aerosol present above 2–3 km. Continental primary aerosol is dominated by mineral dust. Volcanism, pollen and fires generally play a minor role, but their contribution strongly depends on local emission aspects and the proximity of major emission sources. Anthropogenic sources of directly emitted aerosol are industry, heating and traffic, mostly via fossil fuel combustion [Seinfeld and Pandis, 1998].

2.2.3 Aerosol and Climate

The amount of aerosol particles has a strong impact on climate change since they counteract the anthropogenic greenhouse effect, even though their lifetime in the atmosphere is less than a week [Ramanathan et al., 2001]. The influence of greenhouse gases has been studied and modeled before the concentrations and effects of aerosol particles were well known. So older climate models predict a global warming scenario without considering aerosol effects. The result is that these models may have underestimated the warming by greenhouse gases, which was masked by cooling aerosol effects. The greenhouse warming is thus stronger than previously thought, but cooling effects decrease the overall warming effect.

Due to pollution the concentration of particles today is supposed to be about 40 % higher than it would be in an uninfluenced atmosphere [Penner, 2004]. But modern industrial power plants have been equipped with filters to reduce the emission of sulfur species, decreasing the H_2SO_4 availability for aerosol nucleation in the atmosphere. The investigation of aerosol effects will lead to a better understanding of how our climate might evolve. The increase or decrease of aerosol emissions and trace gas concentrations will strongly influence the future of our climate.

The different climate effects of aerosol are usually divided into the following categories:

- Direct aerosol effect: Aerosol particles show a direct cooling effect by reflecting and absorbing solar radiation [Penner, 2004, Ramanathan et al., 2001].

- First indirect effect: Aerosol particles from pollution events can act as additional CCN and increase the number of droplets that form in a cloud. The size distribution simultaneously shifts to smaller diameters. Clouds with more and smaller droplets show increased reflectivity of solar radiation, since their droplet surface area is larger, and they contribute to enhanced cooling. This first indirect aerosol effect is thought to be comparible in magnitude to the greenhouse effect of anthropogenic CO_2. The increased solar heating in the atmosphere by radiation absorption changes the atmospheric temperature structure and can affect global circulation processes [Ackerman et al., 2004, Zhao et al., 2006, Ramanathan et al., 2001].
- Second indirect effect: Another result of more and smaller droplets is the decreasing tendency for a cloud to produce precipitation. This is supposed to increase the overall cloud water content, the cloud´s lifetime and the overall amount of clouds, which leads to even higher reflectivity. It has been calculated that the overall cloud cover and the water content of an indiviual cloud should increase due to reduced precipitation [Penner, 2004, Ramanathan et al., 2001]. This also influences the lifetime of aerosol in the atmosphere, since precipitation is the most important mechanisms for the removal of small aerosol particles. But the expected higher cloud water content due to longer lifetimes of clouds could not be observed, specifically not in the aerosol-polluted marine boundary layer. In more detail, Ackerman et al. [2004] argue that clouds with decreased precipitation mix with overlying air and only then show an increased liquid water content, when this air is humid an does not cause evaporation of cloud water. The second indirect aerosol effect on cloud water content might thus be regionally restricted. An increase in cloud lifetime has also not been reliably observed [Ramanathan et al., 2001].

These aerosol effects — less solar radiation reaching the surface of the Earth and less precipitation being released — can weaken the hydrological cycle and effect not only temperatures but the availability and quality of fresh water [Ramanathan et al., 2001].

Aerosol particles are found in a variety of chemical compositions and thus possess different properties. Pure sulfate aerosol only absorbs little solar radiation but primarily scatters and causes cooling at the surface as well as in the atmosphere. This special case of pure sulfate rarely occurs, and the majority of aerosol consists of a soot, dust or sea salt particle core with a coating of organics, sulfates and nitrates [Ramanathan et al., 2001].

Soot particles from fossil fuel combustion or biomass burning (emitted in about equal amounts from both sources globally) exhibit a special property: they absorb radiation of solar or terrestrial origin rather than reflecting it and thus counteract aerosol cooling. Even more, they also absorb solar radiation that has already been scattered and would otherwise escape into space. A warming effect on the atmosphere is the result. Desert dust is also supposed to interact with terrestrial radiation and contribute to warming, while the influence of anthropogenic aerosol is minor in this energy range. Ramanathan et al. [2001] further states that there is a semidirect effect of soot aerosol on clouds: The heating of the boundary layer air due to radiation absorption by soot might cause the evaporation of cloud droplet water, which would allow more radiation to reach the surface. This would lead to heating at the surface due to soot aerosol. This absorption of radiation may not only take place in the atmospere, but also when soot is deposited on areas of high albedo like snow, decreasing the reflectivity of the surface and thus contributing to warming [Penner, 2004, Ramanathan et al., 2001].

Apart from droplet sizes and number concentration, the height and temperature distribution of a cloud cover determine its overall effect:

High clouds, located in the cold upper troposphere, consist of ice particles and absorb more infrared radiation energy than they reflect incoming solar radiation energy. An increase in high ice clouds, probably in the form of airtraffic condensation trails or via H_2SO_4 injection, would then contribute to warming. Little work has been done addressing the influence of aerosol pollution on the nucleation of ice particles in high clouds, but the role of particularly sulfate aerosol particles as nuclei for droplets and ice crystals is important. Desert dust may act as good ice cloud nuclei, too [Penner, 2004, Ramanathan et al., 2001].

Low level clouds absorb infrared radiation from the surface, but rather increase the Earth´s albedo and have an overall cooling effect. The influence of aerosol pollution on the water content and lifetime of these clouds has been mentioned under the point of the second indirect aerosol effect and is generally uncertain.

A study by Zhao et al. [2006] show that if the number concentration of droplets in a cloud is low (about 50 cm^3), then the measured relative dispersion shows a wide range of values, generally from 0.2–0.8. These values converge to a more narrow range of 0.4–0.5 when the number concentration increases (up to $> 1000\,cm^3$). The measurements that lead to these results took place in clean as well as polluted areas and show similar relationships between cloud number concentration and relative dispersion for all cases, only that cloud number concentrations reached higher values (up to about $1000\,cm^3$) in polluted areas as opposed to smaller concentrations (up to about $400\,cm^3$) in clean areas. The surprising results are explained by additional cloud dynamic effects. The result is a generally high uncertainty concerning the radiative forcing of low number concentration clouds in unpolluted areas. Clouds with high number concentrations show a more narrow range of values for their relative dispersion and thus have a more predictable effect. This knowledge might help to improve models concerning cloud effects.

An apparently stable and globally distributed layer of aerosol exists above the tropopause, the so-called Junge layer (first measured by Junge et al. in 1961). It is found at about 15–23 km, at the altitude of the stratospheric ozone density maximum. Stratospheric aerosol occurs as sulfate and droplets that generally consist of 75 % H_2SO_4 and 25 % H_2O [Berresheim et al., 1995]. The aerosol particles have a lifetime of 1–2 years, maybe even longer for smallest particles [Seinfeld and Pandis, 1998], since precipitation does not occur and downward transport is slow. Sources for stratospheric aerosol are the conversion from OCS to H_2SO_4, and the injection of SO_2 by volcanism (see reactions 2.1 to 2.5 for OCS reactions and oxidation of SO_2), followed by nucleation. High altitude aircrafts additionally inject sulfur and soot particles that favor cloud formation. High stratospheric clouds are especially important for the ozone budget, since destruction of ozone via chlorine needs to be catalysed by cloud particle surfaces [Brasseur et al., 1999]. The influence of these clouds on the radiation budget is a general increase of warming, while stratospheric aerosol with long lifetimes (especially sulfate aerosol) strongly contributes to cooling.

Chapter 3

Method and Instrument

3.1 Chemical Ionization Mass Spectrometry

Derivation of the ACIMS-Formula

The method of Chemical Ionization Mass Spectrometry (CIMS) is used to detect trace gases that typically occur in small mole fractions of 10^{-9} (ppbv) or less. An ion source artificially produces the educt ions $\mathrm{E}^{\pm}$. Highly efficient Ion Molecule Reactions (IMR) of these educt ions with the neutral (trace gas) molecules X lead to detectable product ions of known mass and charge $\mathrm{P}^{\pm}$ (as in equation 3.1). The neutral reaction product Y is not detectable by mass spectroscopy.

$$\mathrm{E}^{\pm} + \mathrm{X} \xrightarrow{k} \mathrm{P}^{\pm} + \mathrm{Y} \tag{3.1}$$

The rate coefficients for IMR are typically higher ($k \approx 10^{-9}$ cm^3 s^{-1}) than those of rapid neutral-molecule reactions ($k \approx 10^{-11}$ cm^3 s^{-1}). This is due to the permanent or ion induced dipole moments of the reactant gas molecules X. The highest possible rate coefficient is the collision rate coefficient ($k \approx 2{\cdot}10^{-9}$ cm^3 s^{-1}), which implies a reaction of the molecules or ions at each collision.

The concentration of the neutral gas molecules X in the flow reactor can be deduced from the counting rates of its product ions $\mathrm{P}^{\pm}$ if the identity of the educt and product ions as well as the rate coefficient k of the requisite IMR (reactions 3.1 and 3.6) are known. The described method is called Active CIMS (ACIMS) if the ions are produced artificially like in our case. Passive CIMS (PCIMS) detects ions that naturally occur in the atmosphere.

For the calculations using ACIMS we assume that the concentration of X in the ambient air ([X]) is not altered by the production of $P^{\pm}$ ($[X](t) = [X]_0$). The charges are preserved during the reaction ($[P^{\pm}]+[E^{\pm}] = \text{const}$).

The production of $P^{\pm}$ from $E^{\pm}$ then yields the following differential equation 3.2. The time derivatives of $E^{\pm}$ and $P^{\pm}$ are proportional to the rate coefficient of reaction 3.1 and the availability of $E^{\pm}$ and X for the reaction.

$$\frac{\mathrm{d}}{\mathrm{d}t}[E^{\pm}] = -\frac{\mathrm{d}}{\mathrm{d}t}[P^{\pm}] = -k \cdot [E^{\pm}][X] \tag{3.2}$$

Integrating equation 3.2 and using $[X](t) = [X]_0$ yields

$$\begin{aligned} [E^{\pm}] &= [E^{\pm}]_0 \cdot \exp(-k[X]t) && (3.3) \\ [P^{\pm}] &= [E^{\pm}]_0 \cdot (1 - \exp(-k[X]t)) && (3.4) \end{aligned}$$

Dividing equation (3.3) by equation (3.4) and solving for [X] directly gives us the so-called **ACIMS Formula**:

$$[X] = \frac{1}{k \cdot t} \ln\left(1 + \frac{[P^{\pm}]}{[E^{\pm}]}\right) \tag{3.5}$$

The concentration of the neutral species X is determined by the measurable concentrations of the educt and product ions. The rate coefficient k and the reaction time t that is available for the reaction partners to form $P^{\pm}$ have to be known. The counting rates of $E^{\pm}$ and $P^{\pm}$ are assumed to be similarly proportional to their concentrations. The counting rates of the respective ions can thus be inserted in equation 3.5 and 3.7 instead of the concentrations $[E^{\pm}]$ and $[P^{\pm}]$.

The ACIMS-formula has to be altered if more than one neutral species is present to react with the educt ions, and different product ions $P_i^{\pm}$ are formed (equation 3.6). The result is the **Parallel-ACIMS Formula** in equation 3.7.

$$\mathrm{E^{\pm} + X_i \xrightarrow{k_i} P_i{}^{\pm} + Y_i} \tag{3.6}$$

$$[\mathrm{X_i}] = \frac{1}{k \cdot t} \cdot \frac{[\mathrm{P_i}^{\pm}]}{\sum_{\mathrm{j}=1}^{n}[\mathrm{P_j}^{\pm}]} \cdot \ln\left(1 + \frac{\sum_{\mathrm{j}=1}^{n}[\mathrm{P_j}^{\pm}]}{[\mathrm{E}^{\pm}]}\right) \tag{3.7}$$

A derivation of the parallel-ACIMS formula can be found in [Wollny, 1998].

Application of the ACIMS-Formula

The electrical discharge ion source that leads to the production of the educt ions is flushed with a continuous flow of oxygen. It produces radicals like $O(^1D)$, and O^-, O_2^- and O_3^- ions by electron attachment. The radicals and ions are carried into the flow reactor with the oxygen flux, where they mix with the sample air or buffer gas. The excited oxygen atoms $O(^1D)$ collide with N_2 or O_2 which leads to ground state $O(^3P)$ atoms, or they react with water vapor to form OH radicals. The $O(^3P)$ atom is converted to O_3 by reaction with O_2. The oxygen ions (O^-, O_2^- and O_3^-) react with the available H_2O, CO_2, NO_2 or SO_2 molecules. The formation of CO_3^- (a radical ion) is dominating, since CO is the most abundant of these trace gases, so this species is the major educt ion $E^{\pm}$ for further IMR [Reiner and Arnold, 1994].

The elementary parts of the instrumental setup are a flow reactor, an ion source and the Ion Trap Mass Spectrometer (ITMS) that detects the produced ions. A schematic view of this setup is given in **figure 3.1**.

An example for the application of the parallel ACIMS formula is the calculation of gaseous nitric acid (HNO_3) mole fractions. HNO_3 is measured by our group according to the following IMR with CO_3^- in the flow reactor (reactions 3.8 and 3.9).

$$\mathrm{CO_3^-(H_2O)_n + \ HNO_3 \ \xrightarrow{k_a} \ CO_3^-HNO_3(H_2O)_n} \tag{3.8}$$

$$\mathrm{CO_3^-(H_2O)_n + \ HNO_3 \ \xrightarrow{k_b} \ NO_3^-(H_2O)_n + CO_2 + OH} \tag{3.9}$$

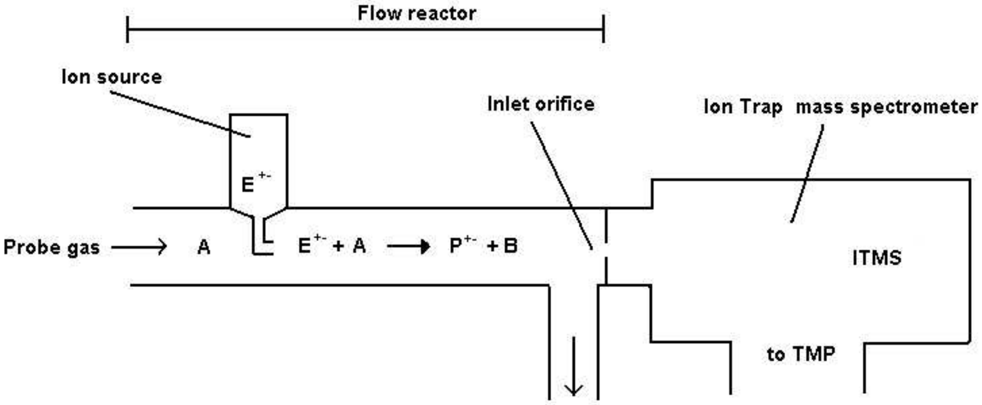

Figure 3.1: A simplified scheme of the instrumental setup for the detection of trace gases, including the flow reactor tube, an ion source and the ITMS [Fiedler, 2004]. A more detailed description is given in section 3.3.

The total concentration of HNO_3 in the flow reactor has to be calculated by including all product ions that arise from HNO_3 reactions with $E^{\pm}$: equation 3.10 adds the contributions from reactions 3.8 and 3.9.

$$[HNO_3] = [CO_3^- HNO_3] + [NO_3^-] \tag{3.10}$$

Further molecules that compete for the educt ion CO_3^- are e.g. $^{32}SO_2$ from the ambient air and $^{34}SO_2$ from the online calibration gas (see section 3.2). The major educt ion from IMR of SO_2 is SO_5^- (these IMR of SO_2 are shown in equations 3.18 and 3.19). The masses of the corresponding educt and product ions are 60 amu (CO_3^-), 123 amu ($CO_3^- HNO_3$), 62 amu (NO_3^-) 112 amu (for $^{32}SO_5^-$), 114 amu (for $^{34}SO_5^-$) and can be seen in the mass spectrum in **figure 5.16**. The water ligands indicated in reactions 3.8 and 3.9 are removed by the collision with helium atoms in the ion trap (section 3.3). The parallel-ACIMS formulae for this example are:

$$[CO_3^- HNO_3] = \frac{1}{k_a \cdot t} \cdot \frac{[123]}{Z} \cdot \ln\left(1 + \frac{Z}{[60]}\right) \tag{3.11}$$

$$[NO_3^-] = \frac{1}{k_b \cdot t} \cdot \frac{[62]}{Z} \cdot \ln\left(1 + \frac{Z}{[60]}\right) \tag{3.12}$$

$$Z = [123] + [62] + [112] + [114]$$

For our calculations k_b from reaction 3.9 is assumed to be equal to the collision rate coefficient. k_a in reaction 3.8 is instead altered to $k_\mathrm{a} = 1{\cdot}10^{-9}$ cm^3 s^{-1}: laboratory experiments in our group by Rainer Nau have shown that k_a lies between 0.5–1$\cdot$10^{-9} cm^3 s^{-1} (personal communication, R. Nau). The rate coefficients usually vary with different degrees of hydratisation of the CO_3^- educt ion, and thus with the humidity in the flow reactor.

The reaction time t is equal to the residence time of the ions in the flow reactor. This ion residence time is calculated from the dimensions of the flow reactor (30 cm length, 4 cm diameter) and the velocity v_FR of the gas flux ϕ_FR. The velocity depends on the pressure and temperature in the flow reactor during the experiment (p_FR and T_FR), and on the flux through a critical orifice that was used to adjust p_FR. The critical orifice was calibrated in the laboratory by using a bubble flow meter. The calibration yielded a linear dependency of the flux on p_FR (in mbar) as in equation 3.13. The square root dependency of the flux on T_FR is stated in [Wutz et al., 2000]: T_cal is the gas temperature during the orifice calibration.

$$\phi_\mathrm{FR} = (-0.49 + 0.13 \cdot \mathrm{p_{FR}}) \cdot \sqrt{\frac{\mathrm{T_{cal}}}{\mathrm{T_{FR}}}} \tag{3.13}$$

Dividing ϕ_FR (= 8.61 l/min for 70 mbar and 300 K in the flow reactor) by the flow reactor tube cross section gives the velocity v_FR (in dm/min, which has to be converted to cm/s). The resulting ion residence time t is of the order of 0.2 seconds.

$$v_\mathrm{FR} = \frac{\phi_\mathrm{FR}}{(4\,\mathrm{cm})^2 \cdot \pi} \cdot \frac{10^3}{60} \tag{3.14}$$

$$t = \frac{30\,\mathrm{cm}}{v_\mathrm{FR}} \tag{3.15}$$

The result of equation 3.10 is the concentration of HNO_3 molecules [HNO_3] in cm^{-3} in the flow reactor. This concentration can be converted to mole fractions (pptv) if the pressure p_FR and temperature T_FR in the flow reactor are known. The pressure p_FR in the flow reactor was set to about 70 mbar, the temperature T_FR usually depends on the ambient conditions, both quantities were recorded during the experiments.

The total number of molecules (N/V) in cm^{-3} in the flow reactor can be determined by the application of the ideal gas law:

$$N/V = N_A \cdot \frac{p_{\mathrm{FR}}}{R\,T_{\mathrm{FR}}} \tag{3.16}$$

N/V			number concentration ($10^{-4}\,\mathrm{cm}^{-3}$)
p_{FR}			pressure in the flow reactor (mbar)
T_{FR}			temperature in the flow reactor (K)
R	$=$	$8.31451\,\mathrm{J}/(\mathrm{K}\cdot\mathrm{mol})$	universal gas constant
N_A	$=$	$6.022045 \cdot 10^{23}\,\mathrm{mol}$	Avogadro constant

For a constant pressure of 70 mbar and a constant temperature of 300 K the result is $N/V \approx 1.7 \cdot 10^{18}\,\mathrm{cm}^{-3}$. Dividing the calculated trace gas concentration $[\mathrm{HNO_3}]$ by this total concentration of molecules yields the mole fraction of $\mathrm{HNO_3}$ in the flow reactor. The unit of mole fractions is independent of pressure and temperature. However, due to memory effects on the interiour walls of the instrument the measured mole fraction in the flow reactor may differ from the real mole fraction of the trace gas in the ambient air.

The calculation of concentrations using the parallel ACIMS formula should involve all product ions that originate from the trace gas of interest. Ignoring some product ions leads to an underestimation of the trace gas concentration.

The mass spectrum in **figure 5.16** indicates another possible candidate for product ions from $\mathrm{HNO_3}$ at mass 124 amu: this mass line may originate from reaction 3.17 of $\mathrm{HNO_3}$ with the educt ion $\mathrm{HCO_3^-(H_2O)_m}$.

$$\mathrm{HCO_3^-(H_2O)_n} + \mathrm{HNO_3} \longrightarrow \mathrm{HCO_3^-HNO_3(H_2O)_n} \tag{3.17}$$

The origin of mass 124 should be verified in further laboratory experiments. Due to uncertainties about the origin of this mass line it has not been included in the $\mathrm{HNO_3}$ calculations of this work. This is one possible error source that leads to an underestimation of the HNO_3 mole fractions.

3.2 Online Isotopic Calibration of Sulfur Dioxide

Our group measures SO_2 with detection limits as low as 10.3 pptv ($2\,\sigma$ of the measured background during the spring 2006 research campaign). This accuracy of our measurements is obtained by using an online calibration method, where isotopically labelled SO_2 of a known mole fraction is injected into the flow reactor. The calibration gas ($^{34}SO_2$) experiences the same IMR as $^{32}SO_2$ which dominates the ambient SO_2. Uncertainties concerning the rate coefficients, the ion residence time, loss to the flow reactor walls of the system, and more are by-passed since $^{32}SO_2$ and $^{34}SO_2$ are exposed to these effects in the same way. The mole fraction of the unknown ambient SO_2 is calculated by comparison with the known mole fraction of the isotopically labelled calibration SO_2.

The IMR of SO_2 with the educt ion CO_3^- in the flow reactor proceeds via reactions 3.18 and 3.19:

$$\mathrm{CO_3^-(H_2O)_n + SO_2 \longrightarrow SO_3^-(H_2O)_n + CO_2} \tag{3.18}$$

$$\mathrm{SO_3^-(H_2O)_n + O_2 + M \longrightarrow SO_5^-(H_2O)_n + M} \tag{3.19}$$

The reaction of SO_3^- with O_2 (reaction 3.19) is rapid compared to reaction 3.18, and thus SO_5^- is detected as the dominant product ion of SO_2. SO_5^- has a mass of 112 amu for $^{32}S^{16}O_5^-$ and 114 amu for $^{34}S^{16}O_5^-$, which is the equivalent product ion from the calibration gas. The water ligands indicated in reaction 3.19 are removed by the collision with helium atoms in the ion trap (section 3.3).

Other product ions from SO_2 are e.g. HSO_4^- at 97 amu and 99 amu. They are not of interest for the calculation of the ambient SO_2 mole fraction because of the online calibration. It was important for HNO_3 to include all product ions in the ACIMS formula calculation, but the isotopic calibration makes such considerations unnecessary for our SO_2 measurements.

The online calibration uses the fact that $^{32}S^{16}O_2$ ($\Rightarrow$ $^{112}(SO_5^-)$) is by far dominating in ambient SO_2. However, it has to be considered that the ambient SO_2 also contains heavy sulfur and oxygen, while the calibration gas contains a specific amount of $^{32}S^{16}O_2$. The fraction of $^{112}(SO_5^-)$ product ions from ambient SO_2 is 93.90 %, while mass 114 amu (mainly $^{34}S^{16}O_5^-$) contributes 5.10 % of the ambient SO_5^- ions (these values can be calculated from the isotope ratios in table 3.1).

The fraction of isotopically labelled SO_2 ($\Rightarrow$ $^{114}(SO_5^-)$) in the calibration gas is slightly different for each gas bottle. The specific values for the bottles that were used during the spring 2006 campaign and the AMMA campaign can be found in table 3.2. These K_{ij} values are calculated from the counting rates on mass 112 amu and mass 114 amu as measured in the calibration gas. They will be used in the calculation of the ambient SO_2 mole fraction.

Sulfur Isotope	Natural Fraction	Oxygen Isotope	Natural Fraction
^{32}S	95.02 %	^{16}O	99.76 %
^{33}S	0.75 %	^{17}O	0.04 %
^{34}S	4.21 %	^{18}O	0.20 %
^{35}S	0.02 %		

Table 3.1: Isotopic distribution of sulfur and oxygen in the ambient SO_2.

SO_5^- fraction		Spring 2006	AMMA
K_{aa}	$^{112}(SO_5^-)$ in the ambient air	93.90 %	93.90 %
K_{sa}	$^{114}(SO_5^-)$ in the ambient air	5.10 %	5.10 %
K_{as}	$^{112}(SO_5^-)$ in the calibration gas	3.28 %	4.98 %
K_{ss}	$^{114}(SO_5^-)$ in the calibration gas	96.72 %	95.02 %

Table 3.2: Isotopic distribution of SO_5^- in the ambient air and in the calibration gas for both research campaigns.

The calculation of the ambient SO_2 mole fraction has been proposed by [Bandy et al., 1993]: The intensity of a mass line is proportional to the sum of the ambient (a) and the calibration standard (s) SO_2 mole fraction on this mass as in equations 3.20 and 3.21.

$$I_a \propto C_\mathrm{a} \cdot \mathrm{K_{aa}} + \mathrm{C_s} \cdot \mathrm{K_{sa}} \quad \text{, Intensity on mass 112} \tag{3.20}$$

$$I_s \propto C_\mathrm{a} \cdot \mathrm{K_{as}} + \mathrm{C_s} \cdot \mathrm{K_{ss}} \quad \text{, Intensity on mass 114} \tag{3.21}$$

C_a total mole fraction of SO_2 that yields mass 112

C_s total mole fraction of SO_2 that yields mass 114

$$R = \frac{I_a}{I_s} = \frac{C_\mathrm{a} \cdot \mathrm{K_{aa}} + \mathrm{C_s} \cdot \mathrm{K_{sa}}}{C_\mathrm{a} \cdot \mathrm{K_{as}} + \mathrm{C_s} \cdot \mathrm{K_{ss}}} \tag{3.22}$$

The ratio R of these intensities (the measured counting rates) is directly used to calculate the unknown mole fraction C_a (equation 3.23).

$$C_\mathrm{a} = \mathrm{C_s} \cdot \frac{\mathrm{R\ K_{ss}} - \mathrm{K_{as}}}{\mathrm{K_{aa}} - \mathrm{R\ K_{sa}}} \tag{3.23}$$

The mole fraction of the calibration SO_2 (C_s) is chosen according to the expected ambient SO_2 mole fractions, such that the counting rates on mass 114 usually exceed those on mass 112 by about one order of magnitude. C_s is determined by the SO_2 mole fraction of the calibration gas (440 ppbv and 500 ppbv for the spring campaign and AMMA-SOP, respectively) and the relative amount of injected calibration gas into the flow reactor (depending on T_FR and p_FR). The injected SO_2 mole fractions were about 575 pptv and 680 pptv (for the spring campaign and AMMA-SOP), which each corresponds to a flux of 11.7 ml/min through the mass flow controller.

An online calibration methode for HNO_3 is currently being developed in our group by Rainer Nau as part of a dissertation thesis. A permeation tube that releases a known amount of isotopically labelled $H^{15}NO_3$ (the naturally dominant isotope is ^{14}N) in a permeation oven is supposed to be included into the instrumental setup. One challenge of this additional online calibration are possible interferences, especially on mass 124 amu, since there is only 1 amu difference in the nitrogen isotopes (in humid conditions the educt ion HCO_3^- (61 amu) becomes important in addition to the otherwise dominating educt ion CO_3^- (60 amu). Under these conditions mass 124 includes at least two product ions $CO_3^-H^{15}NO_3$ and $HCO_3^-H^{14}NO_3$). Another challenge is the technical realization and installation of the calibration.

3.3 Experimental Setup and Mass Spectrometer

Experimental Setup

Figure 3.3 shows a scheme of the instrumental setup inside the research aircraft *Falcon* which is operated by the German Aerospace Centre (Deutsches Zentrum für Luft- und Raumfahrt — DLR) in Oberpfaffenhofen (Ohofen), Germany. The inlet system for atmospheric air is situated on top of the aircraft. A picture of this inlet can be found in **figure 3.2**. It points opposite to the flight direction to prevent particles and droplets from entering the system.

Figure 3.2: The inlet system of the MPI-K CIMS instrument on top of the *Falcon* research aircraft.

The calibration SO_2 line was connected to a 1/2 inch PFA (Perfluoroalkoxy polymer) inlet tube. The mixing of the calibration gas with the ambient air should occur as early as possible downstream of the air intake to ensure equal conditions for the ambient and calibration SO_2 throughout the experiment. The flux of calibration SO_2 was regulated to 11.7 ml/min (Bronkhorst MFC, maximum flux of 20 mln/min, for 1013 mbar and 273 K). A magnetic valve feedback system was used to regulate the pressure p_{FR} in the flow reactor to a constant value of about 70 mbar, while the external pressure varied with the flight altitude (the pressures at different flight altitudes are listed in table A.1). The ion source was located 30 cm ahead of the spectrometer. The constant oxygen supply of the ion source ensured a selective production of O^-, O_2^- and O_3^- ions and O^1D atoms without contamination by ambient air. The stainless steal flow reactor tube between the ion source and the spectrometer had a diameter of 4 cm.

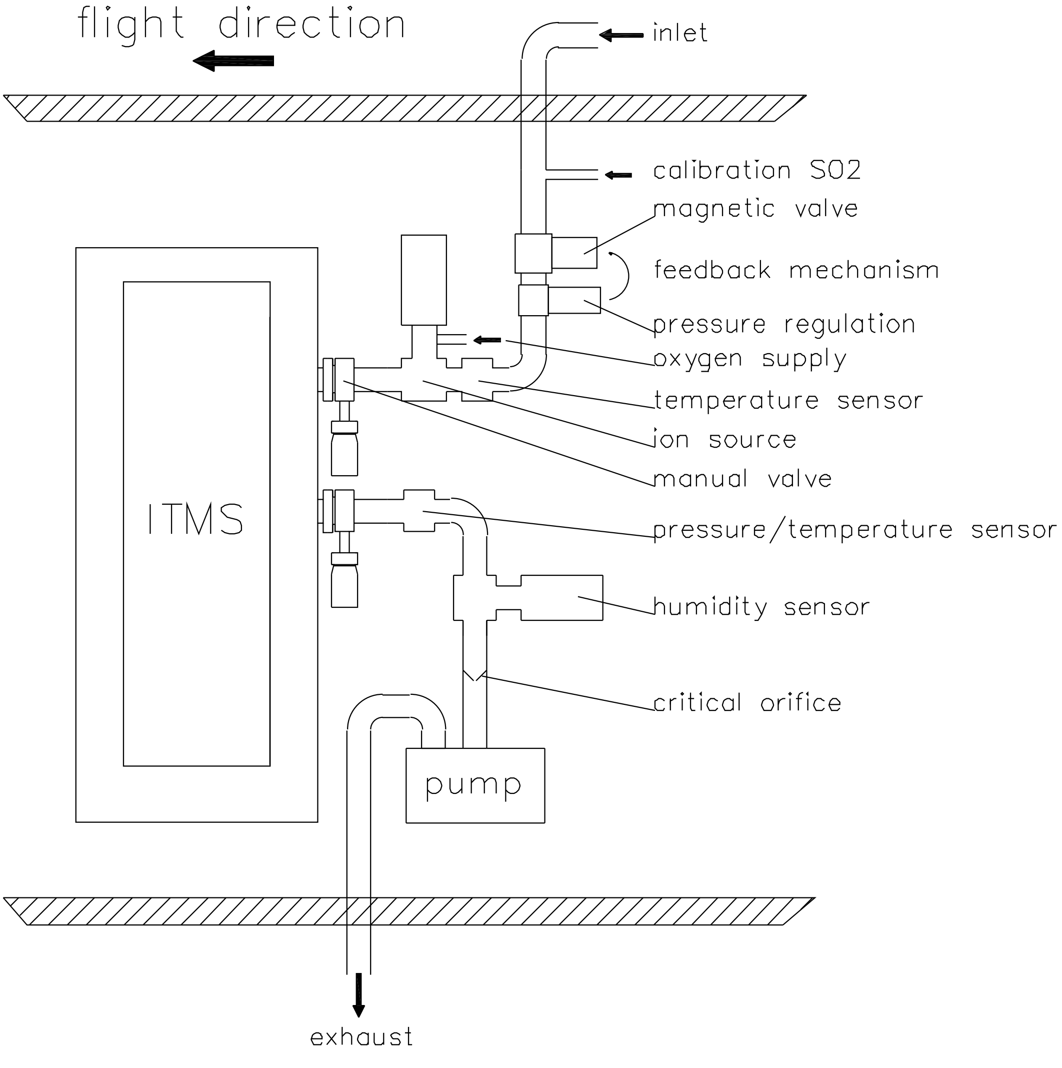

Figure 3.3: Schematic view of the instrumental setup inside the research aircraft. ITMS = Ion Trap Mass Spectrometer.

A mechanical pump was used to suck the ambient air through the inlet system. A critical orifice (4 mm diameter) above the pump in combination with the magnetic valve feedback system ensured a constant flux through the flow reactor, independent of the ambient pressure. The flux through a critical orifice depends only on the temperature and the pressure in front of the orifice. The orifice we used was calibrated with a bubble flow meter to a flux of 8.61 l/min for 70 mbar and 300 K in the flow reactor.

Figures C.2 and C.3 show photographs of the CIMS instrument inside the research aircraft during the AMMA-SOP campaign.

Chemical Ionization Mass Spectrometry (CIMS) Instrument

Our group uses a CIMS instrument equipped with a commercial Paul Ion Trap MAss Spectrometer (PITMAS) by Thermo Finnigan for the detection of trace gases. The CIMS method uses IMR schemes which have been developed by our group. The PITMAS was originally built to measure liquid samples and has been altered by our group for the CIMS measurement of gases. With our settings the instrument produces one spectrum each second. **Figure 3.4** displays a schematic view of the interior of the mass spectrometer.

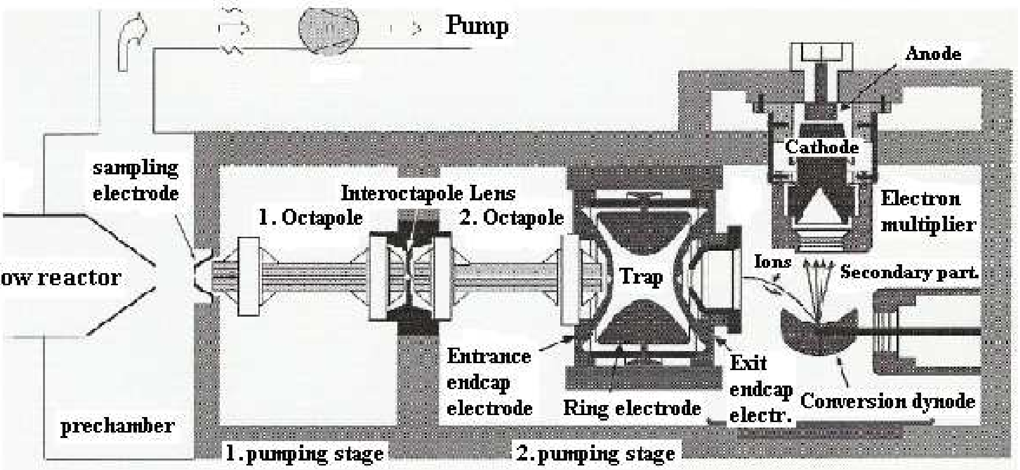

Figure 3.4: Schematic view of the PITMAS instrument [Hanke, 1999].

A circular planar sampling electrode (0.15 mm diameter) separates the prechamber from the spectrometer. The pressure in the flow reactor and prechamber is regulated to a constant value of about $p_{\mathrm{FR}} = 70\,\mathrm{mbar}$, while the pressure behind the sampling electrode at the first pumping stage is as low as 1–2 mbar. A small DC voltage of -5 V to +5 V is applied to the sampling electrode to prevent the ions from colliding with it. They pass through this electrode and are focussed by two octapoles and an interoctapole lense. The counting rate for the desired ion masses can be optimized by varying the voltages on these ion optical devices. The lense between the octapoles can be used to block the ions before reaching the ion trap, depending on the applied voltage and the charge of the ions. The pressure behind the interoctapole lense (at the second pumping stage) is $\leq 0.01\,\mathrm{mbar}$.

The ions are injected into the Paul ion trap through an end-cap electrode during the "injection time" (about 250 ms). The injection time can either be manually set or automatically regulated to the most efficient number of trapped ions ("automatic gain control"). In the ion trap helium is used as a buffer gas. Trapped ions collide with the helium atoms which cools the ions kinetically and excites them internally. The helium also removes water-ligands and dissociates large cluster ions by collisions.

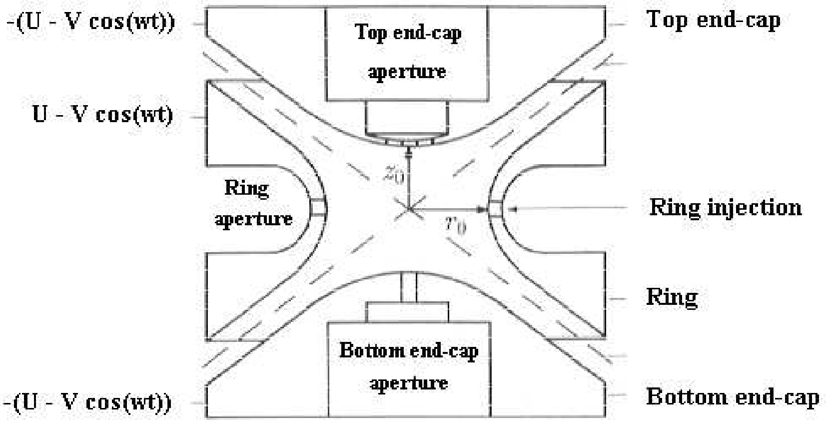

Figure 3.5: A schematic view of the general structure of a Paul ion trap with the applied voltages. Our instrument uses an end cap injection instead of the ring injection shown in this figure.

The ion trap uses a quadrupol field to store the ions, which is created by two hyperboloid end-cap electrodes and a hyperboloid ring electrode (see **Figure 3.5**). An AC voltage ($U - V\cos(\omega t)$) is applied to create the quadrupol field and stabilize the ions in the field according to their equations of motion, the so-called Mathieu equations [March and Hughes, 1989, Paul and Raether, 1955].

Variation of the voltages U and V changes the stability conditions for the ions in the trap. They can be ejected from the trap in a controlled way depending on their mass. By varying the voltages and thus the stability conditions of the quadrupole field the ions are ejected, subsequently generating a mass spectrum from low to higher masses with a certain number of counts (electron signal) on each mass line. The total scan time for one spectrum was 1.1 s with our settings, including 3 microscans with 250 ms injection time each. The ions leave the trap through the second end-cap electrode and hit a conversion dynode, where a high voltage of 15 kV is applied. The conversion dynode emits secondary electrons which are accelerated towards an electron multiplier. The intensities of the electron signals at the multiplier yield a mass spectrum that mirrors the relative amounts of ions with different masses. The mass spectrum of the PITMAS may range from 15–4000 amu. The selected mass range for the measurements included in this work was 50–180 amu.

The "ion fragmentation mode" of the spectrometer can be used to determine the composition of complex ions (large organic ions, volatile organic compounds or cluster ions). The helium atoms in the trap excite the large ions by energetic collisions and split them up into fragment ions. Unknown ions can thus be isolated, and their composition can be investigated. The fragment ions may allow to find the origin of the large product ion that is supposed to be investigated.

3.4 Uncertainties and Error Sources

The measurement of trace gases by CIMS is subject to a variety of uncertainties that originate from statistical variations, instrumental background or systematic errors.

The background of the counting rates of the mass spectrum includes electronic noise from the conversion dynode and the electron mulitplier. It is also possible that a mass line contains ions that are unknown and unwanted (interference) and increase the specific counting rate. These ions may originate from IMR in atmospheric or synthetic air (involving contaminant trace gases from the gas bottle used during the background measurements). The background also includes possible memory effects of the flow reactor walls.

This background was measured during each campaign, using synthetic air of 80 % N_2 and 20 % O_2. The background counting rate on each mass line had to be subtracted from the counting rate that was measured during the experiment. The corrected counting rates were then used to determine the mole fractions via the ACIMS formula (for HNO_3), or using the online calibration method (for SO_2).

For the spring 2006 campaign the average values of the measured background counting rate on the mass lines 62, 112, 114, 123 amu were subtracted from the yields of the atmospheric measurements.

Another measurement was performed using synthetic air, this time including the injection of about 1.3 ppbv calibration gas. The data were corrected using the background counting rates, and lead to the K_{ij} that are listed in table 3.2 and correspond to the relative amounts of $^{34}SO_2$ and $^{32}SO_2$ in the calibration gas ($K_{\mathrm{as}} = 3.28\,\%$ and $K_{\mathrm{ss}} = 96.72\,\%$).

The background mole fraction of SO_2 was determined from this calibrated measurement, using the un-corrected counting rates on masses 112 and 114 for the calculation of the SO_2 mole fractions as described in section 3.2. It yielded an average background of 21.7 pptv and an SO_2 detection limit of 10.3 pptv (two standard deviations of the averaged background).

During AMMA-SOP background measurements were performed on three different days, adding to about 42 minutes of background data. The injection of 680 pptv calibration gas lead to the SO_2 fractions of $K_{\mathrm{as}} = 4.98\,\%$ and $K_{\mathrm{ss}} = 95.02\,\%$ for the calculation of the SO_2 mole fraction. The average SO_2 background mole fraction was 34.2 pptv during for this campaign, with an SO_2 detection limit of 17.2 pptv (two standard deviations of this 27–minutes average).

The calculation of the mole fraction error of SO_2 included a error of $\sqrt{n}$ on a mass line of n counts and an error of the background that had been subtracted from that mass line ($\sigma/\sqrt{N}$ with N = number of background spectra).

The uncertainty of the flux through a mass flow controller is 1 % of the maximum flux (± 0.2 ml/min for the calibration gas). An uncertainty of the calibration of this MFC (3.4 %) was included as well as that of the calibration for the critical orifice (3.9 %). The error of the SO_2 calibration gas mole fraction was 10 %. The fluctuation of the flow reactor pressure was about ± 2 mbar, and the fluctuation of the temperature measurement about 0.3 K.

The error propagation for the SO_2 calculation yielded an relative error of about 20 %, for mole fractions above ∼ 50 pptv as shown in **figures 3.6 and 3.7**. The error for is larger for small mole fractions, especially below the detection limit (10.3 pptv for the spring campaign; 17.2 pptv for AMMA).

The calculated HNO_3 uncertainty was higher (50 % for the spring campaign and 60 % for AMMA) due to the inclusion of more mass lines and the missing online calibration. The error of the ion residence time t was calculated from the uncertainty of the flux through the flow reactor, while the rate coefficient k for reaction 3.8 was assumed to be $(0.7 \pm 0.3) \cdot 10^{-9}$ $\mathrm{cm}^3\ \mathrm{s}^{-1}$. Further uncertainties concerning the HNO_3 calculation have not been included: the possibility of HNO_3 product ion signatures with mass numbers other than 62 and 123 and the uncertainty of the rate coefficient for reaction 3.9 (which was assumed to be the collision rate coefficient). The HNO_3 mole fraction may be underestimated in this work due to additional product ions, e.g. from mass 124 amu.

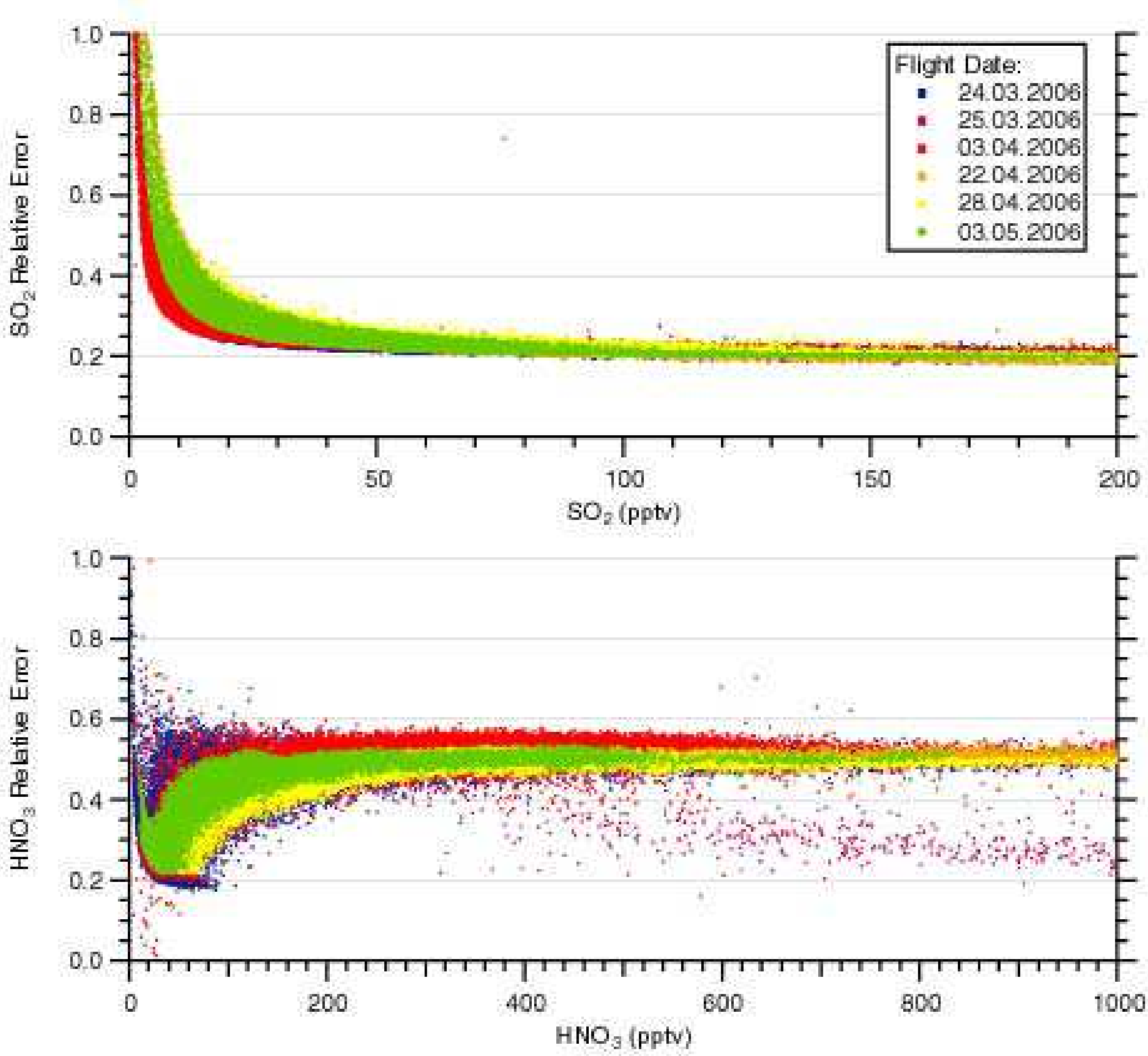

Figure 3.6: Relative error of the SO2 und HNO3 mole fractions vs absolute measured mole fractions for the spring 2006 campaign.

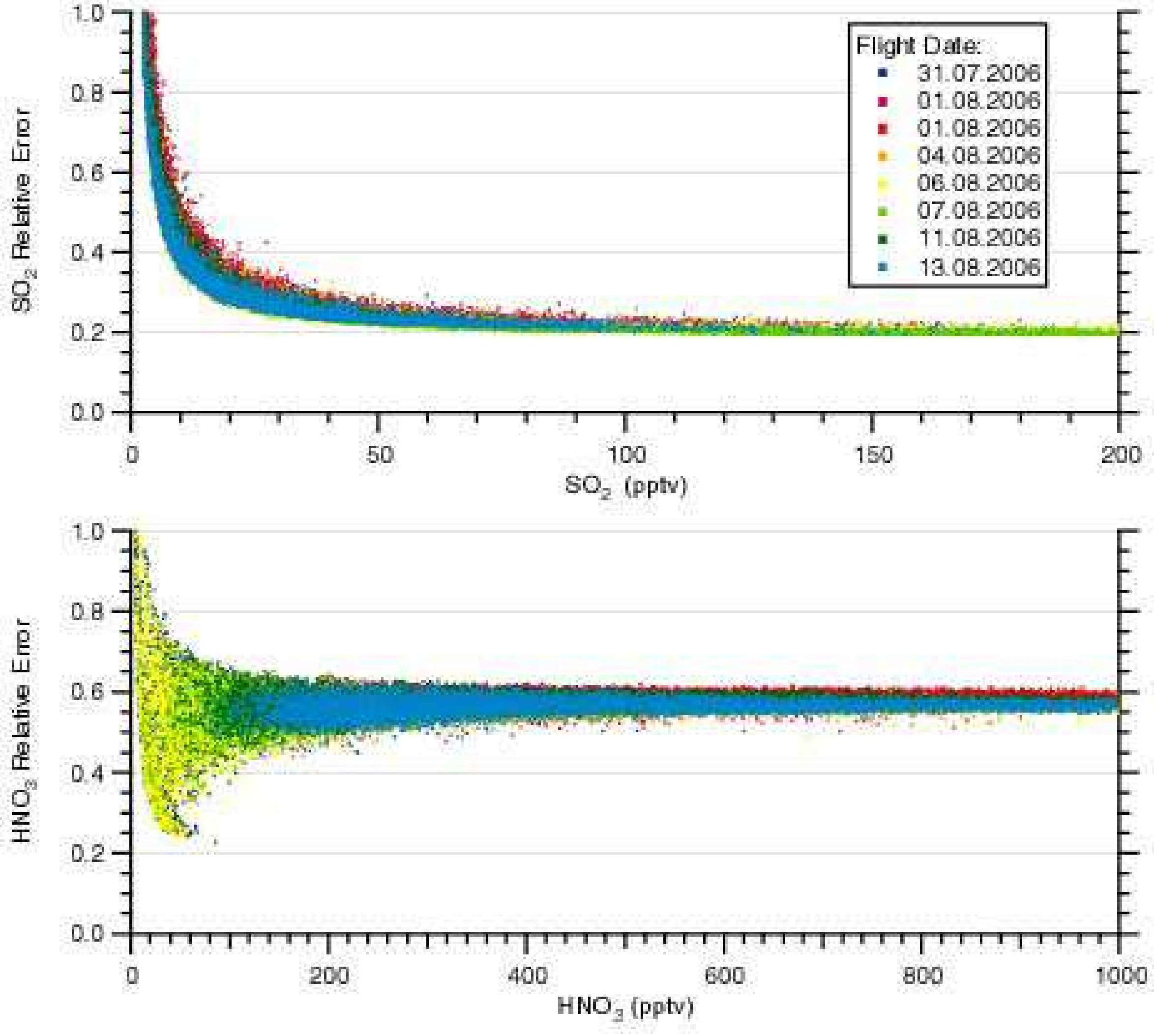

Figure 3.7: Relative error of the SO2 und HNO3 mole fractions vs absolute measured mole fractions for the AMMA campaign.

Chapter 4

Spring 2006 Campaign

Our group participated in an aircraft measurement campaign in spring 2006. This campaign was hosted and operated by the German Aerospace Centre (Deutsches Zentrum für Luft- und Raumfahrt — DLR) in Oberpfaffenhofen (Ohofen), Germany, from March 20th to May 5th. The instrumentation was deployed on the research aircraft *Falcon* (see **figure 5.6** for a photograph of the aircraft) in order to probe atmospheric air masses.

One of three objectives of this campaign was to measure ship emissions as an example of pollution of the marine boundary layer (MBL) by fossil fuel combustion (FFC). The measurements were concentrated around the English Channel and will be referred to as SHIPS. The intention was not to measure individual ship exhaust plumes, but to generally probe the polluted air over the Channel and occasionally encounter single fresh ship plumes. An example of the collected data is briefly discussed in section B.1, but SHIPS results are not of further interest in this work that concentrates on pollution plumes in the free troposphere. The uncommented data can be found in **figures B.10, B.13, B.15 and B.17** for flights during April 3rd, 22nd, and 28th, and May 3rd, respectively.

The second and third objective were measurements of pollution plumes that had been subject to long range transport from North America and Asia (referred to as MEGAPLUME and INTEX). The pollution plumes had travelled eastward from their emission sites on the northern hemisphere and crossed the Atlantic (and Pacific) ocean, experiencing photochemistry and dilution during their journey. The term of long range transport usually refers to transport processes of the order of days and weeks, corresponding to hundreds of kilometers or more. MEGAPLUME (MEGAcity PLUME) was intended to measure pollution arriving over Europe from the megacity Mexico City. Since the research flight hours granted for MEGAPLUME were limited and a Mexico City plume was not in reach, a plume from eastern Asia was probed instead. This plume had been predicted by the FLEXible PARTicle dispersion model (FLEXPART) and was encountered by the research aircraft during the first two flight days of the campaign. The main attention will be given to this pollution plume over the northeastern Atlantic region and Central Europe. This was the first time that an Asian pollution plume was intentionally flown into after predicting its location by model simulations [Stohl et al., 2006]. Data from further flights of the spring 2006 campaign will not be discussed, but plots showing the data can be found in a **figures B.5 to B.18** in chronological order.

Additional data sets from instrumentation onboard the aircraft included basic data aquisition by the *Falcon* and measurements by the DLR Institute of Atmospheric Physics (IPA). *Falcon* data aquisition included aircraft position, velocity and altitude, humidity and other basic environmental data. The IPA gathered data concerning NO and NO_y[1], CO and ozone mole fractions, and different aerosol properties. Technical information about the *Falcon* and the onboard basic data equisition is accessable through the DLR flight facility website *(http://www.dlr.de/fb/desktopdefault.aspx/tabid-527/)*.

A detailed motivation for measurements concerning long range transport will be given in the following section 4.1. The route that the Asian plume of interest took is further described. Section 4.2 includes an overview of the research flights and data sets aquired during the spring campaign.

4.1 Long Range Transport and Asian Plume Propagation

Chapter 2 provided the general motivation for SO_2 measurements by emphasizing its strong impact on H_2SO_4 formation and accordingly on aerosol nucleation and growth. The climate

---

[1] Reacitve nitrogen NO_y includes nitrogen oxides $NO_x (= NO + NO_2)$, HNO_i (i = 2, 3, 4), peroxyacetyl nitrate (PAN) and other nitrates

effects of aerosol have been explicitly discussed in section 2.2.3.

The awareness of the influence of sulfur and aerosol, especially in the upper troposphere and lower stratosphere where the Asian plume was encountered, leads to the main motivation of our measurements. Few pre-existing aerosol particles and low temperatures in these regions favor aerosol formation which may yield an increased number of cloud condensation nuclei (CCN). Our fast and sensitive measurement technique onboard the research aircraft *Falcon* allows the in situ study of these atmospheric air masses.

Transport processes in the atmosphere are driven by temperature gradients. The gradients between the tropics or suptropics and the polar latitudes trigger the global atmospheric circulation [Brasseur et al., 1999, Roedel, 1994]. A fast tropospheric flow of almost no divergence occurs in quasi-barothropic altitudes of about 5–6 km (600–500 hPa) (see appendix A for the conversion between altitude and pressure). Westerly winds extend from about 35° to 70° (N and S) [Roedel, 1994] and exhibit velocities of about 800 km per day [Seinfeld and Pandis, 1998]. Pollution plumes from North America and even Asia that enter these wind fields after upward transport may travel around the globe and finally be detected above Europe. The Asian plume that was encountered took this route across the northern Pacific, Central North America and the North Atlantic. The upward transport at the eastern seaboards of Asia and lifting into the upper troposphere happens via so-called warm conveyor belts (WCB) [Cooper et al., 2004]. There have been reports about plumes crossing the northern Pacific to North America before, e.g. [Tu et al., 2004]. SO_2 enhanced layers have been found, but the measurements only show data for lower altitudes (below 5 km) than those of our Asian plume. The named reference shows how cloud processes can rapidly decrease SO_2 in air masses during long range transport. SO_2 enhanced air masses were usually very dry and displayed little turbulence.

A 9 day back trajectory calculation using HYSPLIT (HYbrid Single-Particle Lagrangian Integrated Trajectory) [Draxler and Hess, 1998, Draxler and Rolph, 2003] illuminates the history of such air masses in general and of the observed Asian plume in particular (**figure 4.1**).

The plot shows that the air mass measured on March 24th left the east coast of China around March 18th after crossing China in about 5 km alititude. It moved to the Pacific, passing around the south of Japan, and was lifted to 10 km during March 19th. The highest sections of the journey were over the North Pacific, where the air mass rapidly travelled towards North America. It moved south along the west coast before crossing the American continent

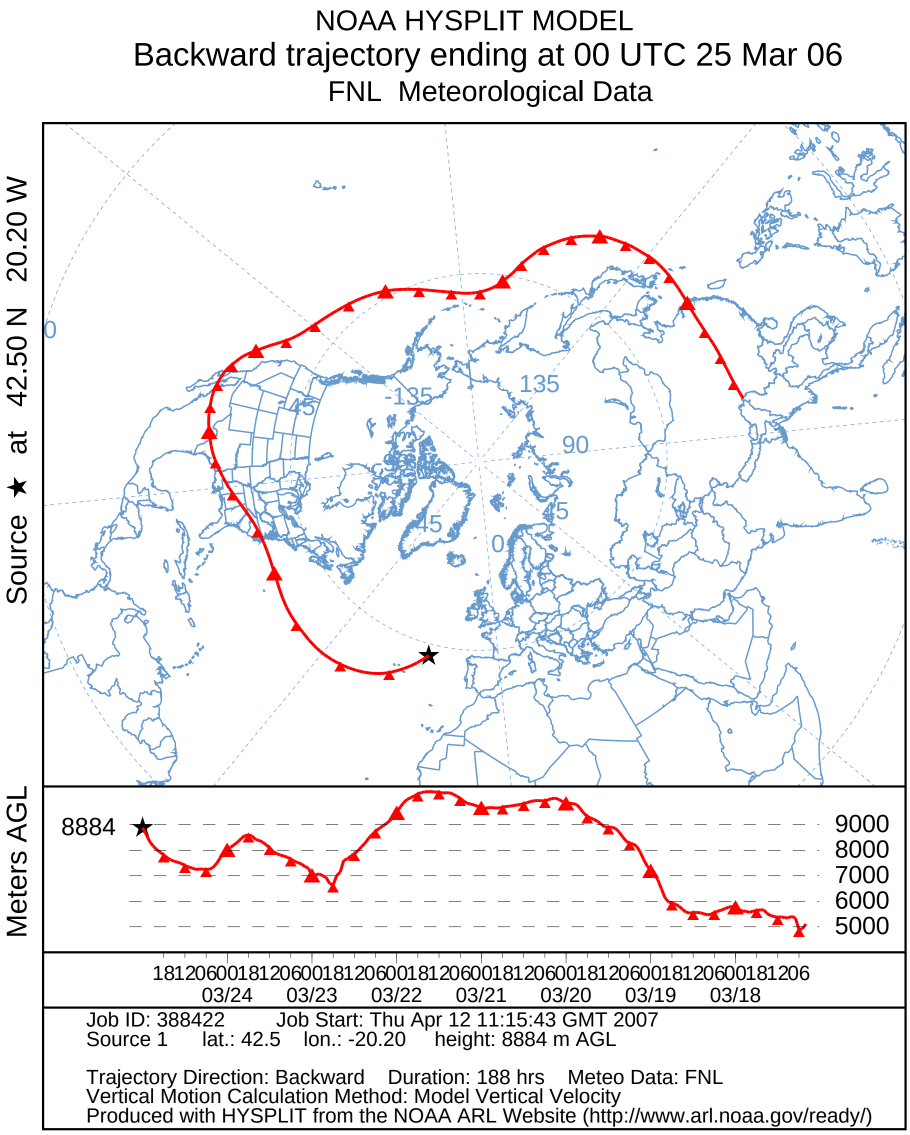

Figure 4.1: HYSPLIT 9 day back trajectory [Draxler and Hess, 1998, Draxler and Rolph, 2003], starting on March 24th at 13 UTC at an altitude of 8884 km at position of the research aircraft at 12:46 UTC.

in altitudes of 7–9 km. The endpoint of the trajectory at almost 9 km was reached after rapid crossing over the North Atlantic. Stohl et al. [2006] uses the FLEXPART model that generally supports the results of this single trajectory calculation, and states that the journey from the east coast of Asia to the west coast of Europe took only 7 days. Midlatitude westerly winds are especially strong in springtime, which is why transport from East Asia across the Pacific is generally most intense during this season [Tu et al., 2004].

Polluted air that travels the atmosphere for about a week is influenced by physical and chemical processes. Depending on the encountered ambient air masses the pollution trace gases experiences dilution, chemical conversion, and removal processes by clouds.

The average lifetime of SO_2 with respect to the reaction with photochemically produced OH is about one week in sunny conditions. Since one week was also the time that our Asian plume took to reach Europe, low values for pollution SO_2 in this plume are expected. Photochemistry occured in the altitude ranges of the observed Asian plume ($\sim$5–9 km) and contributed to gas phase oxidation processes that removed SO_2.

Additional removal of SO_2 from the gas phase happens in the presence of clouds. The relative amount of SO_2 found in the liquid phase is of the order of a few percent of gaseous SO_2 (see section 3.18), generally decreasing for lower temperatures, but formation of HSO_3^- enhances the SO_2 uptake in cloud droplets as described in section 2.2.1. While SO_2 generally decreases with time, other species like ozone and HNO_3 are produced in the plume due to the NO_x ($NO + NO_2$) chemistry.

Pollution plumes are usually traced by their CO content, a combustion product due to insufficient oxygen supply. Long lived tracers like CO are transported and distributed throughout the hemisphere by long range transport. The lifetime of CO in the atmosphere is about 1 month in the tropics, 4 months in midlatitudes in spring and autumn and even longer in high-latitude winter [Seinfeld and Pandis, 1998].

The Asian plume had originally been identified using CO as a tracer in model calculations by Stohl et al. [2006]. CO mole fractions in plumes are generally increased, which makes it easy to distinguish between the plume and stratospheric air, where CO is strongly decreased (see CO data in **figure 4.6 and 4.7**).

The FLEXPART particle dispersion model by A. Stohl is generally applied to calculate global transport processes, and it specifically predicted the propagation of our Asian plume. For a forward trajectory FLEXPART releases so-called tracer particles at the emission site and calculates their trajectories using the mean winds interpolated from the meteorological input fields plus random motions representing turbulence [Stohl et al., 2006]. We use the feature of calculating back trajectories that track emission particles to their source regions. Satellite measurements of CO can be employed to verify the model simulations. A back trajectory calculation using FLEXPART identifies the source regions of the measured Asian plume (**figure 4.2**). Both model calculations, HYSPLIT and FLEXPART, refer to the same position of the *Falcon* during the second flight of March 24th, later named flight B.

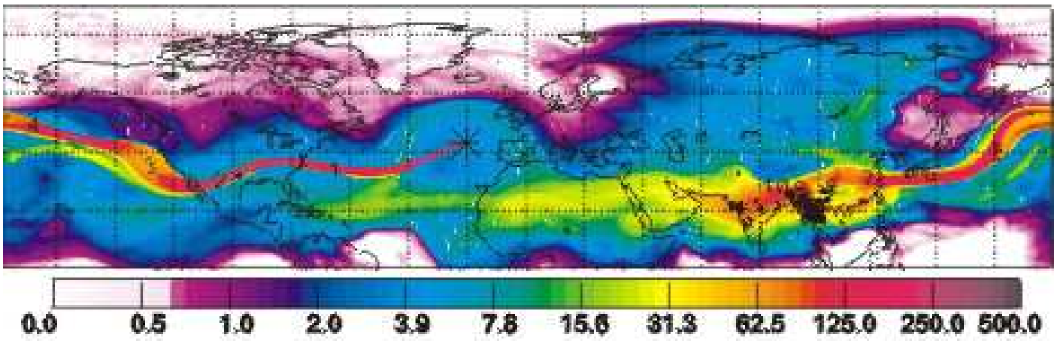

Figure 4.2: FLEXPART results of backward trajectory calculation for flight A, altitude 315 hPa and time segment 12:46–12:48 UTC. The asterisk denotes the aircraft position [Stohl et al., 2006]. The unit of the column integrated potential emission sensitivity function (ns m/kg) refers to an inverse flux of tracer particles (mass/time), integrated over the depth of the atmosphere, which yields the length unit.

4.2 Campaign and Methods

Our experimental setup was fitted into the research aircraft Dassault *Falcon* 20 E5, which is operated by the DLR in Ohofen. All flights were launched from the DLR airbase, partly including stopovers in France or Spain, which resulted in three flights during one day. Shuttle flights were mainly used to probe stratospheric air at the maximum flight altitude of the *Falcon* of 12800 m. **Figure 5.6** shows the *Falcon* research aircraft during the AMMA campaign in West Africa (chapter 5).

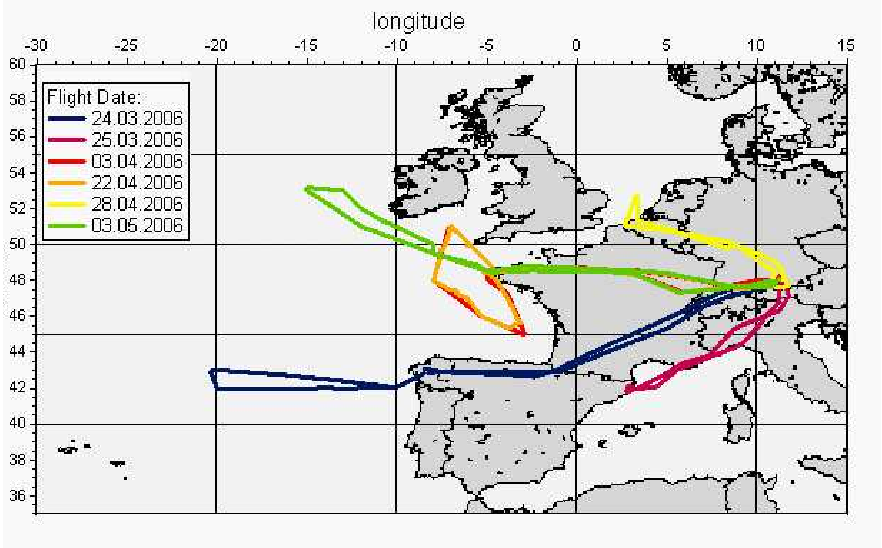

Figure 4.3: Flight paths for all flights performed during the spring 2006 campaign. The two southernmost flights of March 24th and 25th encountered the Asian plume of interest.

Table 4.1 shows the timeframes and objectives of all *Falcon* flights during the spring 2006 campaign time period (from March 24th to May 3rd 2006). A geographical overview of the flight routes is displayed in **figure 4.3**.

4.3 SO_2 Data

This chapter is concerned with the data collected during the first two flights of the campaign, when we encountered a pollution plume from Asia predicted by the FLEXPART model. The model was used as a forecast tool to guide the *Falcon* into the plume area. In the following these two flights will be referred to as flight A (second flight of March 24th) and flight B (flight of March 25th). The measured SO_2 mole fractions of flights A and B are shown in **figures 4.4 and 4.5**. The plots include HNO_3 mole fractions, calculated from our data by using ACIMS (section 3.1), trace gases measured by the DLR (O_3, CO, NO and NO_y), and the flight altitude. O_3 mole fractions of > 100 ppbv indicate stratosphere penetration e.g. during

Date	Start	End	Purpose	Flight Route
24.03.2006	07:10	09:45	NA plume	Ohofen — Santiago
	10:50	14:20		North Atlantic
	15:45	17:55		Santiago — Ohofen
25.03.2006	08:40	12:25	Asian plume	Ohofen — Mediterranean Coast — Ohofen
03.04.2006	07:55	09:50	SHIPS	Ohofen — Brest
	10:35	13:55		English Channel — Bay of Biscay
	15:15	16:55		Brest — Ohofen
22.04.2006	06:05	08:15	SHIPS	Ohofen — Brest
	09:10	12:35		English Channel — Bay of Biscay
	13:35	15:15		Brest — Ohofen
28.04.2006	10:20	13:50	NA plume and SHIPS	Ohofen — English Channel — Ohofen
03.05.2006	06:00	07:40	NA plume	Ohofen — Brest
	08:55	12:10		West of Ireland
	13:45	15:25		Brest — Ohofen

Table 4.1: Overview of all flights of the spring 2006 campaign. Flight days started and ended in Ohofen, refuelling took place in Brest (french Brittany) or Santiago de Compostela (northwestern Spain). NA plume = North American plume. Times are in UTC (local time -1h).

flight B around 09:30 UTC. All displayed SO_2 and HNO_3 data are averaged over 30 seconds, corresponding to up to 660 m of travelled distance in an altitude of 10 km during level flight (at 220 m s^{-1}).

An obvious increase of SO_2 in regions of ozone mole fractions that indicate stratosphere penetration will be briefly discussed in the following section. We probed stratospheric air during all shuttle flights from Ohofen to Santiago and Brest, and during the single flights of March 25th and April 28th. (See **figures B.5 to B.18** for all flights from March 24th to May 3rd 2006.)

The polluted boundary layer (BL) during flight B is indicated by a strong increase in SO_2 up to values of 800 pptv at the Costa Brava, northeastern Spain. The *Falcon* data state a height above ground of about 5 m which seems very low (data from the aircraft´s radio altimeter, a radar system usually used to support landings). The lowest point of the dive (at 41.9° N — 2.76° E) is about 30 km inland, where a motorway follows the coastline (the E 15).

The city of Barcelona is only about 150 km to the southwest of this point, and industrial areas in the vicinity of the city may have contributed to pollution as well. We performed a dive from above 8 km down to almost ground level in this region to gain a representative altitude profile of trace gases and aerosol concentrations.

Figure 4.5 shows some major features of HNO_3 data: a significant increase in the stratosphere as around 09:40 UTC or 11:15 UTC during flight B, and an increase in the polluted BL at higher altitudes than it is observable in the SO_2 data. While SO_2 mole fractions increase rapidly from about 1.4 km downward during the dive, the HNO_3 increase already starts from 4.8 km downwards (referring to the altitudes where mole fractions reach twice the averaged background value). The BL pollution over the Costa Brava and possible sources have been briefly mentioned, but further discussions will focus on the Asian pollution plume in the free troposphere.

4.4 Interpretation and Discussion

The results of our SO_2 measurements and a comparison with other trace gases are presented in **figures 4.4 and 4.5**. The assumed areas of plume penetration will be discussed in this section, and are visualized in **figures 4.6 and 4.7**. The discussion will focus on the Asian plume, while the North American plume (indicated by blue shading in **figure 4.6**) is of minor interest at this point. It travelled at lower altitudes and was mostly separated from the Asian plume that will be the main issue the following. Regions of Asian plume penetration are shaded green in **figures 4.6 and 4.7**. These regions have been deduced from measured CO data and adopted from [Stohl et al., 2006].

The Asian plume does not show significantly higher SO_2 mole fractions than the presumably not effected air masses. An exception is the SO_2 enhancement during flight A around 12:45 UTC. But encountering the plume cannot be verified from our SO_2 data alone. The same is true for HNO_3. Still, when comparing these mole fractions to other measured species we may identify features of plume air (shaded areas in **figures 4.6 and 4.7**).

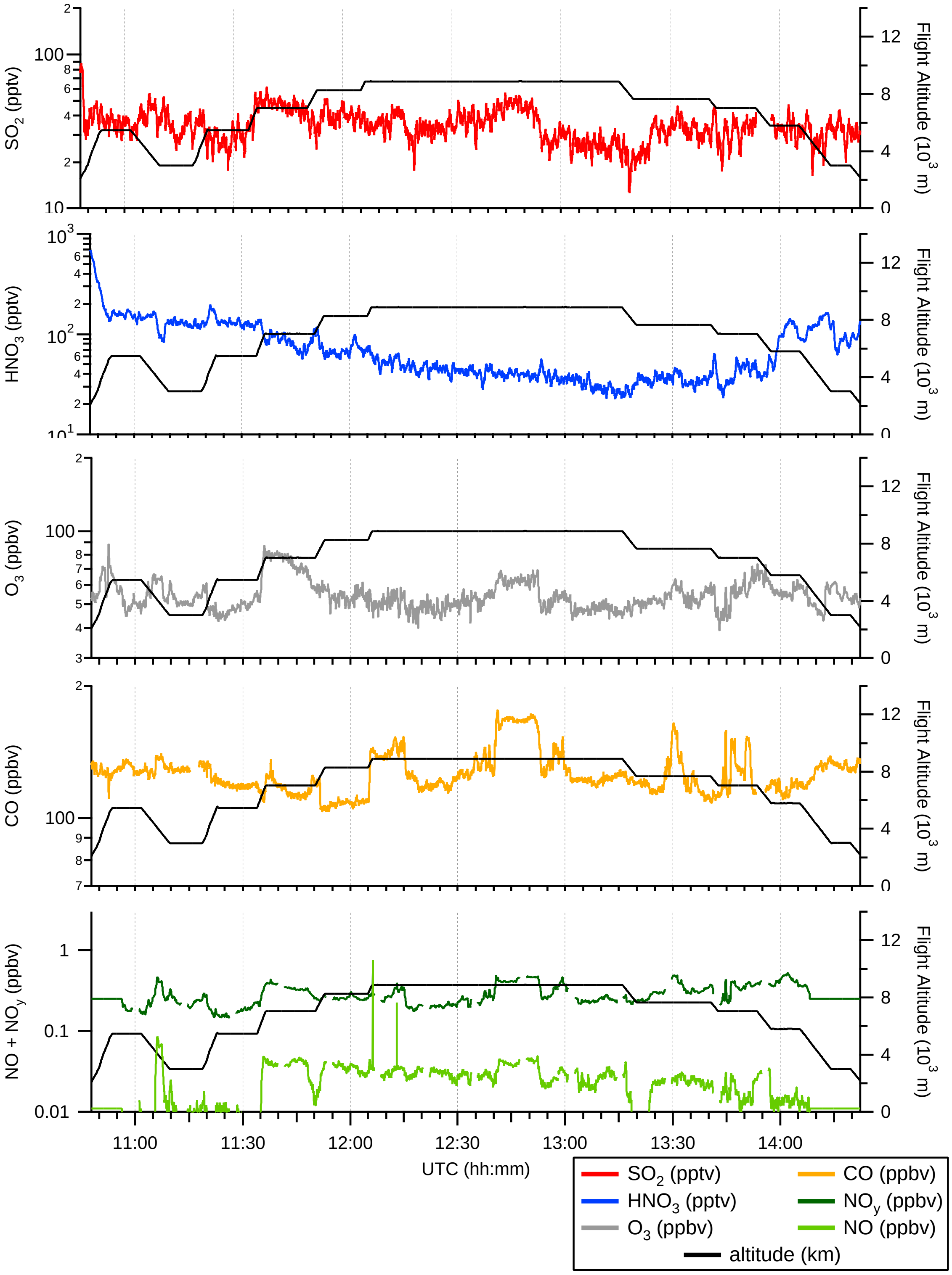

Figure 4.4: SO_2 and HNO_3 by MPI-K, O_3, CO, NO, NO_y and altitudes by DLR IPA for flight 2 during March 24th → flight A.

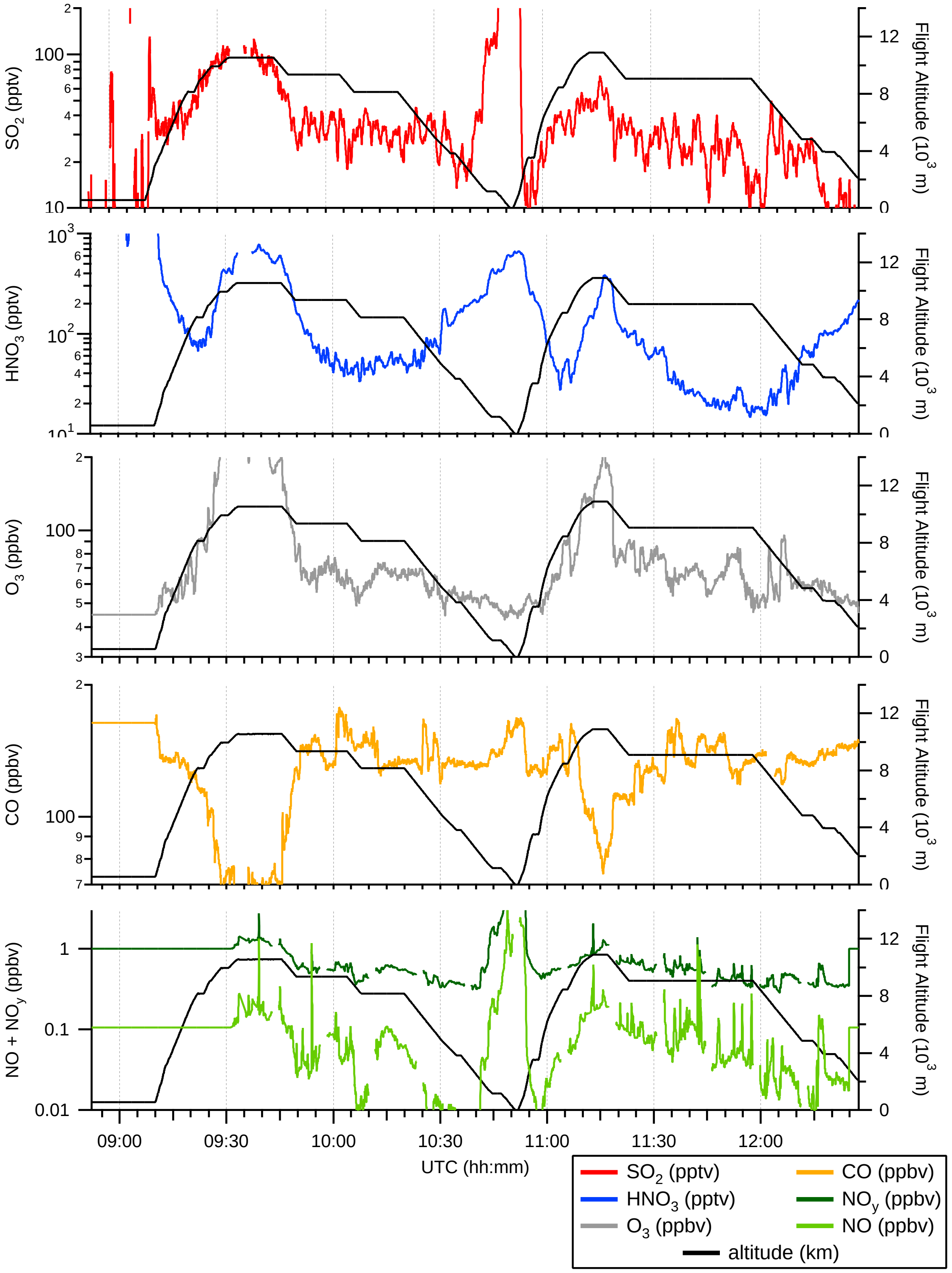

Figure 4.5: SO_2 and HNO_3 by MPI-K, O_3, CO, NO, NO_y and altitudes by DLR IPA for the single flight during March 25th → flight B. The stratospheric and boundary layer data have been partly cut of since they are not of interest for the further discussion. See figur B.8 for different trace gas scales.

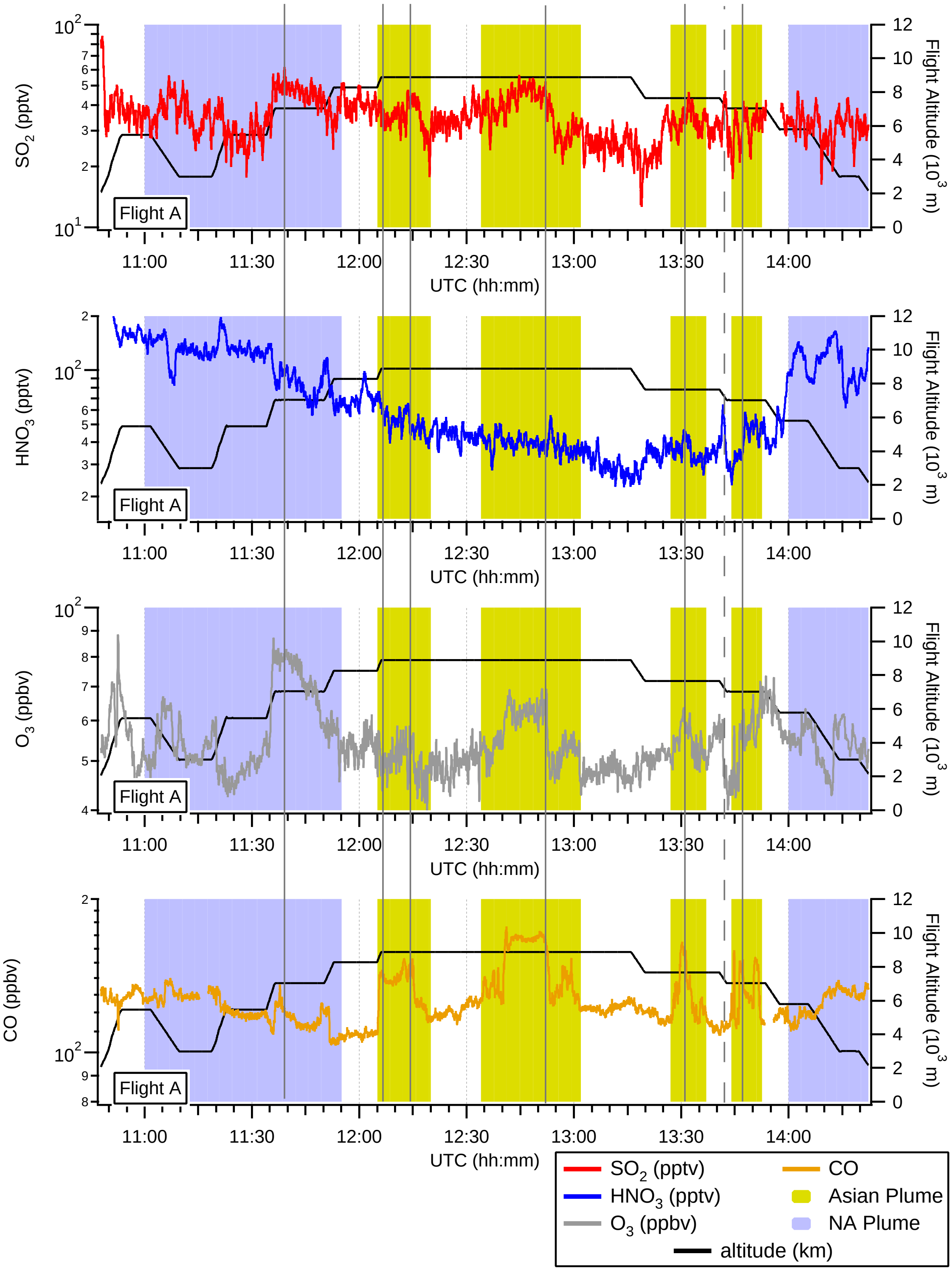

Figure 4.6: Plumes from March 24th → flight A. NA plume = North American plume. The indicated plume locations arise from measured CO tracer data (shaded areas). Solid black lines show parallel increases in SO_2, HNO_3 and O_3 (by DLR) in plume air. Dashed black lines show increases in SO_2, HNO_3 and O_3 outside the plumes, while CO is decreased.

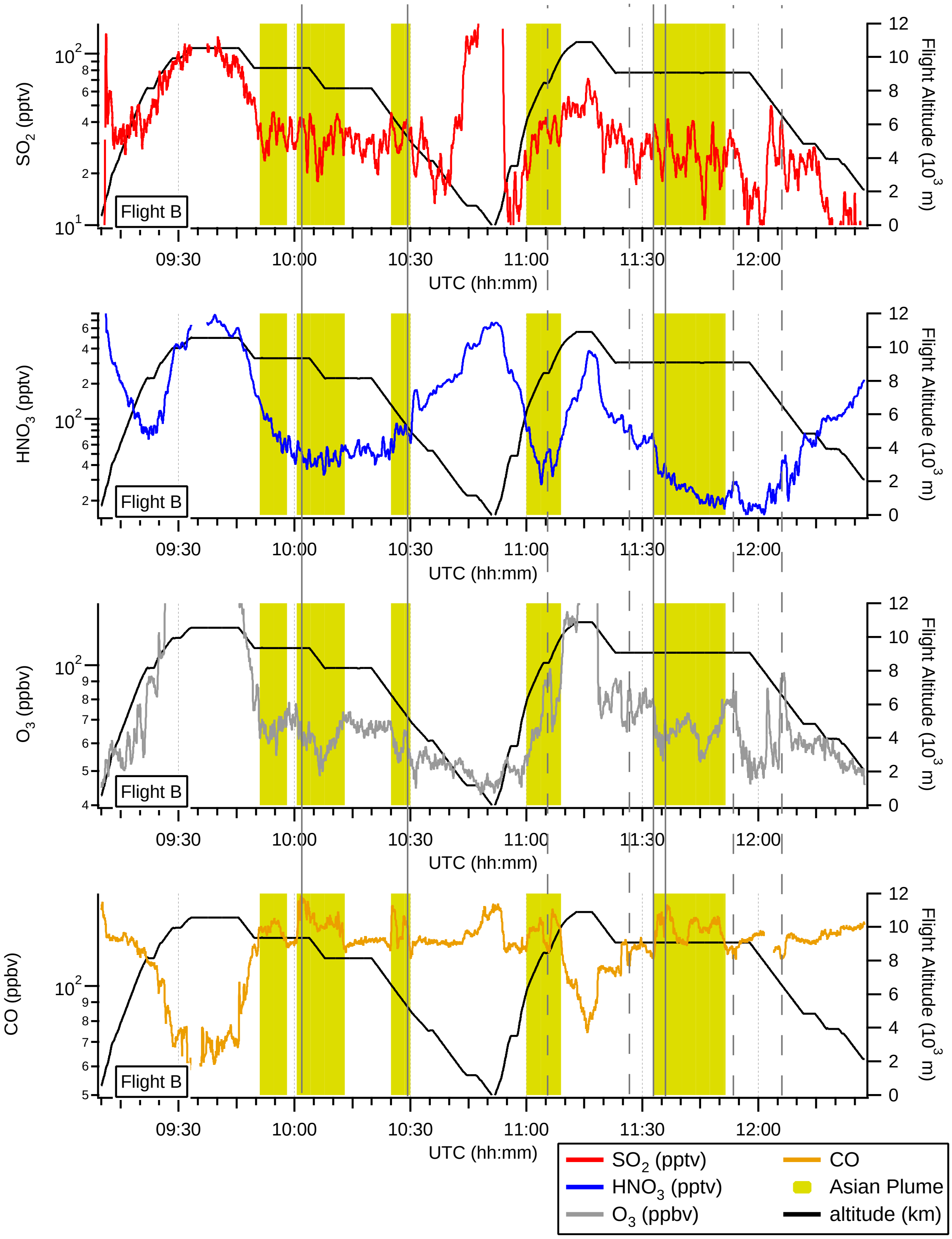

Figure 4.7: Plume from March 25th → flight B. The indicated plume locations arise from measured CO tracer data (shaded areas). Solid black lines show parallel increases in SO_2, HNO_3 and O_3 (by DLR) in plume air. Dashed black lines show increases in SO_2, HNO_3 and O_3 outside the plumes, while CO is decreased. Decreases in CO below 100 ppbv and out-of-range O_3 values indicate stratosphere penetration.

SO_2 and O_3 show similarities in the areas indicated as Asian or North American plume. Some example features are marked by solid black lines in **figures 4.6 and 4.7**, especially conspicuous at 12:50 UTC during flight A or just before 10:30 UTC during flight B. Air masses that are not supposed to be influenced by plume air do not generally show this behaviour (exceptions during flight B are marked by dashed black lines). All marked examples show slightly elevated HNO_3 as well, except for the one at 12:50 UTC during flight A, where a HNO_3 peak occurs only slightly after the broad plume maximum of the other trace gases.

Obvious similarities between SO_2 and O_3 in areas of plume air and differences outside suggest a connection between the two trace gases: they have been in the same plume air mass for some time (see **figure 4.8**).

Outside the plume regions SO_2 and O_3 do not show the same degree of correlation, or they even exhibit opposite behaviour. One example is a decrease in SO_2 during flight A around 13:20 UTC that the other displayed species do not share (NO shows a similar behaviour in **figure 4.4**).

Dashed black lines in **figure 4.7** (and for one occasion in **figure 4.6**) outside plume regions denote areas, where obvious similarities between SO_2 and O_3 occur without expecting plume air to be present. CO values are low during these sections of enhanced SO_2, HNO_3 and O_3. Similar features in the three trace gases outside the plume regions and low CO may thus indicate that SO_2, HNO_3 and O_3 have a common (stratospheric) source, where stratospheric air masses have presumably mixed into the troposphere. These features seem to accumulate during the second leg of flight B.

HNO_3 generally exhibits stratospheric enhancement like O_3 (see stratosphere penetration in **figures B.5 to B.18**) and thus supports the statement of mixing. A general comment on our stratospheric SO_2 measurements can be found at the end of this chapter.

Other features of the measured data remain unclear: decreased HNO_3 alongside with SO_2 and CO peaks, parallel HNO_3 and CO peaks while O_3 and SO_2 are decreased, and others. Origins of some sections of the measured air masses could be identified while others are

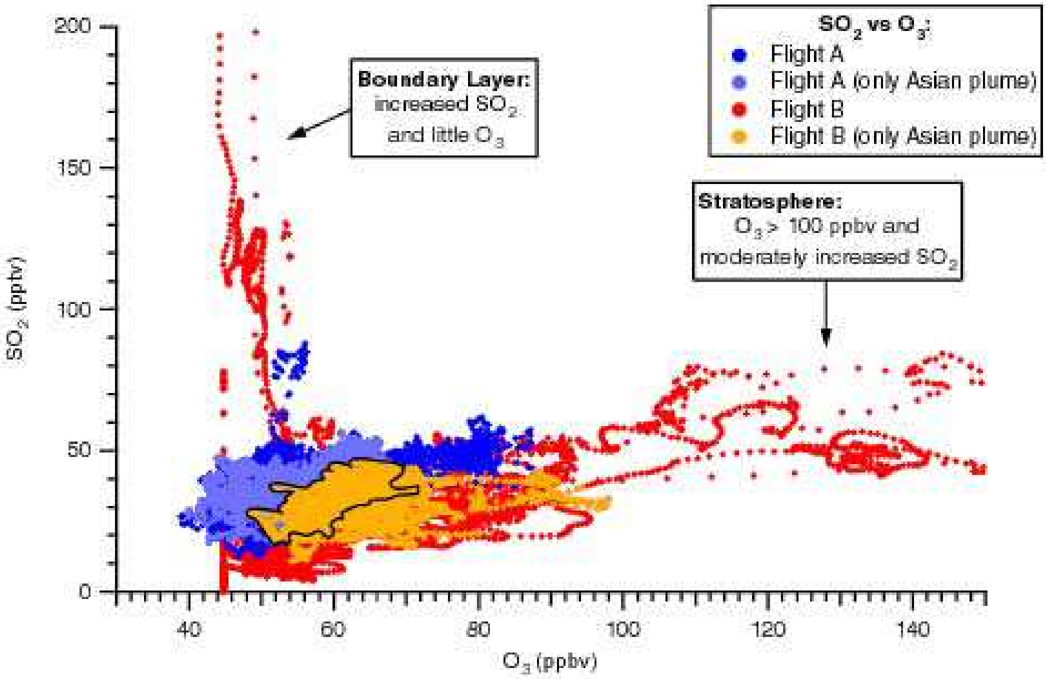

Figure 4.8: Scatterplot of SO_2 vs O_3 for flights A and B. Regions of boundary layer and stratospheric air masses are indicated. The framed area shows where Asian plume air data from both flights overlap.

uncertain. This was expected, at least for flight B, since turbulent weather due to a low pressure trough over Central Europe affected the mixing of the free troposphere on March 25th where the Asian plume was met.

How did turbulence and mixing in of stratospheric air influence the SO_2 mole fractions in the plume? The scatterplot in **figure 4.8** shows values for SO_2 and O_3 during both flights. There is no certain chemical correlation between the two species since their history differs: additional ozone was produced from NO in the plume during its journey [Stohl et al., 2006], while the SO_2 content of the pollution should have decreased due to oxidation chemistry.

However, the scatterplot shows a different interesting result. The SO_2 in the plume area slightly decreases (by ∼10 pptv) while ozone mole fractions become somewhat higher (by ∼10–15 ppbv) for flight B compared to flight A. The shift in ozone may result from mixing in of stratospheric air.

SO_2 mole fractions show no indication of stratospheric air (an increase would be expected, see the last part of this section), instead SO_2 decreases by about 10 pptv. The decrease in SO_2 during the 1-day interval between flights A and B is a result of atmospheric turbulence and dilution as well as oxidation processes. A weather forecast for March 24th (displayed in **figure B.3**) shows a low pressure trough with clouds and precipitation over Central Europe. The plume arrived over Central Europe on March 25th, when the weather situation favored washout and liquid phase oxidation of SO_2. Even if the SO_2 content had previously increased by mixing with stratospheric air, this increase has been strongly reduced again and is not observable.

An altitude profile for flight B clearly displays features of stratospheric air mixed into the plume. The ascending leg of the displayed altitude profile (**figure 4.9**) indicates a layer of stratospheric air with increased ozone and decreased CO around 8.5 km altitude. Such a layer could not be observed during the descent. The corresponding feature in **figure 4.7** is an O_3 peak around 11:05 UTC (flight B), which is likely to be stratospheric ozone mixed into the plume layer. As can be seen in **figure 4.9**, the stratospheric layer of about 500 m depth also shows increased HNO_3 like other stratospheric measurements during the campaign. But not only did stratospheric air mix into the plume, polluted plume air in return mixed into the stratosphere, influencing the stratospheric content of trace gases and aerosol over Europe.

Model calculations as in **figure 4.1 and 4.2** show that the sources of the Asian pollution plume are located from India across China, over which the plume crossed at low altitudes [Stohl et al., 2006] (see **figure 4.1** for a HYSPLIT plot). To verify the pollution sources the EDGAR emission inventory [Olivier and Berdowski, 2001] (Emission Database for Global Atmsopheric Research) gives emission data for different chemical species, e.g. SO_2, and for different source types. **Figure 4.10** shows a selection of SO_2 sources with high contributions in the regions of interest.

The major contribution from the region of China is generally due to industrial FFC, which also has the highest maximum emission value (**figure 4.10b**). The Asian plume

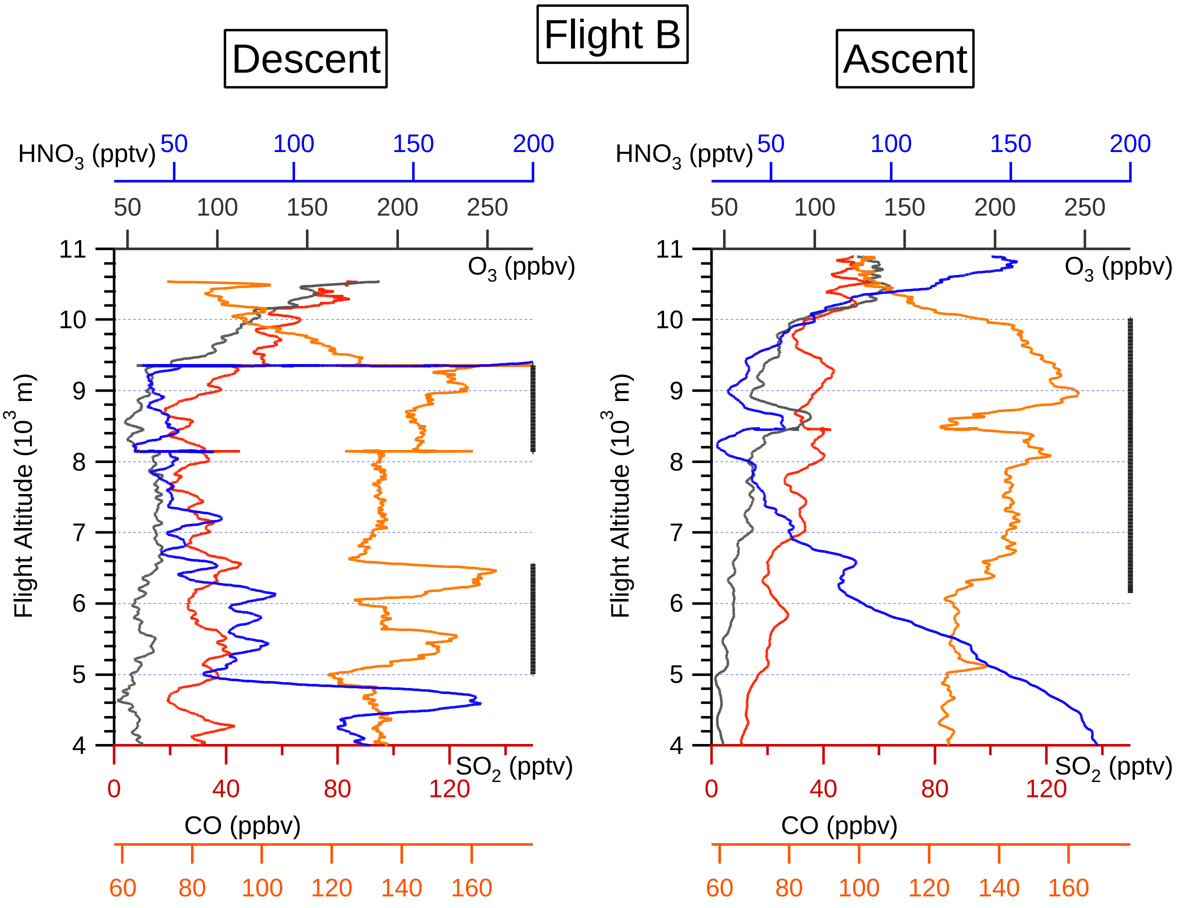

Figure 4.9: Flight B: altitude profiles for SO_2, HNO_3, O_3 and the tracer CO, measured by the DLR IPA. The left graph shows part of the descent from 09:45–10:35 UTC, the re-ascent from 11:00–11:15 UTC is displayed in the right graph. The stratospheric HNO_3 mole fractions in the ascent graph go up to 570 pptv at the highest point of the flight and are cut of from about 9.4 km upwards in this figure. The black bars on the right side of each graph indicate the Asian plume according to figure 4.7.

that we intercepted was characterized as a mixture of BB and FFC pollution. Estimates of the contributions of fires are very uncertain though, due to a lack of data about sizes and locations. The mixing of BB and FFC is typical for pollution outflow from Southeast Asia [Stohl et al., 2006]. According to EDGAR, BB emissions from wood- and savanna-fires mostly arise from Southeast Asia (**figure 4.10d and 4.10e**). India is indicated to be a strong source of industrial and residential BB (**figure 4.10a and 4.10c**).

The EDGAR database contains annual averages of emission values. The database gives one value for each pair of integer latitude and longitude (this leads to a maximum cell size of about 1140 x 1120 m at the equator).

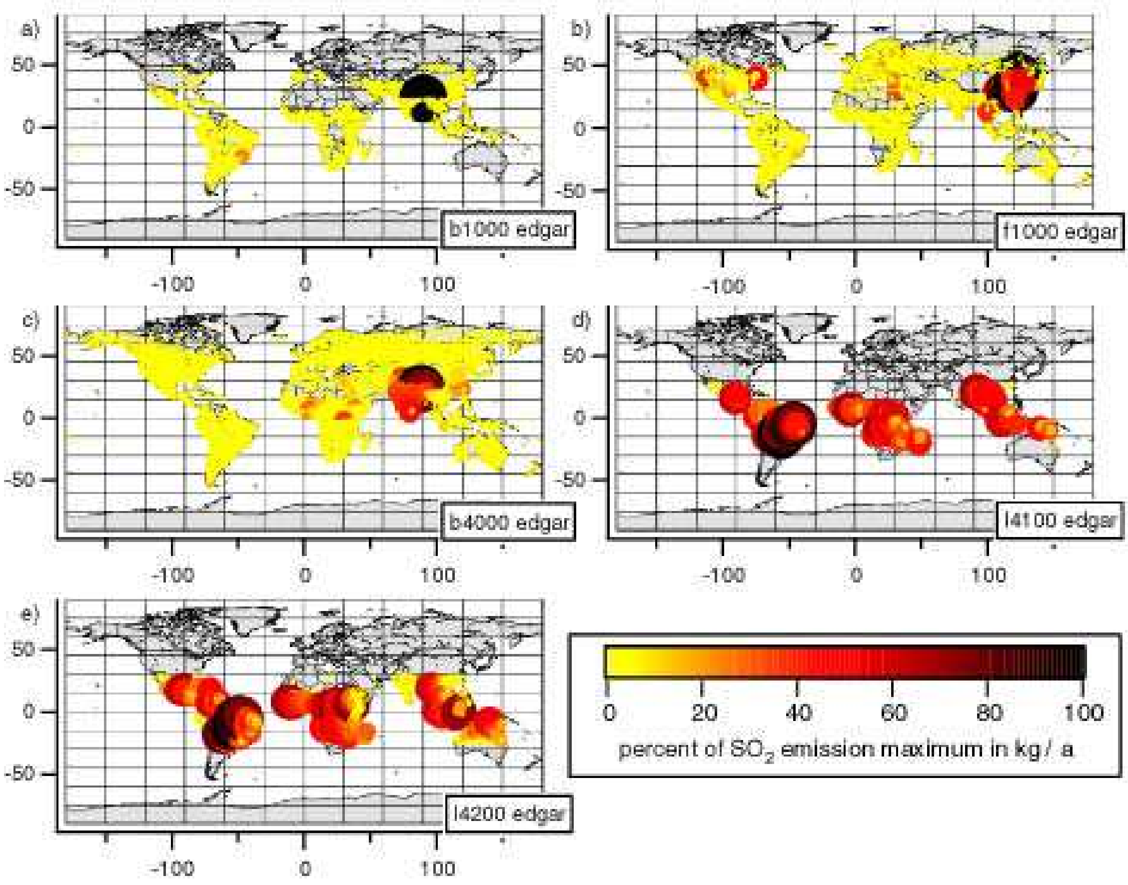

Figure 4.10: Global emission data for SO_2 from the EDGAR database, based on the year 2000. The colorcoding refers to the SO_2 emissions in percent of the emission maximum for each source. Maximum values in kg SO_2 per year are a) $1.083{\cdot}10^7$; b) $5.881{\cdot}10^8$; c) $1.895{\cdot}10^7$; d) $7.810{\cdot}10^6$; e) $7.370{\cdot}10^6$ [Olivier and Berdowski, 2001].

- Biomass burning (BB) emissions from industrial sources (b1000 → a)
- FFC emissions from industrial sources (f1000 → b)
- BB emissions of residential origin (b4000 → c)
- BB emissions from deforestation (l4100 → d)
- BB emissions from savanna fires (l4200 → e)

Stratospheric SO_2 Measurements

Ozone values above 100 ppbv indicate penetration of the stratosphere during research flights and have been observed to be accompanied by enhanced SO_2 and HNO_3 mole fractions during the spring 2006 campaign. This can be seen e.g. during flight B on March 25th from 09:25–09:50 UTC and 11:10–11:20 UTC in **figure 4.5**.

At this point it is not clear whether high stratospheric SO_2 mole fractions are a real atmospheric feature, artefacts from O_3 related SO_2 release from the flow reactor walls (memory effects), or whether they are somehow connected to the presence of increased ozone mole fractions. Different solutions have been discussed concerning the question of stratospheric SO_2 enhancement.

It seems that the measured counting rate of mass 112 is affected by stratosphere penetration during research flights (or probably by enhanced ozone mole fractions) while mass 114 does not show any similar behaviour. If some memory effect concerning the flow reactor walls of the system should exist for SO_2, and if a release would be induced by ozone e.g. (or some other stratospheric species), then some small effect on mass 114 would be expected since chemical reactions often do not distinguish between isotopes. This memory effect of SO_2 could only then be an explanation, if the previous uptake of SO_2 occured under some conditions where isotopically labelled calibration SO_2 was not present (e.g. during material production). Otherwise, if the uptake of SO_2 happened during our measurements, then $^{34}SO_2$ would have to show the same effect as $^{32}SO_2$ due to our online calibration.

A special process that favors uptake and thus release of only $^{32}SO_2$ and not of $^{34}SO_2$ could be another rather unlikely possibility.

A different approach is to search for another (stratospheric) species that shows interference and like the product ions of $^{32}SO_2$ occupies mass 112. This species could be connected to high O_3 or be influenced by the stratospheric ozone increase. No concrete idea concerning the composition of such an ion has emerged so far. Further laboratory experiments are needed to resolve this problem which questions our stratospheric measurements of SO_2 with the currently used method and instrument. It is planned to perform laboratory tests concerning the reliability of SO_2 measurements under stratospheric conditions. Some tests, using an ozone generator provided by the IPA, will be realized in close cooperation with the DLR in the near future. It would be interesting to be able to confirm the observed stratospheric increase of SO_2. Pre-experiments with ozone generated by an electrical discharge have been recently conducted in our group. An increase of SO_2 was verified at high levels of produced ozone, but there was no significant change in SO_2 at stratospheric ozone mixing ratios in the range of some hundred ppbv.

Not all stratospheric penetrations exhibited increased SO_2 during the past aircraft based research campaigns of our group. The most recent airborne campaign that involved the DLR *Falcon* aircraft took place in November / December 2006. The measurements were performed using our second mass spectrometer which is of the same type as the instrument employed during the spring campaign and AMMA-SOP. The flights went from Oberpfaffenhofen, Germany, towards Scandinavia. No comparable stratospheric behaviour of SO_2 was observed during this campaign, and so far the situation remains unclear.

Chapter 5

AMMA Campaign

The international project African Monsoon Multidisciplinary Analysis (AMMA) was launched in 2001 [Brahic, 2006]. Its purpose is to monitor and describe the African monsoon for a period of ten years. The multidisciplinary approach of this project includes physical and chemical aspects. It involves atmospheric convection and transport as well as oceanic, biophysical, chemical and aerosol processes. The set of tools and methods involve modeling and simulations, field campaigns, satellite remote sensing and long term data collection from land, ocean and the atmosphere [Lebel et al., 2005].

5.1 African Monsoon and Mesoscale Convective Systems

5.1.1 Issues of AMMA

The monsoon rain affects the rhythm of life in West Africa since it dictates the agricultural cycles by providing water for the arid regions of concern. It occurs during the summer of the respective hemisphere. The rainfalls give rise to flooding that causes erosion of arable land, and leads to the destruction of roads or bridges. Puddles and ponds of rainwater breed malaria-carrying mosquitoes during the warm rainy season [Giles, 2006]. The majority of the precipitation is provided by mesoscale convective systems (MCS) [Lebel et al., 2005], which will be discussed in detail in section 5.1.2. They also play an important role in the upward transport of gases and particles due to their strong convective character.

On an even larger scale the weather phenomena over West Africa, the Sahel and Sahara region affect our climate globally. The release of latent heat in deep cumulonimbus clouds in the intertropical convergence zone (ITCZ) over Africa is one of the major sources of heat for the atmosphere [Lebel et al., 2005]. The convective weather systems above the Sahel give rise to many of the hurricanes that travel across the Atlantic each year. Sahara dust also crosses the Atlantic and provides a significant amount of aerosol, causes changes in cloud properties over the ocean, and affects the radiation budget of the planet. The mineral dust influences the biological activity in the marine eco-system by offering fertilizing mineral dust to oceanic plankton [Brahic, 2006, Zeng, 2003].

A central issue of AMMA is the occurance of ongoing and severe droughts in the Sahel region since the 1970´s [Brahic, 2006, Zeng, 2003]. The continental water cycle has been profoundly affected by 30 years of rainfall deficit.

Global changes of the sea surface temperature (SST) are supposed to generally influence the monsoon activity. This relates the African monsoon to other weather phenomena such as the El Nino/Southern Oscillations (ENSO) phenomenon in the Pacific region. The SST is a measure of the heat stored in the upper ocean layers, which influences atmospheric processes significantly. The variations of the SST in the Atlantic are strongly connected to the annual cycle of the African monsoon. Anomalies in SST variations are linked to rainfall variability over West Africa. For example, low SST over the Gulf of Guinea in summer[1] help establish a direct circulation with continental rainfall. This cycle is illustrated in **figure 5.1**.

Apart from this general influence of the ocean temperature, local aspects have to be considered as reasons for weather anomalies as well. The lasting drought situation has already effected the natural vegetation, though eco-systems usually display a certain resistance to water stress. Additionally, strong population growth in West Africa causes changes in land use. Examples are overgrazing, or deforestation to win agriculturally usable areas. The reduction of natural vegetation favors erosion and the runoff of rain water [Lebel et al., 2005]. Another effect of the surface changes is an increased surface albedo and thus a reduced supply of moisture and latent heat to the atmosphere. The self-amplification of this effect becomes

---

[1] Summer on the northern hemisphere.

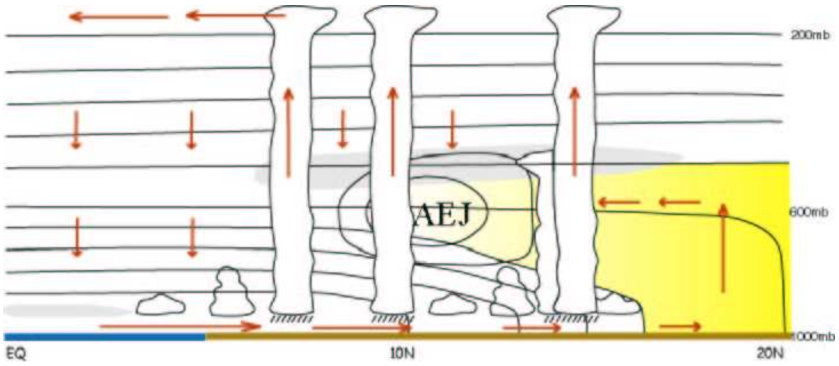

Figure 5.1: Scheme of a N-S vertical cross section along the Greenwich Meridian, looking to the west. The African Easterly Jet (AEJ) is shown in the middle. The yellow shading denotes the Saharan air layer, a dry convection layer containing Sahara dust aerosol. The AEJ participates in transporting airmasses across the Atlantic, carrying large amounts of Sahara dust westwards. [Lebel et al., 2005].

clearer in a simplified picture: the surface does not absorb as much sunlight, heats up less and convection decreases. Less evaporation of water occurs [Zeng, 2003] and fewer clouds release less precipitation, which leads to enhanced droughts. This again influences the soil moisture and vegetation, followed by a further increased albedo, and so on.

The real situation is more complex, but generally the annual rainfall is impacted by the rainfall conditions of the previous rainy season as well as by the long term drought situation. Modeling studies have shown a strong sensitivity of rainfall to land surface properties. After all, the interactions between atmosphere, biosphere and hydrosphere that determine the nature of the Monsoon are rather complicated, and weather characteristics cannot be sufficiently described by current models [Lebel et al., 2005].

Considering all these issues, the prospect of AMMA is to gain a better understanding of the African monsoon and to improve weather forecasts for the affected regions. Discussions about water resources, food security and demography in West Africa will be influenced by the results of AMMA.

5.1.2 Mesoscale Convective Systems

Clouds formed by convective instability can organize into one cloud system, a mesoscale convective system (MCS) (see **figure 5.2**), which is a large convective storm. It shows

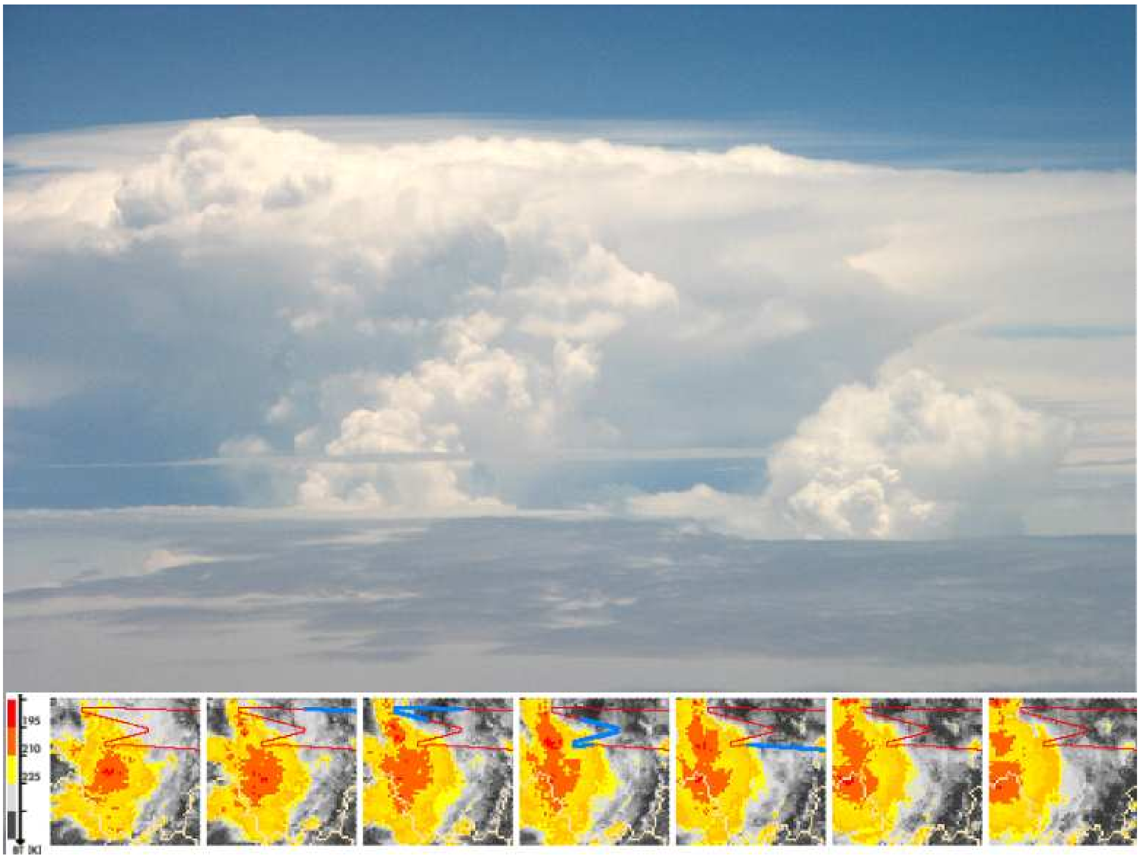

Figure 5.2: Photograph of an MCS on August 7th 2006, photograph taken by Andreas Minikin during an AMMA-SOP research flight. The satellite images of cloud top temperatures (CTT) at the bottom of the figure can be found on the AMMA website *(http://www.isac.cnr.it/∼utls/m55amma/)*. The images show the same MCS as on the photo. The colorscale denotes CTT < 225 K (yellow), < 210 K (orange), < 195 K (red). The time interval between two images is 30 minutes. The size of each satellite image covers 5° in latitude and longitude, which corresponds to 540 x 540 km. The flight track of the research aircraft is shown in red, the blue sections mark the flight section of the aircraft relative to the MCS.

mesoscale circulation with strong winds, and precipitation over wide areas. By definition of an MCS the precipitation area covers more than 100 km in at least one horizontal direction. Cloud top temperatures are typically used to represent the altitude of a cloud and may be as low as 195 K in the case of MCS, the temperature of the tropical tropopause, as **figure 5.2** implies. The cirrus ice cloud deck of an MCS at these temperatures mirrors the extemely cold tropical tropopause region. Due to strong convection an MCS may not only reach the tropopause but even cross this boundary, and inject gas, water and aerosol into the stratosphere (see section 2.2.3 for climate effects) [Houze Jr., 2004].

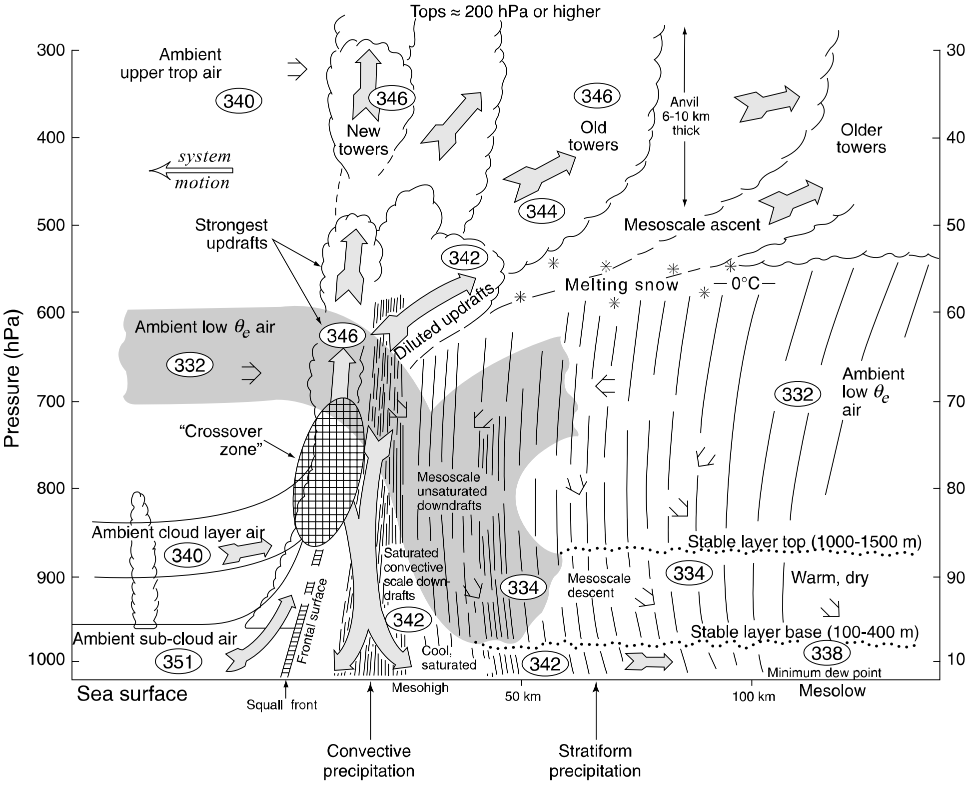

Figure 5.3: Idealized view of a tropical oceanic MCS, taken from [Houze Jr., 2004]. The system moves to the left, leaving older towers behind which form the typical anvil cloud top. Encircled values represent the potential temperature θ_e in K.

An idealized scheme of an MCS is shown in **figure 5.3**. Though this illustration shows all important characteristics of MCSs, these systems may occur in a variety of structures depending on their origin and environment.

The convective region of the MCS consists of an area of updraft, indicated by gray upward arrows in **figure 5.3**, with cumulus-scale cloud formation above the boundary layer. Intense precipitation at lower altitudes under the cloud base causes a downdraft at the rear of the MCS. The convective region shows net heating at all levels because of the release of latent heat, and its cloud top may even penetrate the stratosphere by convective overshooting.

In-cloud turbulences cause varying amounts of ambient tropospheric air to mix with the rising moist boundary layer air, decelerating and broadening its distribution. This air mass is not considered to behave as ascending parcels, like it is usually assumed for smaller scale convection, but rather to ascent via "layer lifting". A deep layer of air, up to 4.5 km strong and thus deeper than the boundary layer, is lifted along certain streamlines of conserved mass, momentum, entropy and vorticity in an unstable atmospheric environment. The updraft line is represented as a frontal surface in **figure 5.3**, showing a slope of 34°–76°.

The encircled numbers in **figure 5.3** represent the potential temperature θ_e in K in the different regions of the MCS. The potential temperature is the sum of potential and thermal energy of an air parcel, and thus is a measure for its energy content. A layering of upwards decreasing potential temperature $\partial\theta_e/\partial \mathrm{z} < 0$ is unstable and thus favors the vertical mixing of air masses [Roedel, 1994]. The displayed values of θ_e in the region of updraft indicate this unstable layering, but the rising air mass nevertheless remains a well-defined layer during its ascent. It overturns within itself as it rises, which reverses the θ_e-profile in the layer.

In response to the instability and overturning of the ascending layer, small-scale convective cells develop in the so-called crossover zone, where updrafts and downdrafts coexist (also shown in **figure 5.3** in the region of strong convection). These cells distribute precipitation particles throughout the MCS and allow a deep stratiform cloud deck to form: smaller ice particles travel upward with the ascending air and make the cloud deck thick and persistent (This so-called stratiform region of the MCS consists of deep ice clouds, extending from about 5 km to the tropopause). The crossover zone mixes the entering middle level ambient air vertically before it can pass to the rear of the system and descends due to low θ_e values, as the shaded area in **figure 5.3** indicates.

The stratiform region consists of old convection towers that stay behind as the system propagates. This region shows net heating where air moves upward and condensation occurs. Precipitation particles, snow and rain, fall out of the stratiform cloud deck and melt or evaporate, thus cooling the ambient air under the cloud base, and causing it to descend along the rear of the system. The inflow from the rear (right in **figure 5.3**) of the system, indicated by small arrows, is not only driven thermodynamically — by cooling effects of precipitation particles from the above stratiform cloud layer — but also dynamically under the influence of gravity waves that occur as a response to the mean heating in the MCS. Further explanations of gravity wave effects are given in [Houze Jr., 2004]. The precipitation falling from the stratiform region is not as intense as the strong convective rain. It covers large areas at the rear of the MCS [Houze Jr., 2004].

Lifetimes of MCS normally range from a couple of hours to about half a day, depending on their size which is effectively determined by the size of the stratiform precipitation region. The growth of the the stratiform region ceases as soon as the formation rate of new convective cells becomes smaller than the dissipation rate of the stratiform anvil. The ability to sustain a sufficient number of new cells depends on favoring environmental conditions, in particular a moist and warm boundary layer that shows potential instability. Over land this layer becomes stable at night when the surface cools down, and convection ceases.

Satellite data show that tropical cyclones spin up from MCSs. Cooling below the stratiform cloud may allow a middle level vortex to extend to the boundary layer and evolve into a deep tropical cyclone. Though the mechanisms for such effects remain unclear and further research is needed, there is little doubt that mesoscale convective vortices (MCVs) of MCSs can trigger cyclone development. It is even found that the majority of hurricanes that form over the Atlantic have their origin in weather systems over West Africa [Lebel et al., 2005].

The characteristics of the heat release to the atmosphere effect the wind field around the MCS, and determine its effects on global circulation. The altitude profile of the net heating is determined by the individual size of the stratiform region, which again is influenced by surface properties. Condensation releases latent heat at all different levels, and the stronger the stratiform part of the MCS is, the higher in altitude and stronger does the net heating maximum become.

The connection between Sahel rainfall and the frequency of Atlantic hurricanes is only one example of the global influences of large weather phenomena like MCS, and emphasizes the need to study the nature of these systems.

What happens to trace gases that enter an MCS via convection from the boundary layer?

Trace gases like SO_2 experience convective transport to higher levels with the boundary layer air. Turbulences and middle level inflow of ambient air into the convective region occur, and any gas phase SO_2 that reaches the anvil outflow region after having passed the regions of condensing water vapor will be strongly diluted.

SO_2 may enter the liquid phase of cloud droplets as soon as condensation occurs in the convective region of the MCS. These droplets may result in precipitation and remove the SO_2 from the MCS, or smaller droplets containing SO_2 may travel upward with the ascending air. The captured SO_2 is either oxidized in the liquid phase to yield sulfate, or it is released back into the gas phase at higher altitudes where droplets cool down or even freeze. SO_2 is not taken up by ice particles, so the probability of SO_2 uptake decreases as the droplets freeze in an ascending air parcle in the MCS. The release of SO_2 may also happen in the stratiform precipitation region, where droplets evaporate and lead to cooling of the rear ambient inflow.

Any SO_3 that originates from oxidation of SO_2 in the gas phase of the ascending moist air mass will certainly stick to pre-existent droplets, followed by conversion to H_2SO_4 in the liquid phase.

Transport of SO_2 in thunderstorms is hindered by cloud processes, as Wang and Crutzen [1995] show in a model calculation on the redistribution and removal of SO_2 in deep convective clouds. The results of this study confirm the suggestions that SO_2 is reduced by strong dilution and washout during the upward motion of boundary layer air: under the conditions chosen in the model 50 % of the original pollution SO_2 was captured by cloud droplets or falling precipitation. Mixing of ambient tropospheric air caused the content of boundary layer air in the anvil parts of the cloud to be as low as 10 % or less. About 80 % of SO_2 oxidation was due to H_2O_2 and most of the rest occured via metal catalysed oxidation in the liquid phase. The oxidized sulfur was removed by precipitation. Under different conditions upward transport of SO_2 may be more efficient, especially in deep convection where transport is fast (in the order of hours).

The aerosol particles that are also transported upward during strong convection act as additional CCN in the region of strong condensation and can suppress precipitation in the convective area by causing more but smaller droplets to form. Thus a larger amount of water and aerosol is transported into the upper troposphere and stratosphere. This upward transport may yield a thicker and more persistent cirrus cloud deck [Ramanathan et al., 2001].

(The previous paragraphs are mainly based on [Houze Jr., 2004].)

We can assume that deep convection and MCSs are responsible for these effects concerning trace gases, in particular SO_2:

- Strong dilution by mixing of ambient tropospheric air into the system.
- Significant loss of SO_2 due to the formation of S(+VI) in precipitation particles. These processes are particularly complex due to the low Henry constant of SO_2 and the possibility of liquid phase oxidation in droplets.
- Transport of some fraction of boundary layer pollution SO_2 to the free troposphere or even stratosphere.

5.2 Biomass Burning

The savanna and forest regions of Africa are responsible for about 20 % of global biomass burning fires [Lebel et al., 2005] and thus strongly influence the atmospheric concentrations of water vapor, particles, black carbon (soot), organic substances, and trace gases like SO_2. In West and Central Africa biomass burning aerosol emissions exceed the emissions by fossil fuel combustion three times. The fires are mainly of anthropogenic origin, e.g. to clear land for agricultural usage. The geographical region of major biomass burning shifts seasonally and matches regions of dry season. The properties of biomass burning emissions may differ with the specific local vegetation and regional agricultural practices. A wide range of water soluble species is emitted, such as organic compounds or inorganic gases and particles, which can act as additional cloud condensation nuclei (CCN). The emission of aerosol particles and trace gases occurs close to the ITCZ. Thus pollution plumes can be elevated to high altitudes by deep convection, and experience rapid transport on regional and global scales.

A fire map of central Africa shows the biomass burning activities with respect to a part of the monsoon season 2006 in West Africa (first week of August 2006) (**figure 5.4**). The fire detection is realized by a comparison of middle-infrared and longwave-infrared satellite data (comparing wavelenghts of $4\,\mu$m and $11\,\mu$m) [Giglio et al., 2003]. The effected areas in the southern hemisphere belong to the zone of tropical dry savanna and experience a dry season during the time of interest. Areas of intense agricultural use are also found in this region.

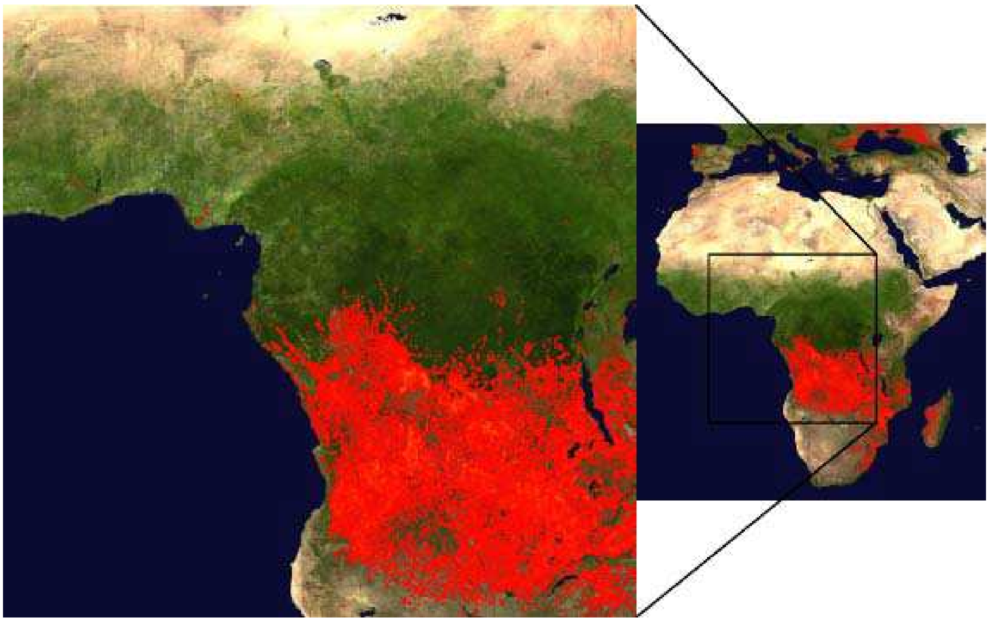

Figure 5.4: The fire map accumulates the locations of fires detected by MODIS onboard the Terra and Aqua satellites over a 10-day period from July 30th to August 8th 2006. Each colored grid cell indicates that MODIS detected at least one fire in this cell. Yellow dots denote high numbers of fires *(http://rapidfire.sci.gsfc.nasa.gov/firemaps/)* [Giglio et al., 2003].

Biomass burning emits large amounts of soot which absorbs solar and infrared radiation well. The net effect is reduced heating at the surface and increased heating in the atmosphere. Thus soot is much different from weakly absorbing but scattering aerosol such as sulfate, which primarily contributes to cooling [Penner, 2004].

Ramanathan et al. [2001] show satellite images of global aerosol optical depth and compare them to model simulations: solar radiation absorption by the surface is reduced due to soot aerosol, which leads to a cooling at the surface and a warming of the lower troposphere. This happens mainly during the dry season when biomass burning is dominant. The latitudinal gradients of solar heating that play a dominant role in driving the tropical circulation are being altered by the presence of these particles in the atmosphere.

Other products of biomass burning include different kinds of aerosol particles, water vapor, CO_2, volatile organic compounds (VOC), methane (CH_4), carbon monoxide (CO), sulfur oxides (mostly SO_2), H_2S, NO_x and ammonia (NH_3, from smoldering fires). Especially the emission of organics is strongly dominated by biomass burning [Ramanathan et al., 2001]. The listed compounds from VOC to NH_3 are reduced species that occur due to an insufficient supply of oxygen to the fire.

Ozone and OH are produced by photochemical reactions of the emitted combustion products NO_x, CO and VOCs [Jost et al., 2003, Yokelson et al., 2003], and lead to the rapid oxidation of SO_2 in the plume, followed by H_2SO_4 formation. Such oxidation products of biomass burning emissions (H_2SO_4 as well as nitric acid (HNO_3)) and their organic derivatives play an important role in aerosol formation and growth [Lebel et al., 2005].

Soot particles from biomass burning take up water vapor in regions of high relative humidity. Further uptake of the oxidation product H_2SO_4 makes these coated soot particles even more hygroscopic, and it attaches more water molecules if the humidity supply is sufficient. These droplets may take up HNO_3, the oxidation product of NO_x.

5.3 AMMA Special Observation Period, Burkina Faso

Our group participated in the AMMA campaign during the West African monsoon period from July 29th to August 19th 2006 in close collaboration with the Institute of Atmospheric Physics (IPA) at the German Aerospace Centre (Deutsches Zentrum für Luft- und Raumfahrt — DLR). Two research aircraft were deployed for airborne measurements in Burkina Faso: the DLR *Falcon* (**figure 5.6**) and the Russian M55 *Geophysica* that reaches altitudes of up to 21 km.

The scientific and technical staff of the *Falcon* and *Geophysica* was part of the AMMA Task Team 8 (TT8), which operated during the "Special Observation Period (SOP) Monsoon", the monsoon season of 2006. Our section of AMMA including the two research aircraft was located in the capital of Burkina Faso, Ouagadougou, at the military airbase "Base Aerienne 551". Our special part of the international AMMA project in Ouagadougou will in the following be referred to as **AMMA-SOP**.

Another three research aircraft were operated from Niamey, Niger. The flight activities of the five aircraft were coordinated between the flight operation centers in Ouagadougou and Niamey. Intercomparison flights ensured the comparability of the datasets.

The *Falcon* flights performed during the AMMA-SOP campaign had different objectives, which are related to the topic of the African Monsoon: long range transport (LRT) of trace gases and aerosol, and the outflow of MCSs. Typical datasets and discussions will be shown for the LRT of a biomass burning plume, and for the MCS outflow over the West African continent.

Figure 5.5: Burkina Faso in West Africa. Adjacent countries are Mali in the North, and counterclockwise Ivory Coast, Ghana, Togo, Benin and Niger. Map taken from the German Wikipedia site "Burkina Faso" *(http ://www.wikipedia.de)*

The *Falcon* flights and their prospects are listed in **table 5.1**. Not included are one testflight in Oberpfaffenhofen (Ohofen), Germany, and additional flights where the CIMS instrument did not collect data.

Date	Start	End	Purpose	Flight Route
01.08.2006	03:17	06:54	Transfer	Ohofen — Marrakesch
01.08.2006	08:19	11:34	Transfer	Marrakesch — Ouagadougou
04.08.2006	08:54	12:13	MCS outflow and LRT	over B.F. — Ghana — Atlantic coast
06.08.2006	09:24	12:39	MCS outflow	over B.F. — South Niger
07.08.2006	12:20	15:14	MCS outflow	over B.F. — South Mali
11.08.2006	14:52	17:47	MCS outflow	over B.F. — South Niger — Mali
13.08.2006	10:41	13:55	LRT	over B.F. — Ghana — Atlantic coast

Table 5.1: Overview of all flights of the AMMA-SOP campaign that include CIMS measurements. Flights started and ended in Ouagadougou except for the transfer flights. LRT = Long Range Transport. Times are in UTC.

Figure 5.6: The research aircraft Dassault *Falcon* 20 E5 during refueling at the Ouagadougou airport on August 6th 2006. Photograph taken by Andreas Minikin.

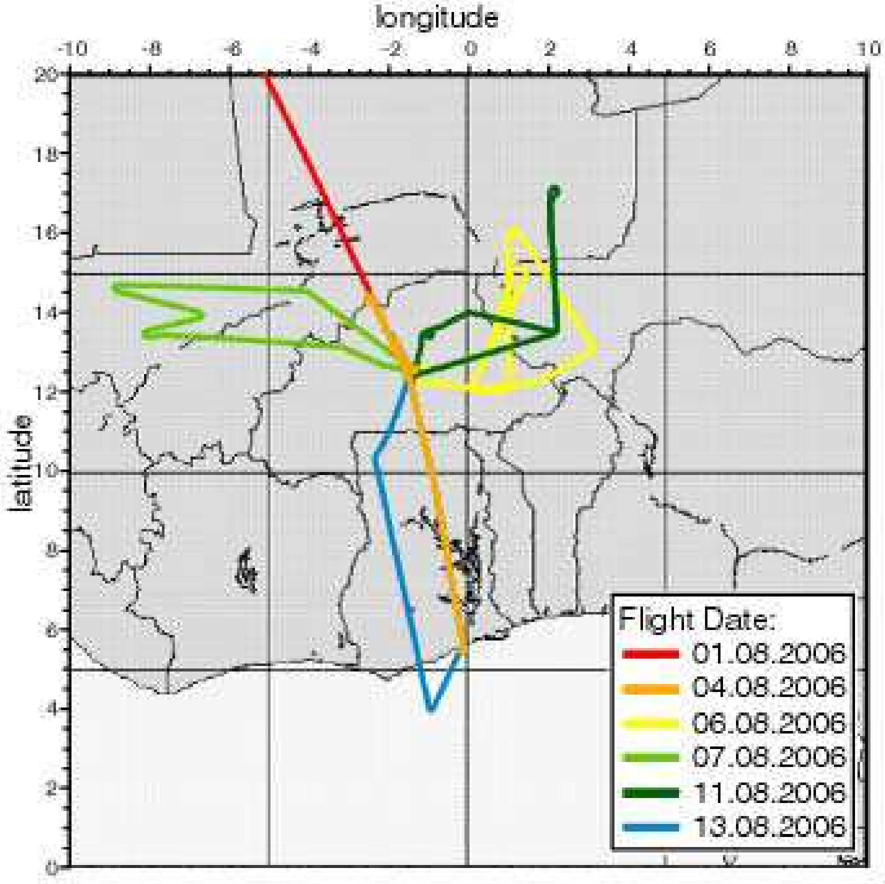

Figure 5.7: Overview for all flight tracks of the AMMA-SOP campaign.

An overview of the flight tracks during AMMA-SOP is given in **figure 5.7**. The *Falcon* payload assignment included the CIMS instrument as displayed in **figure C.1**. A photograph of the instrument inside the aircraft is found in **figure C.2**, followed by a more detailed photograph of the CIMS instrumental setup in **figure C.3**. A further description of the instrument is given in section 3.3. The complete datasets acquired by the other instruments onboard the *Falcon* were not available within the timeframe of this work. Comments on the provided preliminary data will be included.

5.4 Biomass Burning and Long Range Transport Flights

Two flights on August 4th and 13th during the AMMA-SOP campaign were concerned with LRT of atmospheric pollutants. The flights were supposed to take place when minimal MCS activity was observed. Both went south towards the coast of Ghana to performed a dive off the coast to about 4820 and 3860 m above the Gulf of Guinea and measure altitude profiles of trace gases and aerosols (see **figures 5.8** and **5.9**).

The MCS visible in **figure 5.8** was probed on August 4th during the first part of the flight before heading south. This section of MCS outflow measurement is shown as the blue part of the flight track in the satellite image. At this point only the long range transport aspect of the flight on August 4th will be discussed. MCS outflow will be the topic of section 5.5.

During the flight on August 13th the research aircraft dived into a biomass burning pollution layer that extended from about 5500 m altitude downwards. A photograph of the pollution layer (**figure 5.12**) shows the relatively sharp upper boundary of the haze as it could be seen from above. **Figure 5.11** shows the view on the coastline of Ghana from 11:50 UTC at 6.1 km altitude, above the pollution layer. The figures show that the top layer with about 68 % relative humidity obstructed the view downwards to the coastline. At about 70 % humidity the haze droplets reach diameters that favor Mie scattering ($\lambda \approx \mathrm{d}$). The visibility below the humid top layer was better due to smaller aerosol droplet diameters.

Such a pollution had not been encountered during the flight on August 4th, a cloud cover was observed instead (**figure 5.10**).

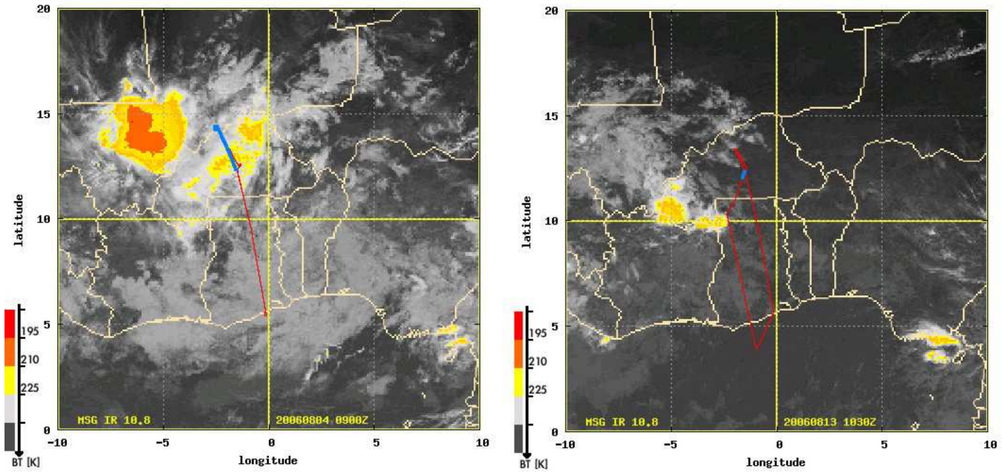

Figure 5.8: LRT flights during AMMA-SOP, satellite images of cloud top temperatures: August 4th (left), August 14th (right). The satellite images can be found on the AMMA website *(http://www.isac.cnr.it/∼utls/m55amma/)*. The colorscale denotes CTT < 225 K (yellow), < 210 K (orange), < 195 K (red). The size of each satellite image covers 20° in latitude and longitude, which corresponds to 2160 x 2160 km. The flight track of the research aircraft is shown in red, the blue sections mark the location of the aircraft during the first section of each flight.

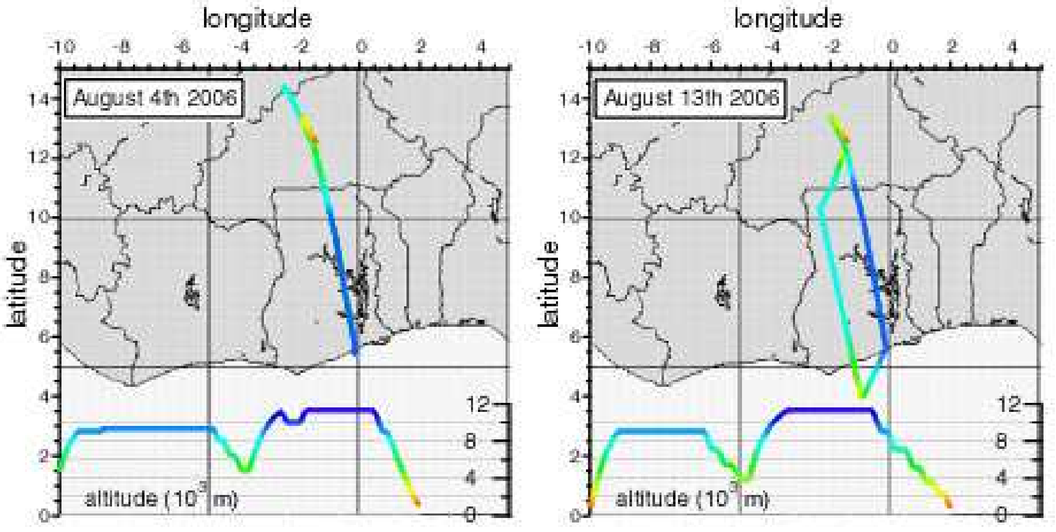

Figure 5.9: LRT flights during AMMA-SOP, geographical locations and altitude profiles. The flight track and altitude are comparable due to equal colorcoding.

Figure 5.10: Cloud cover during the research flight on August 4th 2006 around 10:45 UTC, seen from 9.1 km altitude, about 2.5 km above the clouds.

5.4.1 SO_2 Data

This section presents the data from two LRT flights of the AMMA-SOP campaign on August 4th and August 13th 2006. Research flight paths lead to the coast of Ghana (**figures 5.8 and 5.9**), where the aircraft performed a dive from 9370 m to 4820 m and from 9060 m to 3860 m, respectively, before returning to Ouagadougou. The time sequences of SO_2 and HNO_3 data are shown in **figures 5.13 and 5.14**, including a zoom into the interesting dive region of each plot.

All displayed SO_2 and HNO_3 data have been averaged over 30 seconds, corresponding to up to 660 m of travelled distance at an altitude of 10 km during level flight (220 m s^{-1}).

The biomass burning plume on August 13th covers altitudes from about 5500 m downwards to at least 3860 m. The layer characteristics of this plume are best represented in the altitude profile of **figure 5.15**. SO_2 mole fractions at the lowest flight altitudes inside the plume were as high as 1.32 ppbv, which is an increase by a factor of more than 50 compared to the average atmospheric background value of (27 ± 6) pptv. This average is taken for an

Figure 5.11: The coastline of Ghana as seen from the aircraft during the research flight on August 13th 2006 around 11:50 UTC at 6.1 km altitude.

Figure 5.12: A pollution layer off the coast of Ghana as seen from above around 11:55 UTC at 5.5 km altitude during the research flight on August 13th 2006.

altitude range above the pollution layer of 5480–9060 m during the descent, and 5410–9060 m during the ascent; the upper boundaries of the observed plume layer were 5480 m and 5410 m for this flight. Equivalent layers of the plume are generally found at slightly lower altitudes for the ascent, but the layering still exhibits a very similar structure. The horizontal distance between ascent and descent was about 80 km.

- A top layer with rapidly increasing SO_2 of averaged 7.2 pptv SO_2 per 10 m is observed during 408 m of the descent (5480–5070 m) (red in **figure 5.17**). The mole fraction of SO_2 at 5070 m altitude is 322 pptv. The equivalent layer during the ascent is 690 m strong (5430–4740 m) with an averaged downward increase of 5.3 pptv per 10 m, and 398 pptv SO_2 at 4740 m altitude.

- This is followed by a 540 m deep layer of almost constant SO_2 values of 322–384 pptv. This layer was found from 5070 m downwards during the descent (only 1.2 pptv increase per 10 m) (yellow in **figure 5.17**). It is less extended during the re-ascent (320 m from 4740 m downwards) and shows an average increase of 0.5 pptv per 10 m (389–416 pptv).

- An intermediate layer (green in **figure 5.17**) shows downward increase rates of 5.2 pptv SO_2 per 10 m for 350 m during the descent, and 2.5 pptv per 10 m for 360 m during the ascent.

- The lowest and most heavily polluted layer of this plume is found from 4190 m (descent) or 4070 m (ascent) down to the lowest point of the dive at 3860 m with the highest observed SO_2 value of 1323 pptv. The descent yields a downward increase of SO_2 of 22.8 pptv per 10 m while the ascent increase rate is 28.4 pptv per 10 m (blue in **figure 5.17**).

HNO_3 values show a similar layering profile during the descent on August 13th, with a maximum value of 3.96 ppbv at the lowest point of the dive. The re-ascending HNO_3 leg does not follow the SO_2 layering due to a memory effects.

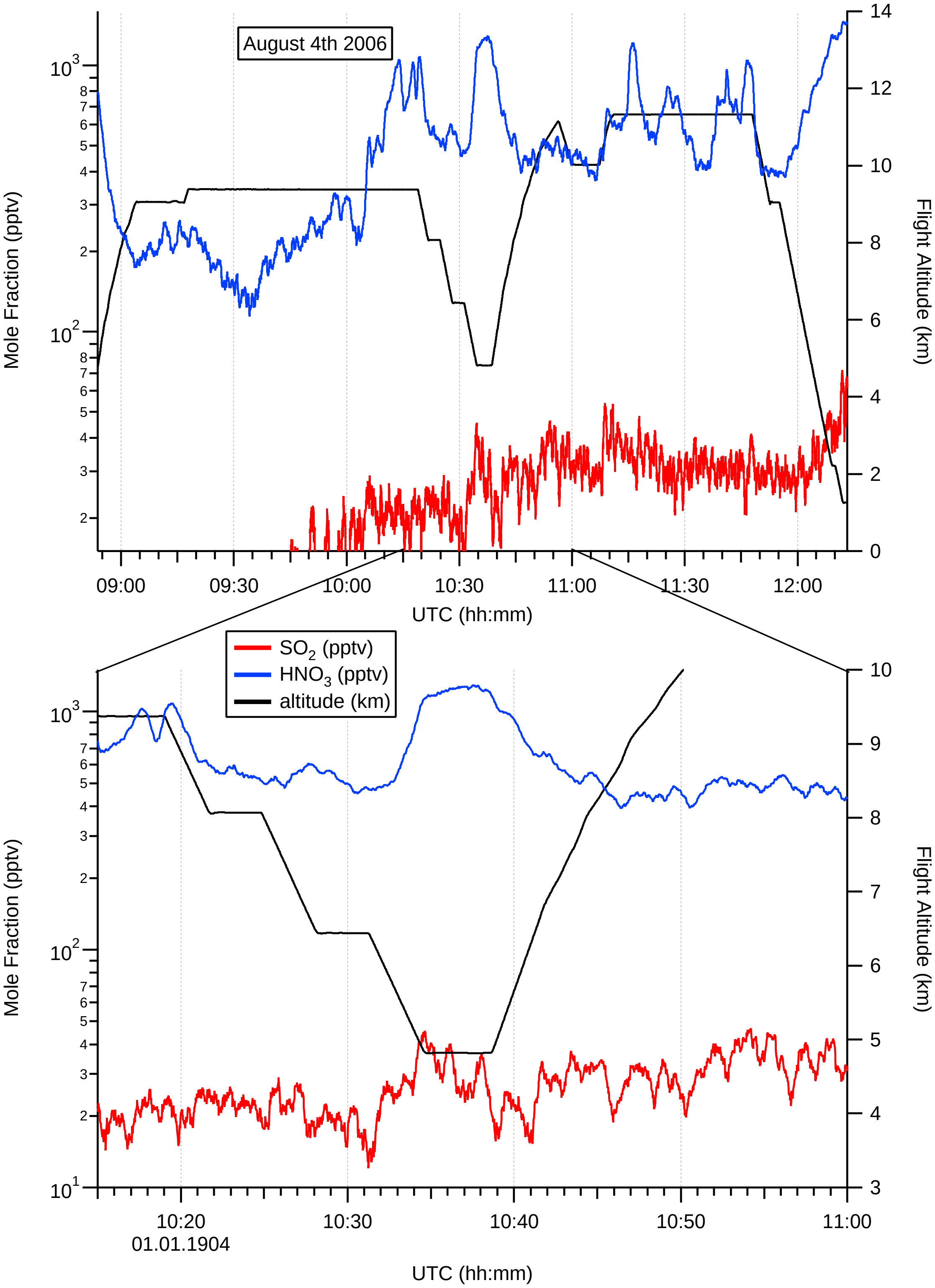

Figure 5.13: Time sequences of SO_2 and HNO_3 mole fractions measured by CIMS for the long range transport flight on August 4th, including the flight altitude.

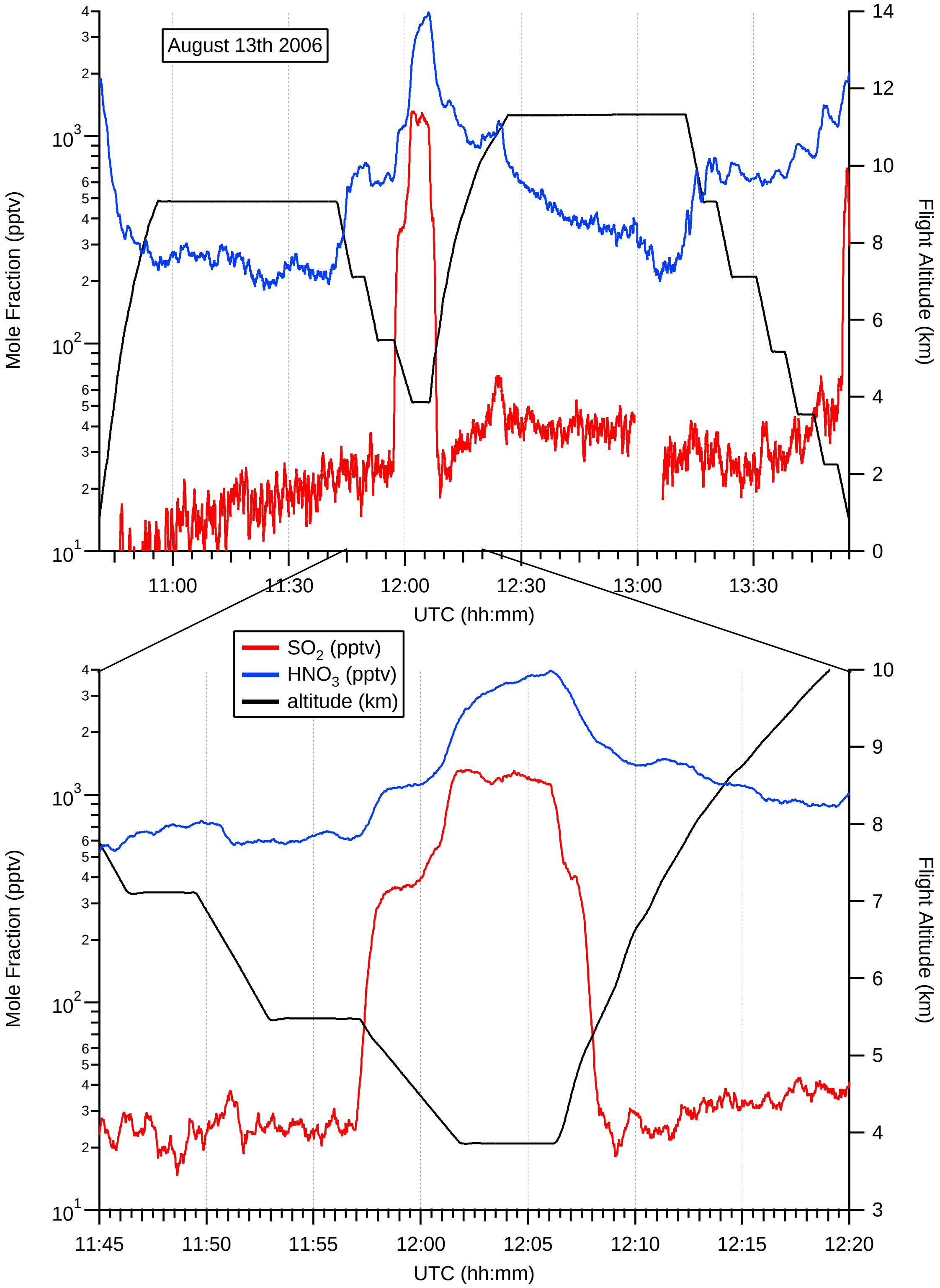

Figure 5.14: Time sequences of SO$_2$ and HNO$_3$ mole fractions measured by CIMS for the long range transport flight on August 13th, including the flight altitude.

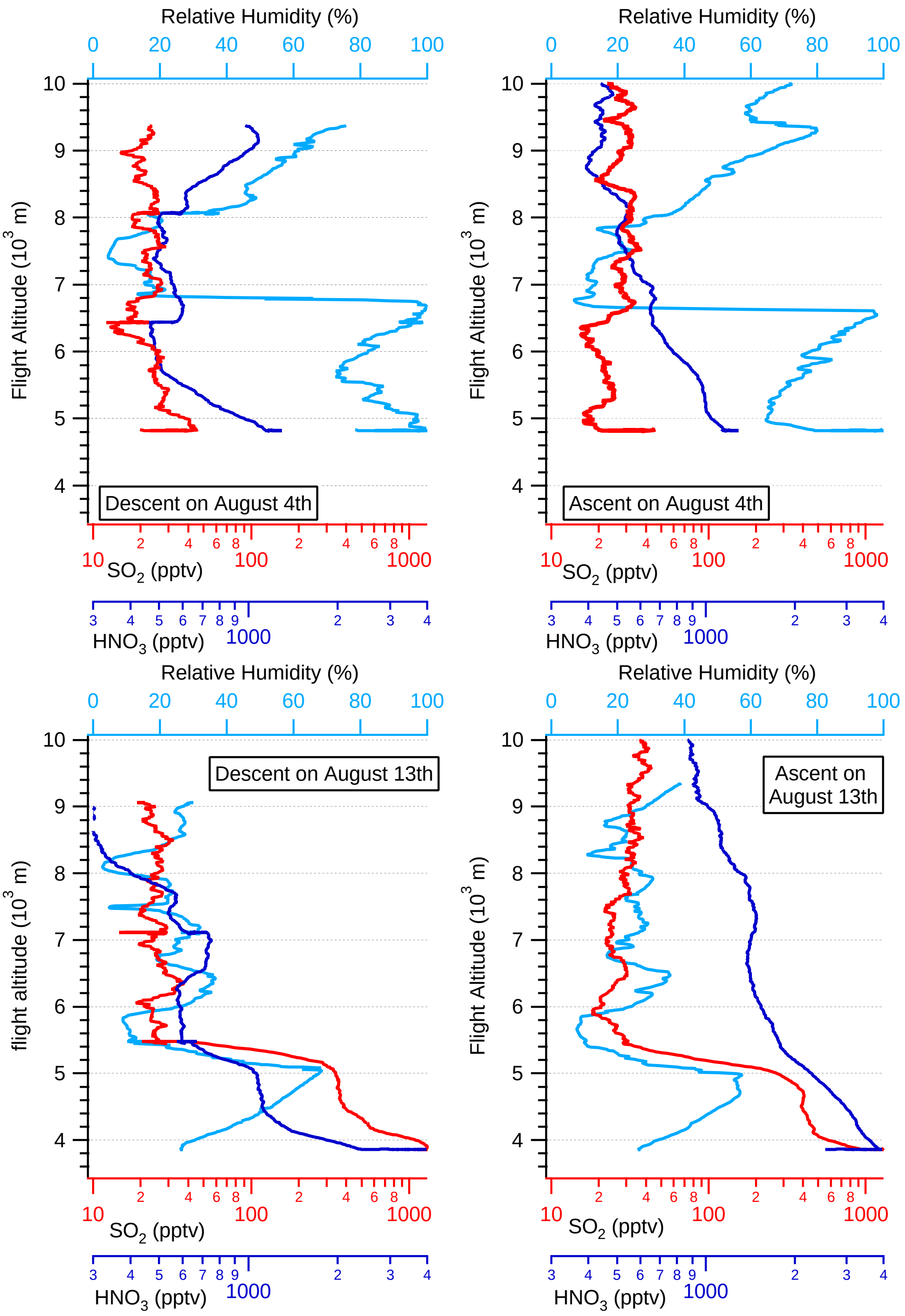

Figure 5.15: Biomass burning plume: altitude profiles for SO_2, HNO_3 mole fractions and relative humidity (from aircraft basic data). The plots show the dives and climbs before the Ghana coast for the flights on August 4th and 13th.

During the flight on August 4th we did not encounter an SO_2 pollution comparable to August 13th. The altitude profiles in **figure 5.15** instead show a general decrease of SO_2 from the altitude of highest relativ humidity (around 6600 m). A minimum in SO_2 mole fractions is found at 6430 m during the descent (12 pptv) and at 6250 m during the ascent (16 pptv). A layer of higher SO_2 mole fractions follows from below 6210 m during the descent, and below 5990 m during the ascent, showing a peak value of only 25–30 pptv around 5420 m, followed by a further decrease down to 15 pptv towards the surface (lowest altitude at 4820 m).

Only during the descent do we observe another layer of increased SO_2 from 5730 m down to the lowest point with a maximum SO_2 value of 45 pptv, which is still only a moderate pollution. This layer is not observed during the re-ascent when we must have left this plume.

HNO_3 values increase towards the surface, and reach as high values as during August 13th at corresponding altitudes (1.29 ppbv maximum value at the lowest point). HNO_3 does not follow the SO_2 layer structure mentioned before.

Figure 5.16 shows an example of how mass spectra of polluted plume air looked like. It is deduced from the flight on August 13th. The features around masses 112 amu and 123–124 amu stand out and account for strong SO_2 and HNO_3 pollution. The strong peak at mass 124 amu could be an additional product ion of HNO_3 from the reaction with HCO_3^-. The maximum measured mole fraction of about 4 ppbv inside the pollution plume on August 13th would be further increased if the contribution of this educt ion was included. However, it has not been included since the origin of mass 124 amu and the ion molecule reactions have not been investigated yet.

The calibration SO_2 peak at mass 114 amu is not different inside and outside the pollution plume region. It is mainly due to the injected calibration gas. The peak at mass 112 amu instead is strongly increased inside the plume. It accounts for ambient SO_2. The features around mass 75–80 amu are an indicator for humidity [Speidel, 2005] and show that the averaged plume spectrum is not very humid compared to the background spectrum.

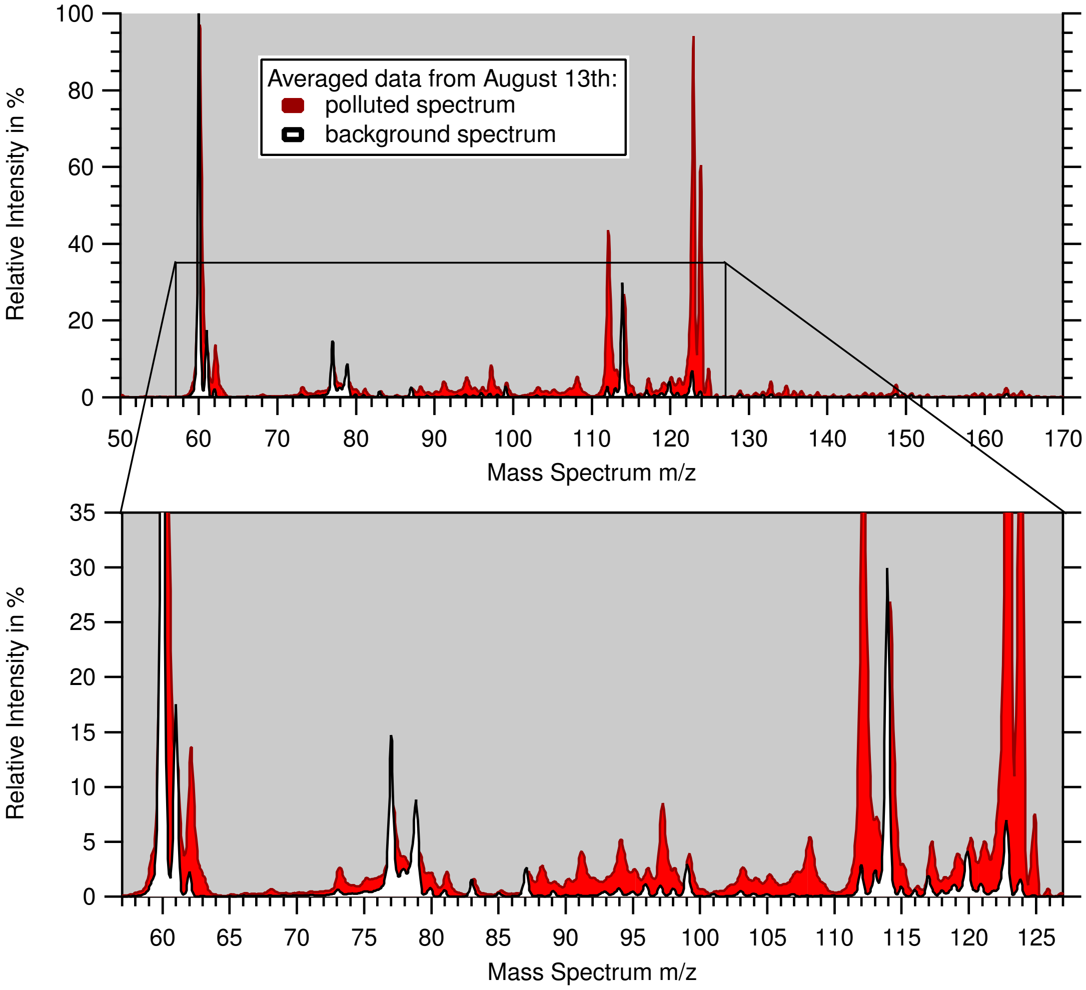

Figure 5.16: Averaged spectra for the biomass burning plume from August 13th, normalized to the highest peak. The red spectrum is an average over about 5 minutes inside the plume in the lowest part of the dive from about 3860–4150 m. The background spectrum is averaged over 10 minutes (from 11:22–11:32 UTC) at 9060 m outside the plume and displayed for comparison.

5.4.2 Interpretation and Discussion

The general increase of SO_2 inside the pollution plume on August 13th of up to 1.3 ppbv exhibits a layering structure which is found during both, the descent and re-ascent of the altitude profile. HNO_3 shows the same layer characteristics during the descent. It exhibits a peak mole fraction of 3.96 pptv towards the end of the dive at 3860 m and shows a strong

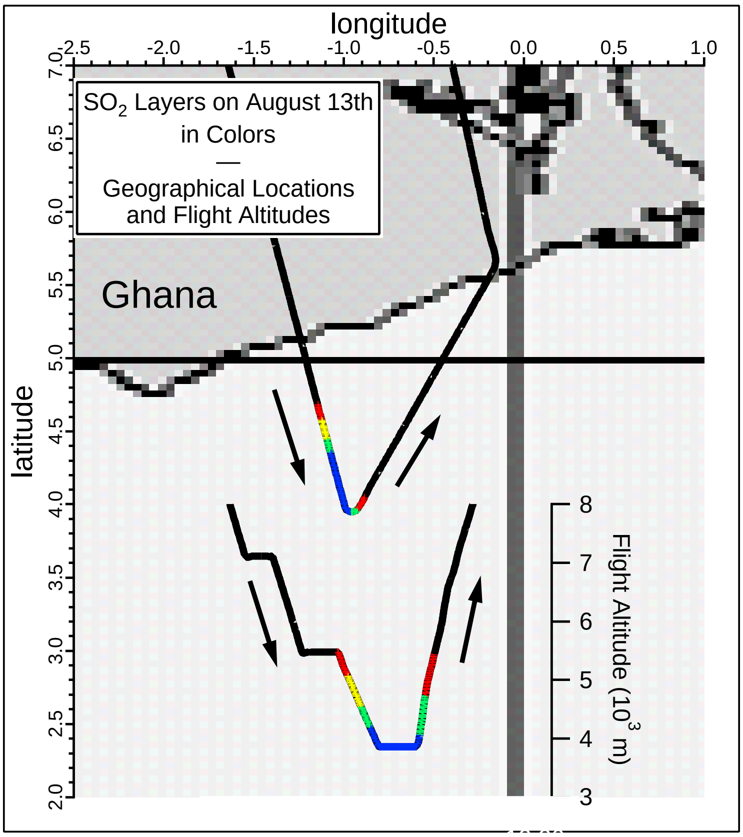

Figure 5.17: SO_2 layering during the dive and re-ascent on August 13th. SO_2 generally increases towards the surface during the whole flight. red) rapidly increasing SO_2 in a layer of strongly increasing relative humidity. yellow) layer of almost constant SO_2, while the relative humidity decreases towards the surface. green) increasing SO_2. blue) rapidly increasing SO_2 down the lowest flight level.

memory effect during the ascent. At such high concentrations HNO_3 sticks to the interior walls of the instrument and slowly evaporates again after the concentration decreases, resulting in a shift of the profile´s structures while the memory effect lasts. The general features observed in SO_2 during the ascent of the dive are still to a certain degree visible in HNO_3, but they seem to occur about 1 min later, which corresponds to an altitude difference of about 700 m during the ascent (see expanded region of the time sequence in **figure 5.14**). The memory effect increases the measured HNO_3 mole fraction while the ambient mole fraction has already decreased. The time sequence implies that the memory effect after a pollution event of ≈ 4 ppbv HNO_3 could even last for an hour – from about 12:10–13:00 UTC during

August 13th. The measured HNO_3 values during the re-ascent after such a strong pollution are thus quantitatively not reliable.

Similar to the trace gas SO_2 the relative humidity (from *Falcon* basic data aquisition) rapidly increases with lower altitudes during the flight on August 13th: from 12 % at 5480 m (descent) and 8 % at 5660 m (ascent) to a sharp maximum of 68% at an altitude of 5080 m (descent) and 58% at 4980 m (ascent). This corresponds to the first layer of SO_2 as described in section 5.4.1. Only this layer can be found in both the relative humidity and SO_2. The relative humidity does not follow the SO_2 layer structure further downwards, but decreases almost linearly towards the surface with a rate of 0.4 % per 10 m during the descent and the re-ascent. The layering of SO_2 during the altitude profile on August 13th is visualized in **figure 5.17**. The colorcoding is deduced from the layer description in section 5.4.1. It can be seen that the layering is of the same structure during the descent and ascent, but located at slightly lower altitudes during the ascent further off the coast.

The preliminary data for CO from the DLR-IPA display mole fractions of up to 480 ppbv that clearly indicate combustion as the source of pollution. The altitude profile of CO is of a similar shape as our measured HNO_3 profile, even showing the structure that was previously identified as HNO_3 memory effect. Further discussions, involving the final CO data, should cast some light on the nature of this memory effect, or reveal a real pollution structure of CO and HNO_3 in this biomass burning plume. The preliminary NO and NO_y data (also from the DLR-IPA) do not show this shape. A strong pollution of about 8 ppbv NO_y at the lowest point of the flight is present. NO mole fractions are only at 3 % of the measured NO_y mole fractions, indicating aged pollution.

HYSPLIT 4 day back trajectories can be found in **figures C.9 to ??**. They illuminate the origins of the air masses that we encountered during the dive and re-ascent. The starting points of the trajectories correspond to the layering in **figure 5.17**, with each trajectory starting at the top of a layer:

- C.9a) The red layer is characterized by strongly increasing SO_2 mole fractions and relative humidity (during the descent). The hysplit trajectory refers to an altitude of 5478 m at the top of this layer. The layer extends down to 5070 m during this flight section.

- C.9b) The red layer layer (during the ascent) extends up to an altitude of 5429 m, which is chosen as the endpoint altitude of this trajectory. The layer extends down to 4736 m during this flight section.

Both trajectories come from the coast of Cameroon, but the air encountered during the descent (a) has travelled at altitudes above 5 km for four days, while the trajectory during the ascent (b) rises from below 3 km in northern Cameroon. Both travelled across the ocean above 5 km altitude and are thus likely to carry dry air.

- C.9c) The top of the yellow layer of almost constant SO_2 (during the descent) is located at 5070 m.

- C.9d) The top of the yellow layer (during the ascent) is found at 4736 m altitude. This layer is less extended during the ascent and not visible in **figure 5.17**.

Both trajectories come from the area of Northwest Cameroon, but their travelling altitudes differ: trajectory (d) experiences a strong lifting to 5 km just before the air mass leaves the continent.

- **??**e) The trajectory endpoint is at the top of the green layer (during the descent) at 4534 m. The SO_2 mole fractions are increasing below the layer of almost constant SO_2 (yellow).

- **??**f) The trajectory endpoint is at the top of the green layer (during the ascent) at 4410 m.

Altitude profiles as well as geographical history are similar for these two trajectories. The air experiences a lifting of almost 1000 m before leaving the continent (as in (d)).

- **??**g) The trajectory endpoint is at the top of the blue layer (during the descent) at 4188 m. SO_2 mole fractions show a rapid increase at least down to the lowest flight altitude of about 3860 m.

- **??**h) The trajectory endpoint is at the top of the blue layer (during the ascent) at 4068 m.

- **??**i) The trajectory endpoint is at the lowest level just after the descent at 3864 m.

- **??**k) The trajectory endpoint is at the lowest level just before the ascent at 3857 m.

These air masses come from below 3000 m and south of the equator. Unfortunately HYSPLIT does not support equator–crossing since the trajectories are calculated from different datasets for each hemisphere. The trajectories probably originate from regions of strong biomass burning in the southeast. This would explain the intense pollution. Generally (for this flight) the lower air masses originate from locations further south and thus from closer to the major fire locations, carrying more biomass burning pollution.

Trajectories for altitudes above the pollution layer (some examples are shown in **figure ??** for altitudes of 7 km (a), 6.5 km (b) and 6 km (c)) generally originate from further north, where far less fires are observed. According to HYSPLIT they have not travelled below 5 km for at least 3 days and thus experienced strong photochemistry in these altitudes before we observed them.

A sharp transition (red in **figure 5.17**) as we encountered it on August 13th between the clean and dry free troposphere and a biomass burning pollution layer has been observed before by [Yokelson et al., 2003]. Within this transition layer of some hundred meters they observed a strong increase of H_2O. The relative humidity from August 13th shows this feature as well. We can assume that the layering was very stable, and only little mixing with clean overlying air occured. Such mixing is also more likely to occur over land and by strong convection, which can perturb the stable layering of the plume, while we encountered the layer above the Gulf of Guinea.

An equivalent self-stabilizing effect of haze layers can generally be observed in inversion weather, when fog or haze create a cooling effect towards the surface and stabilize the layering.

Why does the altitude profile on August 4th not show such an SO_2 pollution layer? The dive extends almost as far down as that on August 13th, but the observed SO_2 mole fractions, especially during the ascent, are even lower than those in the free troposphere (about 20–30 pptv above 7 km altitude, see the alitude profile in **figure 5.15**).

The HNO_3 mole fractions increase towards the surface and reach 1.29 ppbv at 4820 m. They are comparable to the measured HNO_3 mole fractions of 1.09 ppbv at the same altitudes on August 13th.

The cloud cover and the corresponding step from 10 % to 100 % relative humidity on August 4th are the main difference compared to the LRT flight on August 13th. SO_2 and HNO_3 have been taken up by cloud droplets, which is indicated by a slight decrease in mole fractions at the altitudes of highest relative humidity in **figure 5.15**. While HNO_3 starts to increases towards the surface from about 1 km below the cloud cover (which indicates some aged pollution), the SO_2 mole fraction stays low. The pollution must have experienced additional cloud processes and removal of SO_2 before HNO_3 was formed by oxidation of pollution NO_x.

SO_2 shows a layering structure, which is described in section 5.4.1 and displayed in **figure 5.18**. The red section during the descent marks a layer of low SO_2 (compared to the free troposphere) down to 12 pptv, which is below the detection limit of 17.2 pptv SO_2. The yellow section shows an intermediate layer of increased SO_2 below 6210 m. A further increase (up to 45 pptv) follows only during the descent (green). The aircraft left this slightly polluted green layer and encountered a clean region (clean referring to SO_2) at the lowest flight altitude of 4820 m. It ascended into another layer of increased SO_2 (yellow) that extended up to 5590 m. The yellow layer occured at similar altitudes during the descent and ascent and displayed comparable SO_2 mole fractions of about 25–30 pptv. Higher HNO_3 values during the ascent may be due to memory effects and do not neccessarily imply that the air masses had different sources. Equivalent yellow and red layers are found at lower altitudes further off the coast, as already observed in **figure 5.17** during August 13th.

The preliminary CO data confirm that there had been a pollution plume in SO_2. The slight increase in SO_2 mole fractions that is visible in **figure 5.13** during the lowest flight section shows some structure which is also found in the CO data. CO as a long lived tracer still exhibits pollution mole fractions of up to 260 ppbv. Unlike during August 13th it does not mirror the structure or memory effect of HNO_3 as nicely. Preliminary NO_y data again range at about twice the measured HNO_3 mole fraction at the lowest flight altitude, where

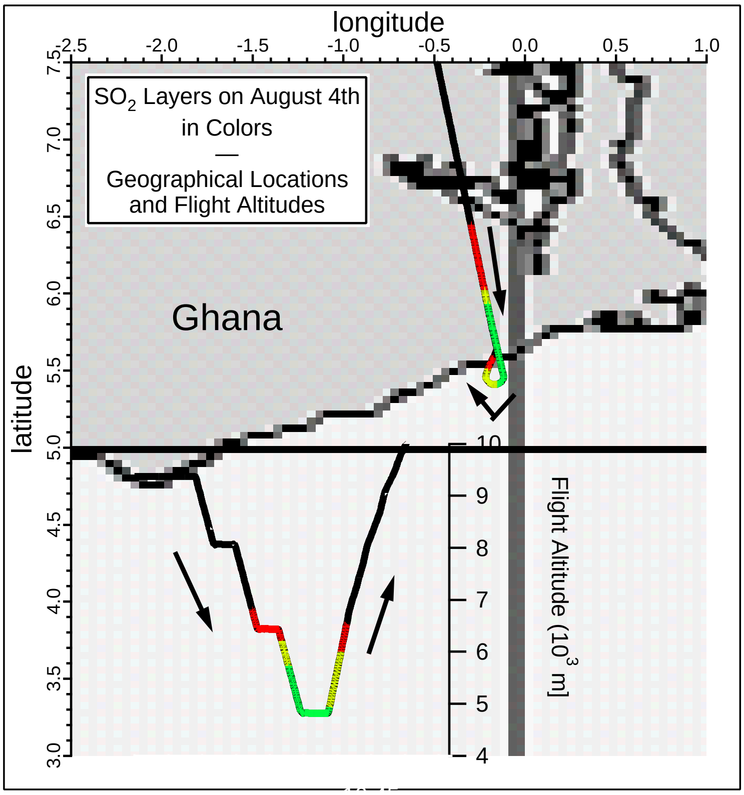

Figure 5.18: SO_2 layering during the dive on August 4th. red) layer of decreased SO_2 while the relative humidity peaks at about 100 %. yellow) intermediate layer of enhanced SO_2 values, followed by a decrease towards the surface. green) layer of increased SO_2 values, only observed during the descent. Unlike in figure 5.17 the colors do not refer to layers of different increase rates of SO_2, but denote layers of slighly higher or lower SO_2 mole fractions.

the pollution is strongest. NO mole fractions are only of the order of 5 % of the measured NO_y mole fractions, indicating aged pollution below the cloud cover.

The origins of the air masses during August 4th are illustrated in HYSPLIT 4 day back trajectories in **figures C.4 and C.5**. The trajectory altitudes and locations were chosen to be at SO_2 maximum or minimum values inside the red, yellow and green layer. The layering differs from that observed on August 13th, and similar colors for layers do not imply similar layer properties or characteristics:

- C.4a) The trajectory endpoint is chosen inside the red layer with decreased SO_2 and very high relative humidity of 100 % (during the descent) at the SO_2 minimum at 6430 m altitude.
- C.4b) The trajectory endpoint is at the SO_2 minimum at 6250 m inside the red layer (during the ascent).

Much different than during August 13th, both trajectories approach the measurement position from the continental north. They show very similar paths and altitudes, which supports their common origin. Both air masses were lifted from about 3 km over eastern Nigeria.

- C.4c) The yellow layer shows slightly increased SO_2 (during the descent). The trajectory endpoint is a the SO_2 local maximum at 5420 m.
- C.4d) The yellow layer (during the ascent) has a local SO_2 maximum at 5490 m altitude.

The ascent trajectory (d) shows that this weakly polluted air mass had been below 3 km only two days earlier, and has not travelled far since. The SO_2 pollution layer originates from the area of southern Ghana, Togo or Benin. Plot (c) during the descent shows a trajectory very similar to (b), only about 1 km lower.

- C.5e) The green layer shows increased SO_2 (only during the descent) with a maximum at 4530 m.
- C.5f) After leaving the green layer (just before the ascent) there is a minimum of SO_2 mole fractions at 4410 m altitude.

The trajectory plots give no indication of why the descent shows increased SO_2 while the ascent is much cleaner at the same altitudes. Both trajectories originate from the ocean and perform a short turn over land before arriving from the north. The high SO_2 and relative humidity that we measured around (see **figure 5.15**) may thus be due to a single and probably local pollution source which HYSPLIT does not show.

The trajectories of the lowest altitudes do not indicate that the air masses originated from specifically polluted areas, especially not from the biomass burning regions of Central Africa. The sources of the encountered pollution cannot be identified as as easily for August 4th as for August 13th.

Still, the Emission Database for Global Atmsopheric Research (EDGAR) give some hints concerning the origins of biomass burning pollution in the area of the Gulf of Guinea (see **figure 5.19**) [Olivier and Berdowski, 2001]. Yokelson et al. [2003] observed biomass burning pollution from humid savanna regions as a well-mixed layer of haze up to altitudes of 6 km, while we encountered a similar layer on August 13th around 5.5 km. It is not clear whether the air beneath the cloud cover on August 4th could be identified as haze as well. The HYSPLIT trajectory calculations in **figures C.4 to ??** imply that pollution from the region of Central Africa contributed to our plume, at least on August 13th. **Figure 5.19** shows some possible sources of SO_2 pollution for this region:

Residential biomass burning (**figure 5.19a**) is dominant in the area of Ghana. This is especially interesting concerning the slight SO_2 pollution measured during August 4th, which probably originated from this region according to the HYSPLIT trajectories (**figure C.4d**).

Biomass burning SO_2 from deforestation (**figure 5.19b**) has strong sources at the African West coast between the equator and 15° S. These emissions underlie annual cycles and are most dominant during the dry season that this region experienced during the time frame of the AMMA-SOP campaign. Deforestation fires north of the equator did not occur during this time of the rainy season (for seasonal fires compare EDGAR with the firemap **figure 5.4**).

Another highly seasonal emission source are savanna fires (**figure5.19c**) as mentioned before and suggested by [Yokelson et al., 2003]. These fires were again most likely to occur south of the equator during the time of AMMA-SOP. Savanna and deforestation fires are the most plausible source of the SO_2 and soot pollution that we measured and observed during August 13th.

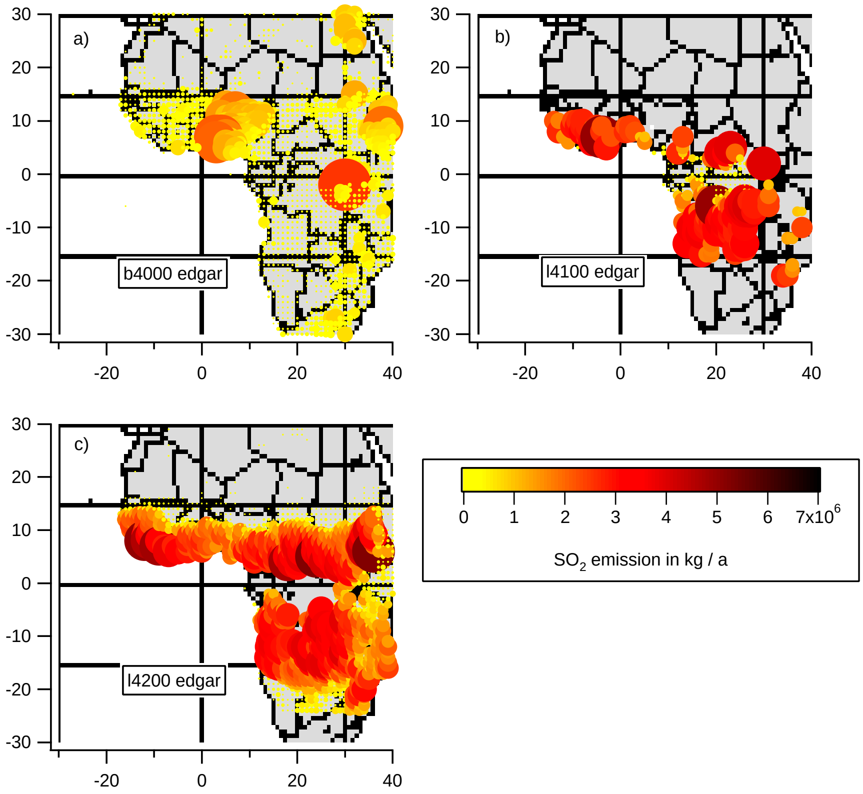

Figure 5.19: Global emission data for SO_2 from the EDGAR database, based on the year 2000. The colorcoding refers to the SO_2 emissions in kg SO_2 per year. a) residential BB emissions. b) deforestation. c) savanna fires [Olivier and Berdowski, 2001].

- BB emissions of residential origin (b4000 → a)
- BB emissions from deforestation (l4100 → b)
- BB emissions from savanna fires (l4200 → c)

5.5 Mesoscale Convective System Flights

The flight times and routes for MCS outflow flights were planned on the basis of meteorological predictions and forward trajectory calculations for the MCSs of interest. Nighttime and early morning meetings of the Ouagadougou operation team, and tele-conferences with the operation centre in Niamey were the backbone for flight planning, while the ongoing observation of the evolving convective systems helped to decide about the actual flight route and time. The idea was to sample air that had been processed by an MCS during the previous 24–48 hours. The research aircraft *Falcon* was supposed to probe air from altitudes of 12–13 km, its maximum flight altitude. See **figure 5.20** for the four flight routes relative to the convective systems that were probed during the AMMA-SOP campaign.

MCSs are characterized by strong convection and contribute to convective transport of trace gases and aerosol to the upper troposphere. The nature and structure of these systems as well as the fate of the trace gases that are transported by an MCS have been discussed in section 5.1.2.

5.5.1 SO_2 Data

This section presents the data from four MCS outflow flights during the AMMA-SOP campaign on August 4th, 6th, 7th and 11th 2006. The measurements were performed in the outflow (east) of the MCS, and during one flight (August 6th) in the region of a dissipating MCS. An overview of the SO_2 and HNO_3 data is given in **figures 5.21 and 5.22**, displaying the temporal evolution of the trace gas mole fractions separately, and the altitude profiles of all MCS flights in one plot. It has to be discussed which data points can be used for MCS outflow analysis.

A general systematic increase of SO_2 is observable during all AMMA-SOP research flights and will be adressed in the discussions section.

The HNO_3 mole fractions do not show a similar systematic increase as it is observable in the SO_2 time sequences. The mole fractions range from 100 pptv to 1 ppbv and show a slight decrease with altitude during August 6th and 7th. The highest parts of these flights were in the outflow of MCSs which already implies that HNO_3 may generally decrease in the outflow regions.

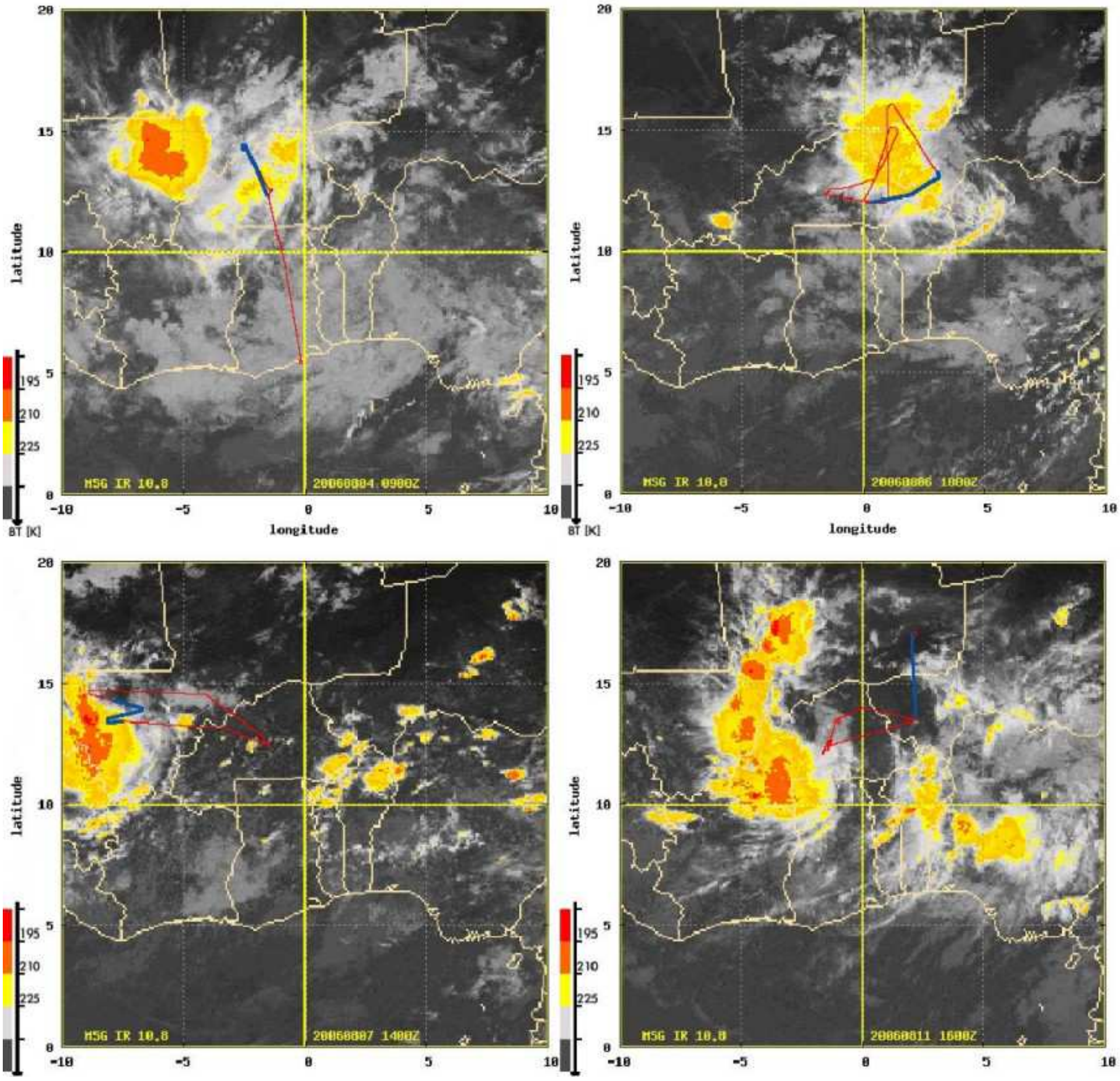

Figure 5.20: MCS flights during AMMA-SOP, satellite images of cloud top temperatures: August 4th (top left), August 6th (top right), August 7th (bottom left), August 11th (bottom right). The satellite images can be found on the AMMA website *(http://www.isac.cnr.it/∼utls/m55amma/)*. The colorscale denotes CTT < 225 K (yellow), < 210 K (orange), < 195 K (red). The size of each satellite image covers 20° in latitude and longitude, which corresponds to 2160 x 2160 km. The flight track of the research aircraft is shown in red, the blue sections mark the first half hour after takeoff for each flight. The further evolution of the MCSs during the flight can be seen in figure C.10.

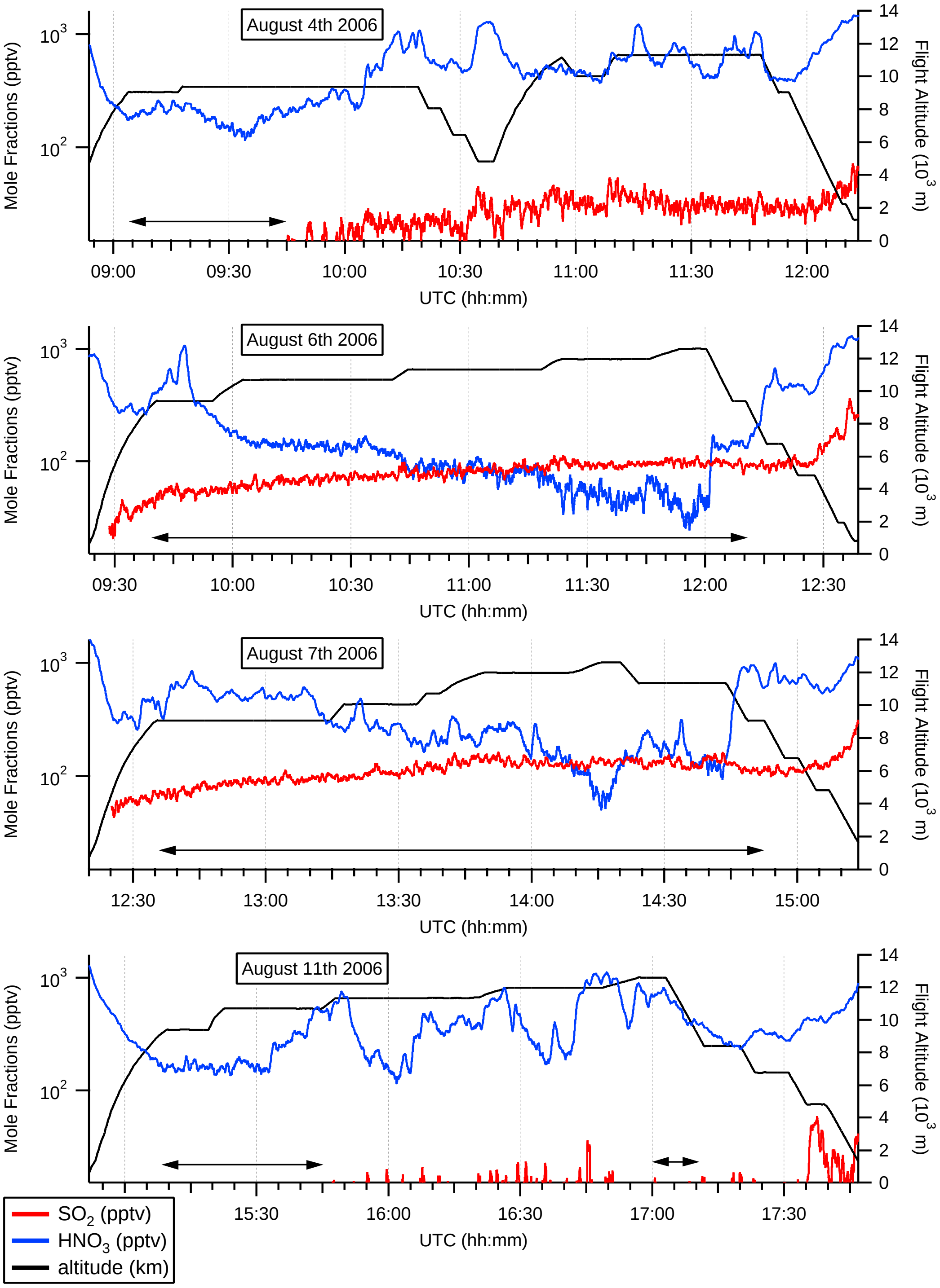

Figure 5.21: Time sequences of SO_2 and HNO_3 mole fractions measured by CIMS for the four MCS outflow flights, including the flight altitudes. SO_2 data points below 15 pptv are cut off according to the SO_2 detection limit: SO_2 mole fractions significantly below the detection limit (17.2 pptv) are subject to the variability of the measurement background. The arrows denote the MCS outflow regions as described in section 5.5.2 with flight altitudes for MCS outflow of ≥ 9 km.

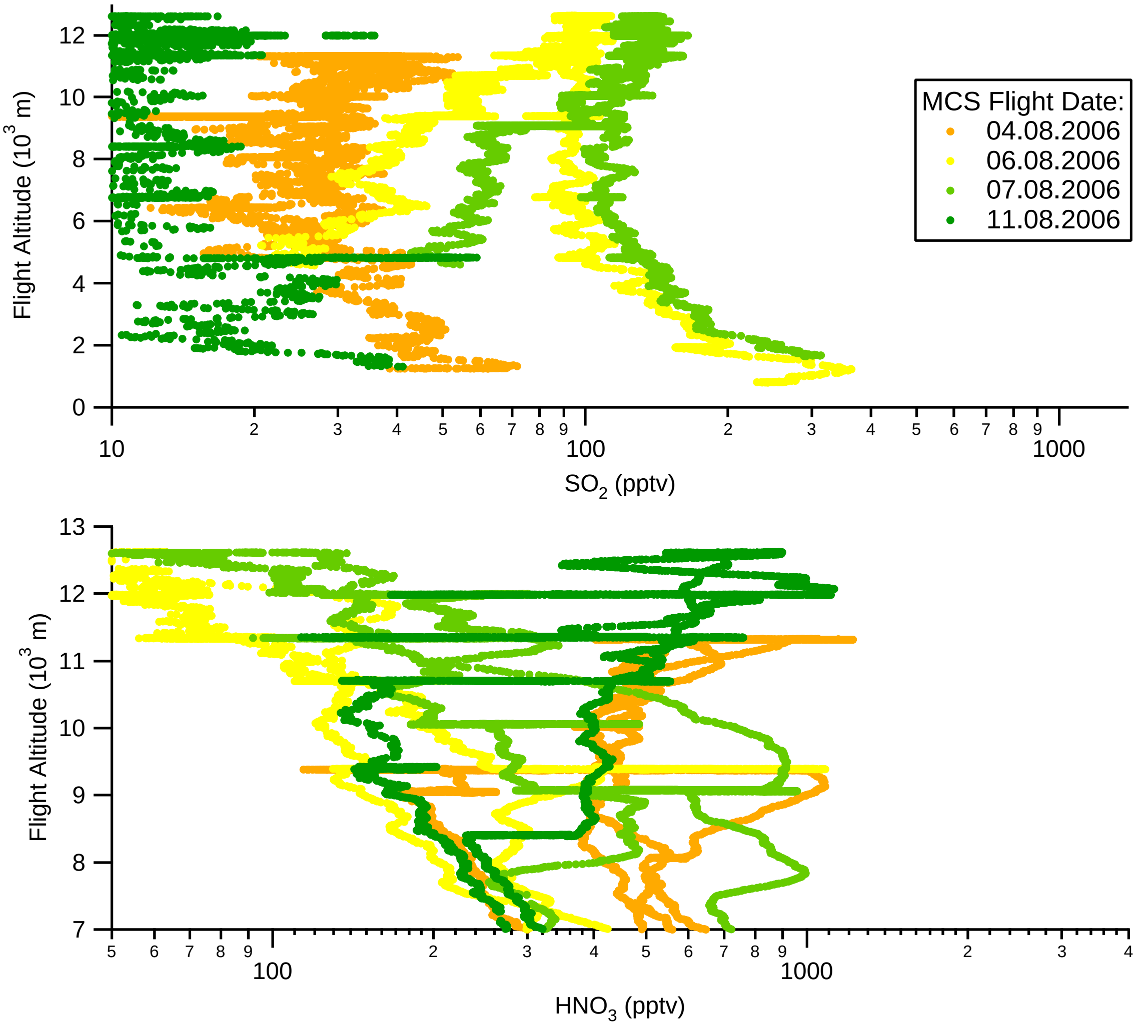

Figure 5.22: Overview of SO_2 and HNO_3 altitude profiles for the four MCS outflow flights during the AMMA-SOP campaign. The SO_2 systematic increase is especially observable during August 6th and 7th.

5.5.2 Interpretation and Discussion

The systematic increase in SO_2 mole fractions could be due to a memory effect on the interior walls of the inlet system. The boundary layer air at the airport, where the *Falcon* was stationed, was humid and polluted by SO_2 and other trace gases, while our inlet system at the top of the aircraft was constantly open to the ambient air. A thin water layer could have formed in the inlet line, taking up pollution from the boundary layer air. Ambient SO_2 that was probably stored in this layer would be released during research flights, while dry and clean air flushes the inlet line at higher altitudes. A release of this ambient SO_2 (memory effect) would result in an artificially high measured SO_2 mole fraction during the flight, starting after the aircraft´s takeoff and slowly wearing off, when SO_2 in the water film starts to decrease due to evaporation. The opposite of the observed increase would be expected of such a memory effect.

The systematic increase is not only visible in the SO_2 mole fractions, but already in $^{112}(SO_5^-)$ counting rates. Other mass lines do not show this behaviour during the research flights. Calculating the SO_2 mole fractions by using the elementary ACIMS formula leads to an equivalent systematic increase. One difference should be mentioned though: the strong increase of calculated SO_2 mole fractions before landing (for each flight) is due to a decrease of the calibration gas (and educt ion) counting rate and not observed according to ACIMS.

Measured SO_2 mole fractions for the AMMA-SOP flights do not vary much during each flight (observe the almost uniform behaviour of SO_2 in **figure 5.21**). A comparison of the average mole fractions of the flights shows that the measured SO_2 ranges from 111 pptv on August 7th to 8 pptv on August 11th, which is well below the detection limit of 17.2 pptv ($2\,\sigma$ of the instrumental background). Again, looking at the counting rates of mass 112 amu for each flight shows that the tendency for very low or high SO_2 values originates in this mass line.

The measured mole fractions of SO_2 are all assumed to be real for the following discussion to allow the intercomparison between different flights at all. The reason for the observed behaviour of SO_2 mole fractions (and counting rates) is not clear.

Not all data points taken during the flights on August 4th, 6th, 7th and 11th are equally suitable for MCS outflow analysis. Some parts of the flights show long distances between the aircraft and the MCS. This is obviously the case for August 4th, when an MCS was probed during the first part of the flight, while a long range transport section followed and lead the aircraft away from the dissipating MCS.

There are also some parts of the flights, especially during August 4th and 11th, where SO_2 is below the detection limit of 17.2 pptv.

- The flight on August 4th probed an MCS only during the first section of the flight which went north after leaving Ouagadougou. The MCS part of this flight includes measurements up to 09:45 UTC when the aircraft was already about 600 km southeast of the center of the MCS. The shortest distance to the center of the MCS was about 340 km at an alititude of 8.5 km at 09:15 UTC. It can be seen in **figure 5.21** that the SO_2 data points for this flight up to about 09:45 UTC are well below the detection limit of 17.2 pptv. Thus most of the data points cannot be used for MCS outflow analysis.

- The entire dataset of the flight on August 6th can be used for an MCS outflow analysis. The system that was probed during this flight dissipated just northeast of Ouagadougou. The entire dissipation process of this system can be seen in the second row of satellite images in **figure C.10**. The research aircraft circled the system in counterclockwise direction until it was just north of the center. It crossed the center of the MCS three times, first going straight south (11.3 km altitude), then north (12.0 km) and back southwest (dive from 12.6 km until landing) while flying back to Ouagadougou.

- **Figure 5.2** shows a photograph of the MCS from August 7th. At 12:45 UTC the research aircraft was already in a distance of about 540 km from the MCS center, approaching further. The aircraft went west at 10.1 km altitude until it was north of the MCS´s center in only 250 km distance. It probed the outflow region east of the system (see bottom left image of **figure 5.20**) at altitudes of 10.1–12.6 km and headed back to Ouagadougou at 12 km alitude. The distance between the aircraft and the MCS exceeded 600 km at about 14:50 UTC.

- The MCS visible on the bottom right image of **figure 5.20** or in the bottom row of **figure C.10** does not show the round or elliptical shape of the MCSs observed during the other flights, but exhibits a line-structure with a biggest cell in the south and some smaller cells north of it. A number of MCS must have combined to give rise to this shape that is visible in the cloud top temperature images. The research aircraft had a distance to this MCS structure of about 340 km at an altitude of 9.4 km before it headed east and away from the system. It reached a distance of about 600 km at 10.7 km altitude around 15:45 UTC (data points until 15:45 UTC are mainly below 10 pptv – see **figure 5.21**), ascended further and turned north, keeping a distance of about 600 km to the MCS line. The aircraft approached the system again and reduced the distance to less than 600 km from about 17:00 UTC on.

For the further analysis only data points within a distance of 600 km between the aircraft and the system are used for MCS outflow discussion. This distance is six times the minimum horizontal dimension of an MCS (per definition [Houze Jr., 2004]) and about twice the average diameter of the cirrus cloud decks as visible on the satellite images in **figure 5.20** (~ 340 km diameter for cloud top temperature below 225 K).

This leaves the following flight sections: 08:55–09:45 UTC on August 4th, while most of the measured SO_2 is below the detection limit. The whole flight on August 6th can be used for MCS analysis. On August 7th data points from 12:30–14:50 UTC are MCS outflow data. The flight sections before 15:45 UTC and after 17:00 UTC on August 11th were at 600 km or less distance to the MCS and will be further discussed. These flight sections are marked by arrows in **figure 5.21** with the additional limitation that the flight altitude was ≥ 9 km.

Figure 5.23 shows altitude profiles of the MCS outflow data. Compare this figure to the altitude profile displaying the complete flights (**figure 5.22**). Most of the SO_2 data points from August 4th and 11th are below the detection limit which is indicated by a grey dotted line in the upper plot. These data points cannot be used for MCS outflow analysis. It is unclear why so little SO_2 was measured during these flights. The bottom plot in **figure 5.23** shows only data from August 6th and 7th in comparison to measured background SO_2 in the

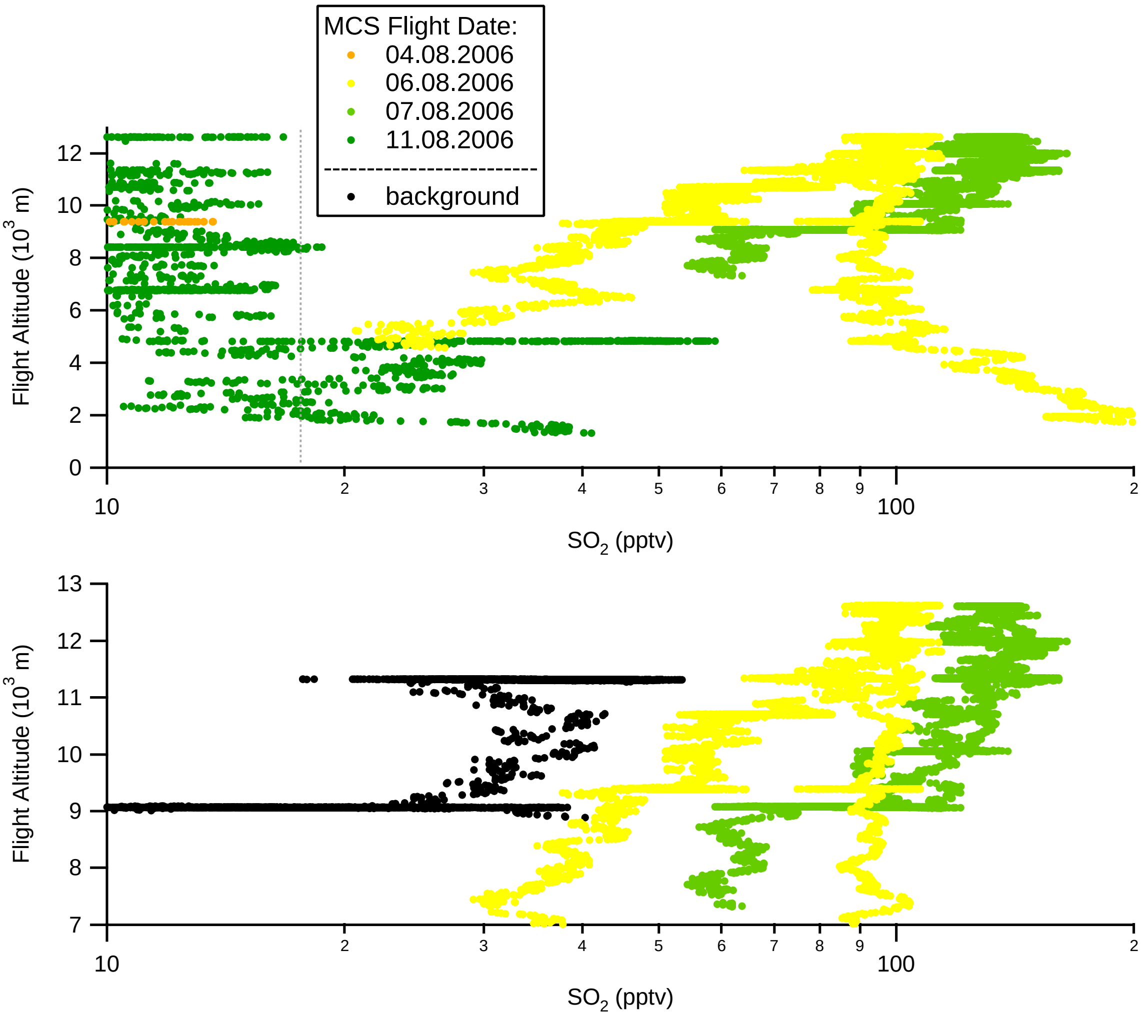

Figure 5.23: Overview of SO$_2$ altitude profiles for two MCS outflow flights during the AMMA-SOP campaign, including only the MCS outflow parts of the flights as discussed in the text. The detection limit (17.2 pptv) for SO$_2$ is indicated by the grey line in the upper plot. A background SO$_2$ altitude profile is applied to the bottom plot for comparison. The background values are taken from August 13th during flight sections in the free troposphere.

free troposphere. The background data are taken from the flight on August 13th at altitudes of 9.1–12.0 km (significantly above the pollution plume that was encountered later during this flight at $\leq$ 5.5 km altitude) and at a horizontal distance of at least 130 km to location where the plume was encountered by the aircraft. Very little convective clouds were observed during this day (see right plot of **figure 5.8**).

The average measured SO_2 for the background and the two MCS flights are (from 9.1 km upwards): 27 pptv ($\sigma = 12$ pptv) for the background on August 13th, 78 pptv ($\sigma = 16$ pptv) for the MCS flight on August 6th and 111 pptv ($\sigma = 23$ pptv) for the MCS flight on August 7th. If the background measurements are representative for free troposperic SO_2 that is not influenced by convection, then the vertical transport of SO_2 in the MCSs that we probed was significant and the resulting SO_2 increase in the range of 50–90 pptv.

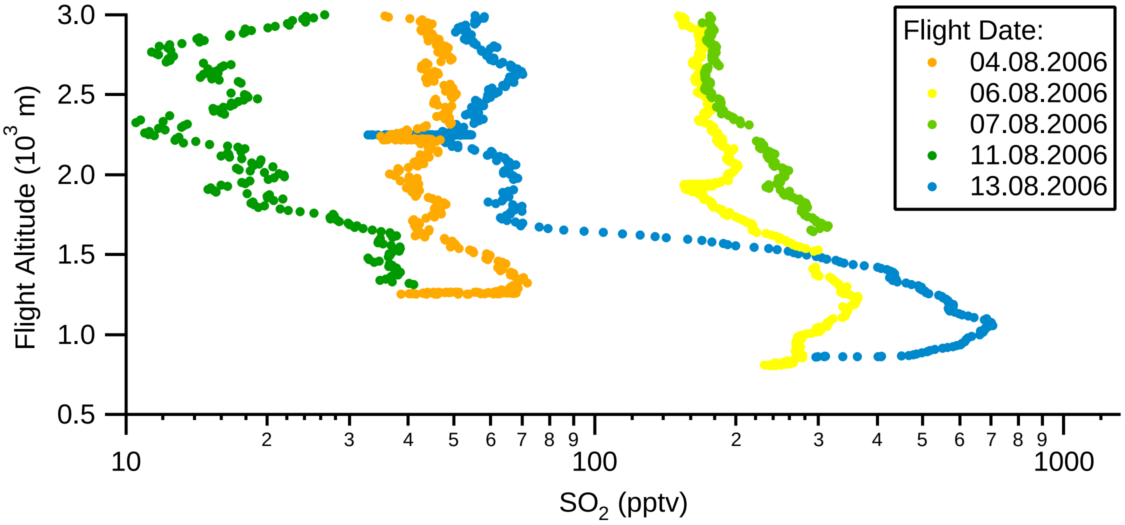

Figure 5.24: Overview of SO_2 altitude profiles for the boundary layer below 3 km during the AMMA-SOP campaign. The measurements in these altitudes result from takeoff and landing of the research aircraft at the Ouagadougou airport.

There are very few SO_2 measurements in the planetary boundary layer that all result from takeoff and landing at the Ouagadougou airport. An overview of SO_2 below 3 km altitude is given in **figure 5.24**. The highest mole fractions of 705 pptv were measured at 1050 m on August 13th before landing in Ouagadougou. Further approaches for landings on August 6th and 7th show 325–365 pptv SO_2. These data are taken in the well mixed boundary layer above the city of Ouagadougou, which is dominated by traffic exhaust from mopeds and burning of waste. Mole fractions of SO_2 in rural areas are probably lower and include a smaller contribution from traffic emissions.

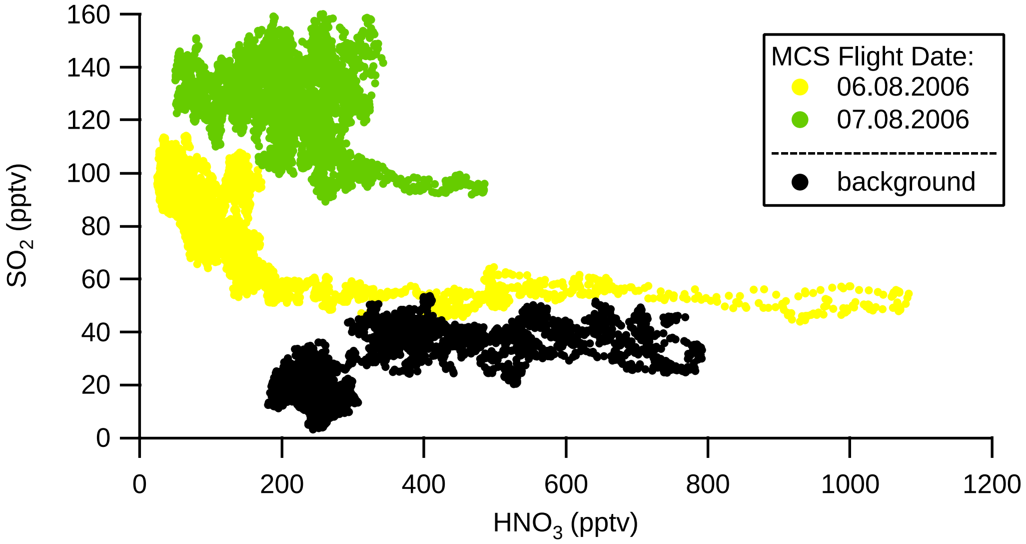

Figure 5.25: Scatterplot of SO_2 vs HNO_3 mole fractions for the MCS outflow data. It shows the different effect of convective cloud processing on the two trace gases: vertical transport of SO_2 to the free troposphere, and removal of HNO_3 by cloud processes. The tails of data points towards higher HNO_3 values for August 6th and 7th generally contain the points of lowest altitudes in this plot (just above 9 km).

Wang and Crutzen [1995] show in their model calculation on the redistribution and removal of SO_2 in deep convective clouds that SO_2 experiences strong dilution and washout while it is lifted from the boundary layer. The model estimates that 50 % of the original SO_2 pollution are captured by cloud droplets or falling precipitation under the chosen environmental conditions. Mixing of ambient tropospheric air caused the content of boundary layer air in the anvil parts of the cloud to be as low as 10 % or less. If we apply these results to our boundary layer SO_2 measurements (with the highest measured SO_2 value of 705 pptv on August 13th, see **figure 5.24**) an increase of the free tropospheric SO_2 by 35 pptv (50 % of the elevated 70.5 pptv) due to convective cloud transport would be expected. Our MCS outflow SO_2 measurements of 51 pptv and 84 pptv above a background of 27 pptv imply that the increase is probably twice as high, depending on the boundary layer conditions and the characteristics of the vertical transport in the specific MCS, which are not provided.

Thus vertical transport of SO_2 in convective cloud systems may be more efficient in our case than estimated by [Wang and Crutzen, 1995].

The fate of HNO_3 in convective clouds is the strong uptake of HNO_3 by cloud droplets and thus a removal from the gas phase. **Figure 5.25** illustrates that this contrasts the SO_2 increase in the free troposphere due to convective transport. While SO_2 increases in the outflow region to three times the background value of about 40 pptv, HNO_3 decreases due to washout. The highest SO_2 datapoints coincide with HNO_3 values that are generally lower than in the free troposphere background. The uptake of HNO_3, a strong acid with large Henry constant, in cloud droplets is much more efficient than that of SO_2. Also, if ammonia is present, HNO_3 is not released significantly by droplets that evaporate in the outflow anvil, but it experiences deposition as nitrate in aerosol.

The NO_x that experiences convective transport to the outflow region of an MCS cannot be oxidized to HNO_3 on the time scale of the transport process. It takes 1–2 days for NO_x to form HNO_3, while the convective transport can be of the order of hours.

Chapter 6

Summary and Conclusions

Measurements of sulfur dioxide (SO_2) have been carried out in the free troposphere during this work. A Chemical Ionization Mass Spectrometry (CIMS) instrument equipped with a quadrupole ion trap mass spectrometer was deployed onboard the research aircraft *Falcon*, which is operated by the German Aerospace Center (Deutsches Zentrum für Luft- und Raumfahrt — DLR) in Oberpfaffenhofen, Germany. During two research campaigns the CIMS method and an online isotopic calibration were used to detect sulfur dioxide. Gaseous nitric acid (HNO_3) was also measured by our group.

6.1 Spring 2006 campaign

The *Falcon* research aircraft was operated from the DLR airport in Oberpfaffenhofen during the spring 2006 campaign. Two flights on March 24th and 25th were concerned with hemispherical long range transport of atmospheric pollution.

We probed a pollution plume from Southeast Asia that had been predicted by the FLEXible PARTicle dispersion model (FLEXPART) and intercepted by the research aircraft on both flight days. It was identified by its enhanced carbon monoxide (CO) content. This was possible due to the long lifetime of the CO tracer of more than a month. SO_2 mole fractions in the predicted plume regions were not significantly high: about 30–40 pptv were measured in the free troposphere during the entire flights, while the detection limit was at 10.3 pptv. The SO_2 mole fractions exhibited features that showed similarities with ozone at various points during the plume penetration. Ozone and CO had been measured by the DLR Institute for Physics of the Atmosphere (IPA). The similarities lead to the conclusion that the two trace gases originated from the same air mass of Asian pollution.

HYSPLIT (HYbrid Single-Particle Lagrangian Integrated Trajectory) air mass trajectories and FLEXPART simulations indicate that the plume had been traveling for about 7 days from its source region in Souteast Asia and China before it reached Europe. EDGAR (Emission Database for Global Atmsopheric Research) emission data could identify China as a major emission source of fossil fuel combustion SO_2, while wood- and savanna-fires in Southeast Asia contributed biomass burning SO_2 pollution. India is also a strong source of residential and industrial biomass burning emissions. The air masses passed over Asia at altitudes of about 5 km and entrained polluted air from the named sources at these low altitudes, then it travelled the Pacific and Atlantic ocean at altitudes of 7–10 km before it reached Europe. The measured SO_2 mole fractions were not significantly increased inside predicted plume regions. Gasphase or cloud-related oxidation processes in the atmosphere had already reduced SO_2 mole fractions to its background value of 30–40 pptv during this time period.

Other sections of the flights, especially of the research flight on March 25th, showed similarities in SO_2 and ozone while CO mole fractions were low. The air masses that were encountered during these flight sections over Southern Europe had experienced mixing of stratospheric and tropospheric air. The mixing had been induced by a low pressure trough that was present over Central Europe as the plume arrived in this area. We could identify these stratospheric air layers at altitudes of 7–9 km by low CO, but increased ozone, SO_2, and HNO_3 mole fractions, inside and out of the predicted plume region. This mixing is typical for Central European weather and indicates that pollution from high altitudes may reach lower tropospheric layers or even the continental boundary layer. Surface trace gas concentrations (e.g. ozone) may be increased due to pollution plumes that were subject to long range transport. Stratospheric trace gas and aerosol concentrations may also be increased over Europe, since the mixing of stratospheric air into the troposphere implies the opposite effect of tropospheric air in the stratosphere.

SO_2 mole fractions were not significantly increased in the plume regions, which implies that the SO_2 pollution that originated from biomass burning and fossil fuel combustion over Asia had already contributed to H_2SO_4 formation (and thus aerosol formation and growth) before reaching Europe. The plume had traveled the northern hemisphere at altitudes of 7–10 km. The background concentration of aerosol in the entire northern hemisphere is thus influenced by emissions from certain polluting areas, e.g. the industrial regions of Eastern Asia.

Increased H_2SO_4 formation in the free troposphere favors new particle formation and growth of particles. Grown aerosol particles increase the planetary albedo and change the the radiation budget of the planet. When aerosol particles act as cloud condensation nuclei they can induce the formation of clouds in the free troposphere. Clouds cool the planet by scattering incoming sunlight back to space,but they also contribute to greenhouse warming. The overall effect strongly depends on cloud properties like the droplet size and number distribution, which is effectively altered by the presence of pollution aerosol and sulfuric acid.

6.2 AMMA campaign

Our group participated in the African Monsoon Multidisciplinary Analysis (AMMA) campaign during the Special Operation Period (SOP) Monsoon in August 2006. This part of the international AMMA campaign was located at the airport of Ouagadougou, Burkina Faso, in West Africa. Two major issues of the campaign were addressed in this thesis: the long range transport of biomass burning pollution and the convective transport of trace gases in Mesoscale Convective Systems (MCS) during the monsoon season. The main motivations for investigating the African monsoon are the ongoing draughts in the Sahel region, and the improvement of climate models and weather forecasts on regional and global scales. The specific role of SO_2 and H_2SO_4 includes the influence on cloud properties due to aerosol formation and droplet growth, and the changes of the planetary radiation budget by sulfate aerosol.

On August 4th and 13th we investigated long range transport of atmospheric pollution. A dive and re-ascent were performed off the coast of Ghana during each flight to measure altitude profiles of the trace gas and aerosol distribution. We encountered a sharp transition between the free troposphere and a layer of high relative humidity (70 % on August 13th; 100 % and cloud cover on August 4th) below about 6 km altitude.

The underlying air on August 4th was characterized by high relative humidity of 70–100 %, while SO_2 mole fractions were similar or below the free tropospheric SO_2 values of about 20–30 pptv. The detection limit for SO_2 during the AMMA campaign was at 17.2 pptv. The tropospheric background HNO_3 mole fraction was about 500 pptv during this flight. The mole fractions of HNO_3 decreases by about 100 pptv below the humid cloud layer, then increased towards the surface and reached a maximum value of 1.29 ppbv at the lowest point (4.8 km altitude). HNO_3 pollution was observed, but SO_2 had been removed from this plume layer. This indicates that the air mass may have experienced cloud processes shortly after its pollution occured, while HNO_3 had not yet been produced from NO_x at that stage (the time range for $NO_x \rightarrow HNO_3$ is 1–2 days). The uptake of HNO_3 in cloud droplets is observable in the decrease of mole fractions right below the transition from dry to very humid air where clouds were present. HNO_3 pollution at lower altitudes was not affected by these processes.

During the flight on August 13th we encountered a strong layer of SO_2 and HNO_3 pollution below the transition step in humidity. SO_2 and HNO_3 mole fractions and the relative humidity showed a simultaneous strong increase. The mole fraction of SO_2 reached 1.32 ppbv at the lowest point of the flight (3.8 km altitude) while tropospheric SO_2 mole fractions of 30–40 pptv were measured above the humid layer. HNO_3 mole fractions reached a peak value of 3.96 ppbv at the lowest flight level, compared to a tropospheric background of about 500 pptv. HNO_3 displayed a significant memory effect during the ascent, which indicates that the measured HNO_3 mole fractions after strong pollution events are quantitatively not reliable for probably up to an hour. The observed pollution in SO_2 and HNO_3 was significant and extended down to at least 3.8 km altitude during this flight. HYSPLIT back trajectory calculations imply that plume air from this lowest section of the flight came from the African continent south of the equator and from below 3 km altitude. The pollution was about 4 days old when it reached the measurement site. EDGAR emission data show a strong source of biomass burning in this region, which is due to deforestation fires and savanna burning induced by a dry season.

Four flights of the AMMA campaign were concerned with the outflow of MCS, which are large thunderstorms that contribute most of the monsoon rainfall. The flights took place on August 4th (the first part of this flight before probing polluted air), August 6th, 7th and 11th. Our measurements of SO_2 imply that this trace gas experiences vertical transport in convective clouds. Only two of four MCS flights (6th and 7th of August) show the expected enhanced SO_2 mole fractions in outflow regions at altitudes of ≥ 9 km. The two other flights exhibit very low SO_2 mole fractions, often below the detection limit, and cannot verify upward transport.

One general problem of SO_2 measurements during AMMA becomes important when we discuss small increases of SO_2 (of the order of tens of pptv) that are due to convective transport: The mole fractions of SO_2 do not show much variation during each AMMA flight (except for the pollution measured on August 13th). The measured values stay in a narrow range around 21 pptv on August 4th, 78 pptv on August 6th, 111 pptv on August 7th, 8 pptv on August 11th and 27 pptv on August 13 (without plume air). The average mole fractions vary strongly from one day to another, while the mole fractions of each flight separately are rather uniform. Additionally, all flights show a general slight increase in SO_2 mole fractions, which may lead to the assumption that SO_2 is increased in MCS outflow, while this effect could simply be due to the general evolution of the mole fractions during each flight. On the other hand, looking at the raw data implies that the calculated SO_2 mixing ratios might be real. The reason for the described effect is unclear.

HNO_3 mole fractions from MCS outflow flights show the effectivity of cloud processes for the washout of this trace gas. Decreases of HNO_3 down to 50–100 pptv in the outflow regions of the MCS (9–12 km altitude) contrast mole fractions in the ppbv range that were measured at the same altitudes when no MCS was in close proximity. The uptake of HNO_3 in cloud droplets is responsible for this removal.

6.3 Summary

We have measured different pollution plumes during the two described research campaigns. It was demonstrated that SO_2 pollution can travel long distances in the free troposphere and contribute to the global H_2SO_4 concentration in the clean and cold upper troposphere, where nucleation is favored.

The biomass burning pollution that we observed was intense. The close proximity of the ITCZ and strong convective systems may lead to a further upward transport of such a pollution. These convective transport processes, especially in the region of West African and during the Monsoon season, have been investigated during the AMMA campaign as well. Similar upward transport processes from the boundary layer contributed to the Asian pollution layer that we measured above the North Atlantic and Central Europe. The complexity of the influence of local events on global climate becomes clear, since all discussed topics are interlinked and cannot be understood separately.

Appendix A

General Appendix

A.1 Conversion between Pressure and Altitude

pressure (hPa)	ICAO-height (m)	flight level (FL)
1013	0	0
1000	109	4
900	986	32
850	1455	48
800	1947	64
750	2464	81
700	3010	99
650	3589	118
600	4204	138
550	4863	160
500	5572	183
450	6342	208
400	7183	236
350	8115	266
300	9162	301
275	9739	320
250	10316	340
225	11035	362
200	11773	386

Table A.1: Table of pressure-altitude conversion; ICAO = International Civil Aviation Organisation; list from *http://www.pa.op.dlr.de/amma-dlr/*.

Appendix B

Spring 2006 Campaign

B.1 "SHIPS" — an Example for Pollution by Fossil Fuel Combustion

During SHIPS we investigated the SO_2 in the polluted marine boundary layer (MBL) over the English Channel. The (planetary) boundary layer is generally characterized by friction with the surface and extends up to 1 km, followed by the free troposphere [Roedel, 1994]. Wind velocities are virtually uniform and air is rapidly transported, resulting in a well mixed layer [Brasseur et al., 1999]. The MBL in particular is lower (about 500 m) because of the flat surface of the sea, while the continental boundary layer (CBL) extends higher up due to turbulences caused by topographical characteristics (up to 2 km).

The MBL is generally much cleaner than the CBL layer, but the amount of pre-existing aerosol is high due to sea salt particles that originate from sea spray. Gaseous sulfur components in the MBL are strongly influenced by ship traffic that uses heavy oil with a high sulfur content of up to 5 %. Since a large number of sea salt aerosol is present new particle formation through H_2SO_4 from ship emissions is not favored. Instead, the growth of aerosol particles to form cloud condensation nuclei and droplets is enhanced by the ships´emissions.

Figure B.1 shows typical SO_2 data from our aircraft based measurement in the marine boundary layer, made by our group in April 2006 over the English Channel. The flights were part of the SHIPS campaign, organized by the German Aerospace Centre (Deutsches Zentrum für Luft- und Raumfahrt — DLR) in Oberpfaffenhofen. The altitude profiles clearly

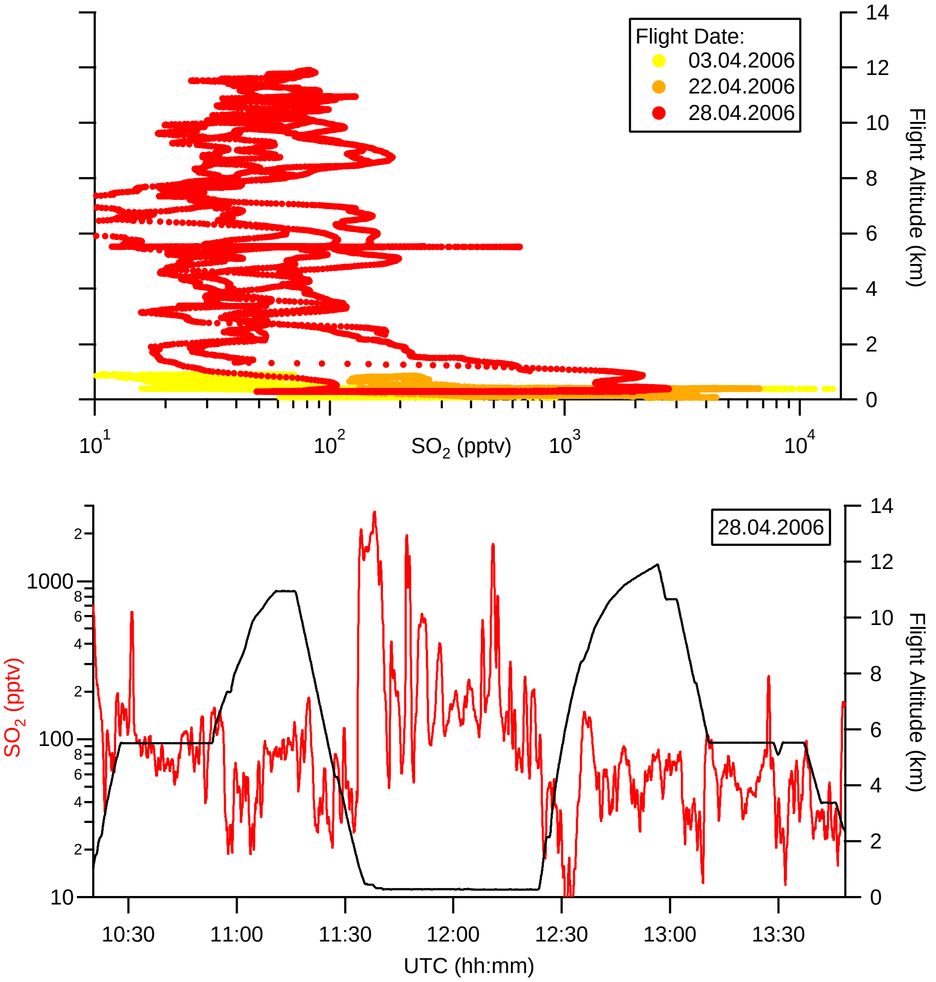

Figure B.1: SO$_2$ data from three SHIPS flights: altitude profiles for three flights (above), and time series for one flight (below). Ship exhaust was measured during the low flight section from about 11:30–12:30 UTC.

show the increase in SO$_2$ from ship exhaust in low altitudes of a few hundred meters. The most polluted plume that exhibits mixing ratios of 10 ppbv was intercepted by the research aircraft at about 400 m altitude.

The decrease with altitude in SO$_2$ of about two orders of magnitude on April 3rd shows that the pollution is not significant above about 800–1300 m, where mixing with lower layers is weak. The air above the English Channel was generally hazy, accounting for the growth of particles due to pollution. The time series below shows the increase in SO$_2$ downward from about 2 km. Some distinct narrow peaks originate from penetration of single exhaust plumes by the aircraft. A broader peak at about 11:40 am marks the passage through a major ship route.

B.2 Additional Figures

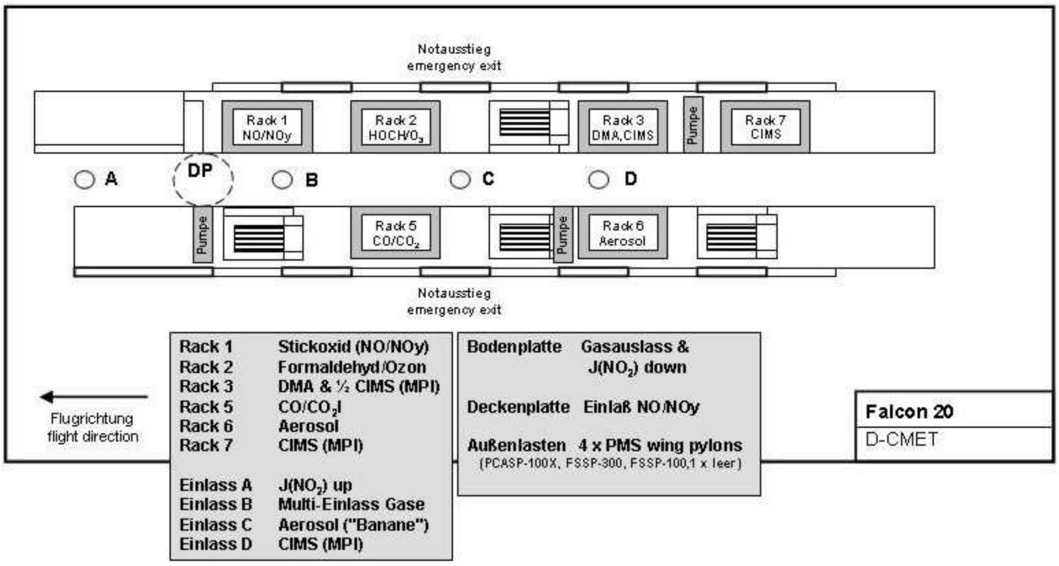

Figure B.2: *Falcon* payload during the spring 2006 campaign. All instruments were operated by the DLR IPA the CIMS instrument by our group.

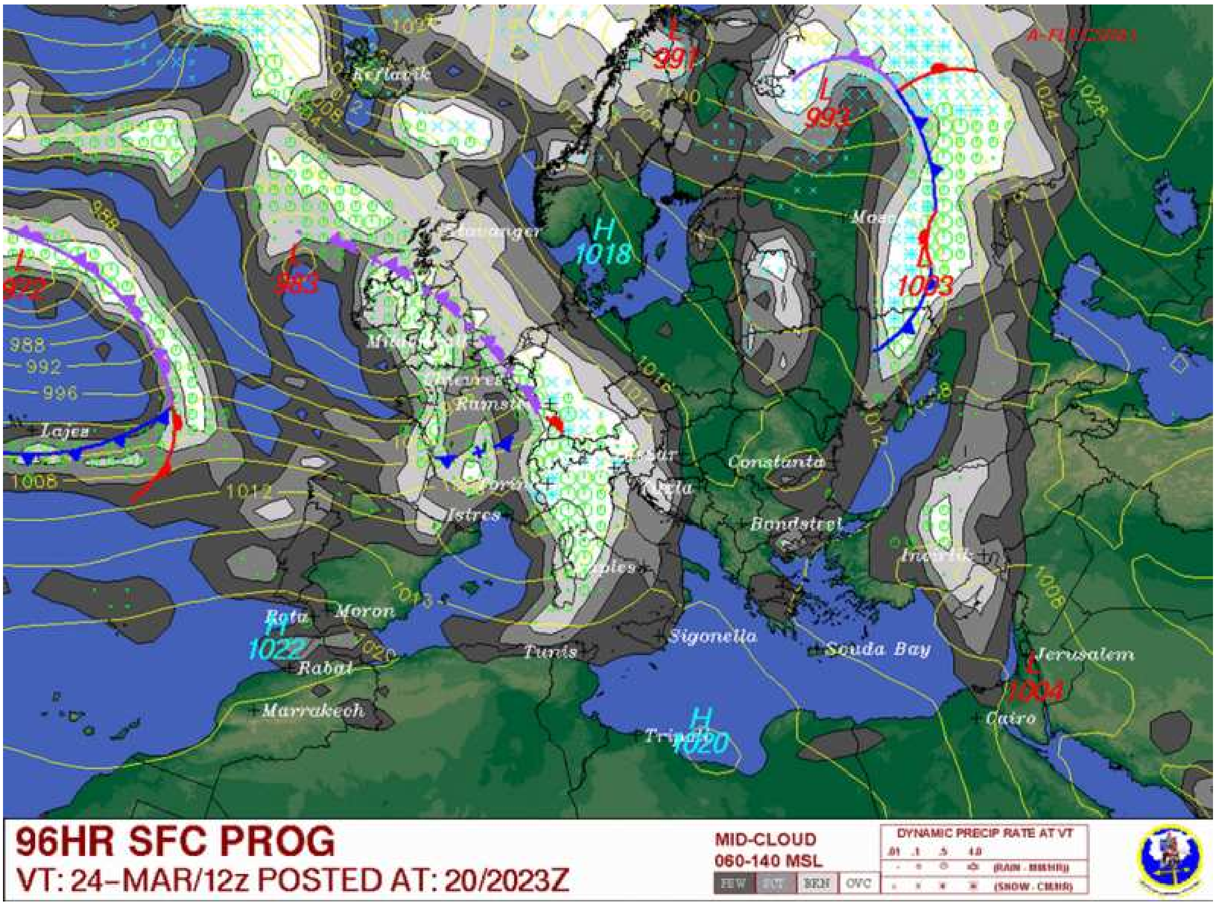

Figure B.3: 96 hour forecast for March 24th. Provided by the DLR-IPA as part of flight planning and quicklook data. The low is west of Ireland. The trough is visible as the cloudy area over Central Europe.

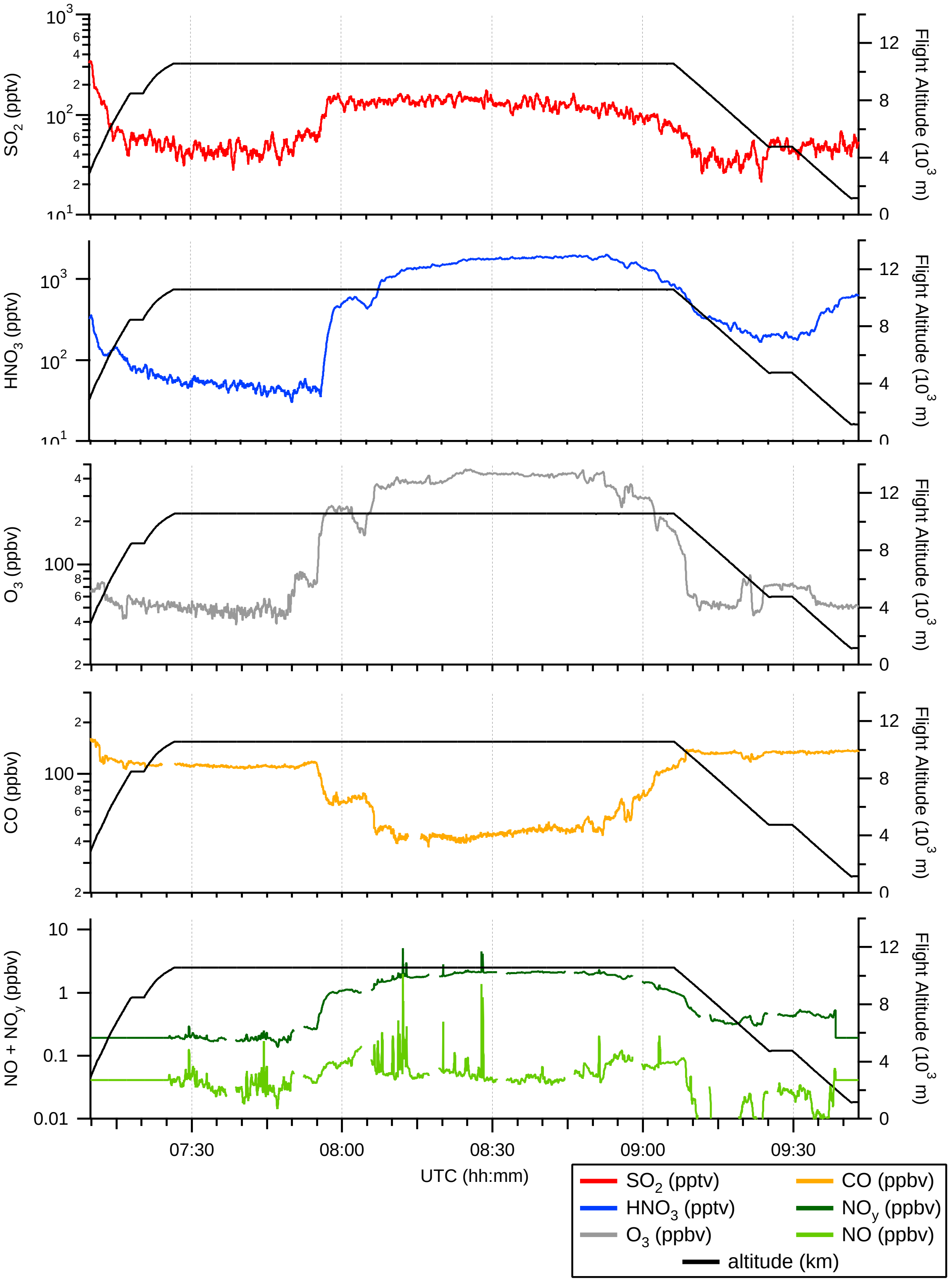

Figure B.4: 24.03.2006 Flight 1

Figure B.5: SO_2 and HNO_3 by MPI-K, O_3, CO, NO, NO_y and altitudes by DLR IPA for the first flight on March 24th.

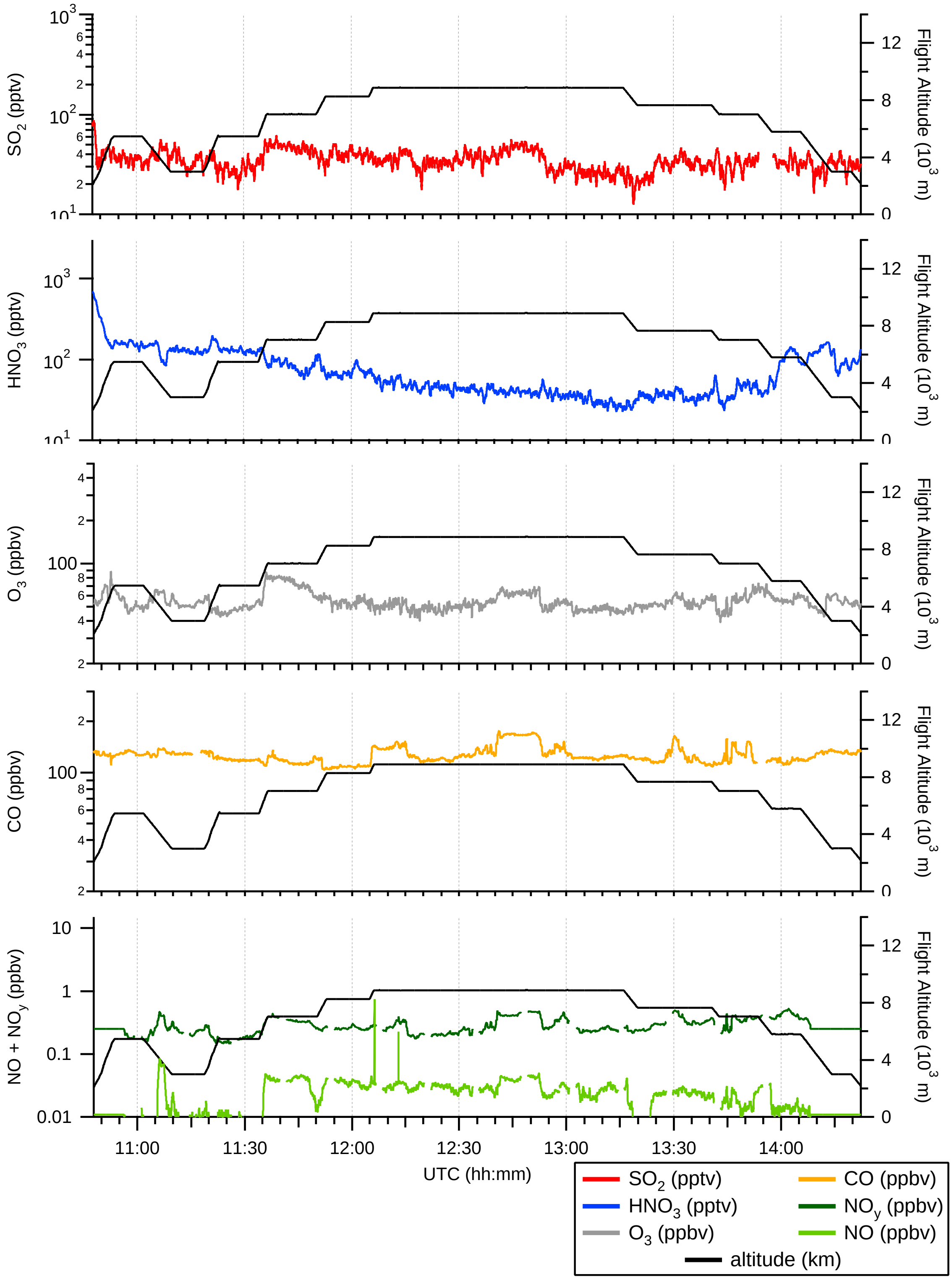

Figure B.6: SO_2 and HNO_3 by MPI-K, O_3, CO, NO, NO_y and altitudes by DLR IPA for the second flight on March 24th — referred to as Flight A

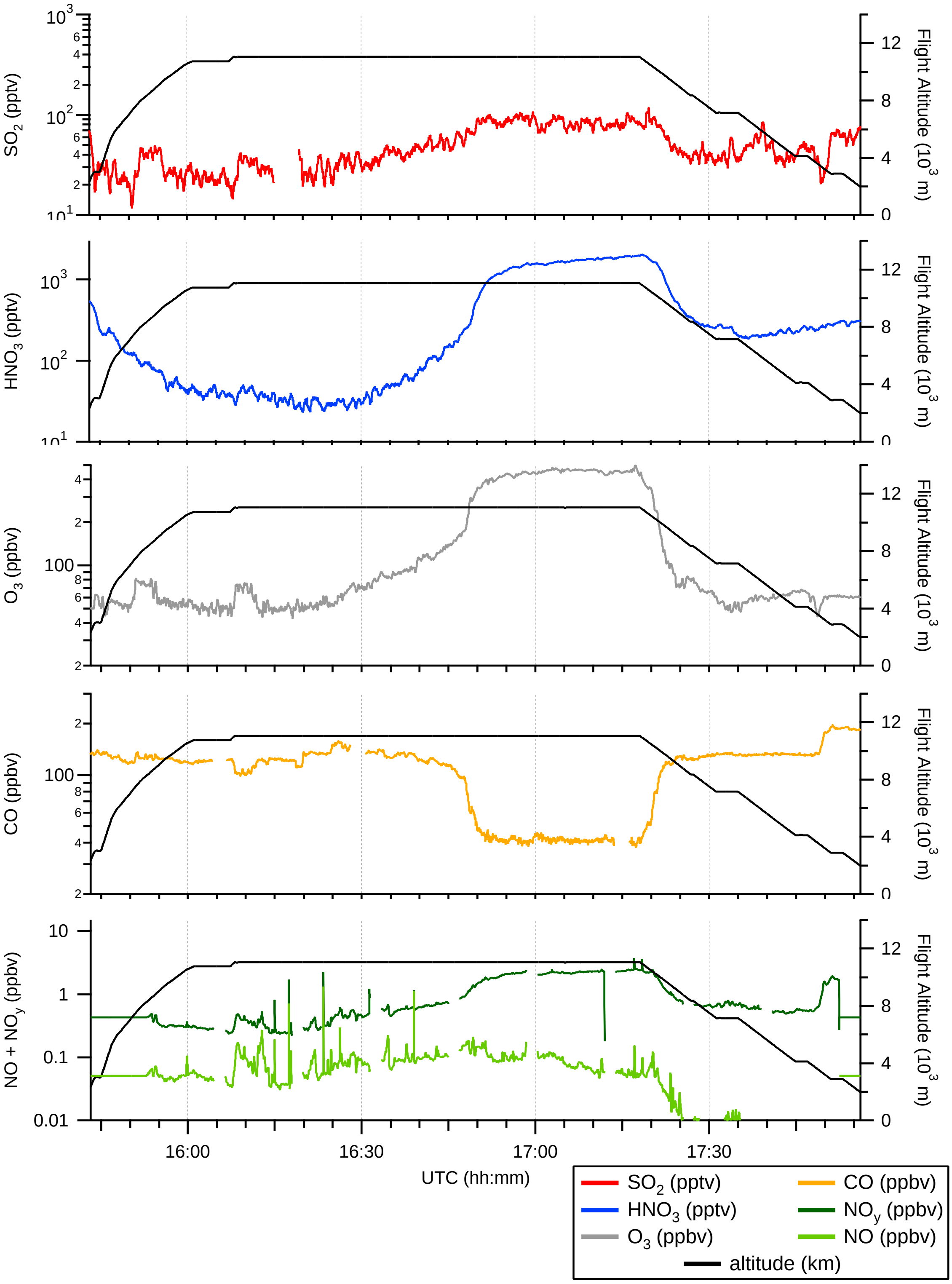

Figure B.7: SO_2 and HNO_3 by MPI-K, O_3, CO, NO, NO_y and altitudes by DLR IPA for the third flight on March 24th.

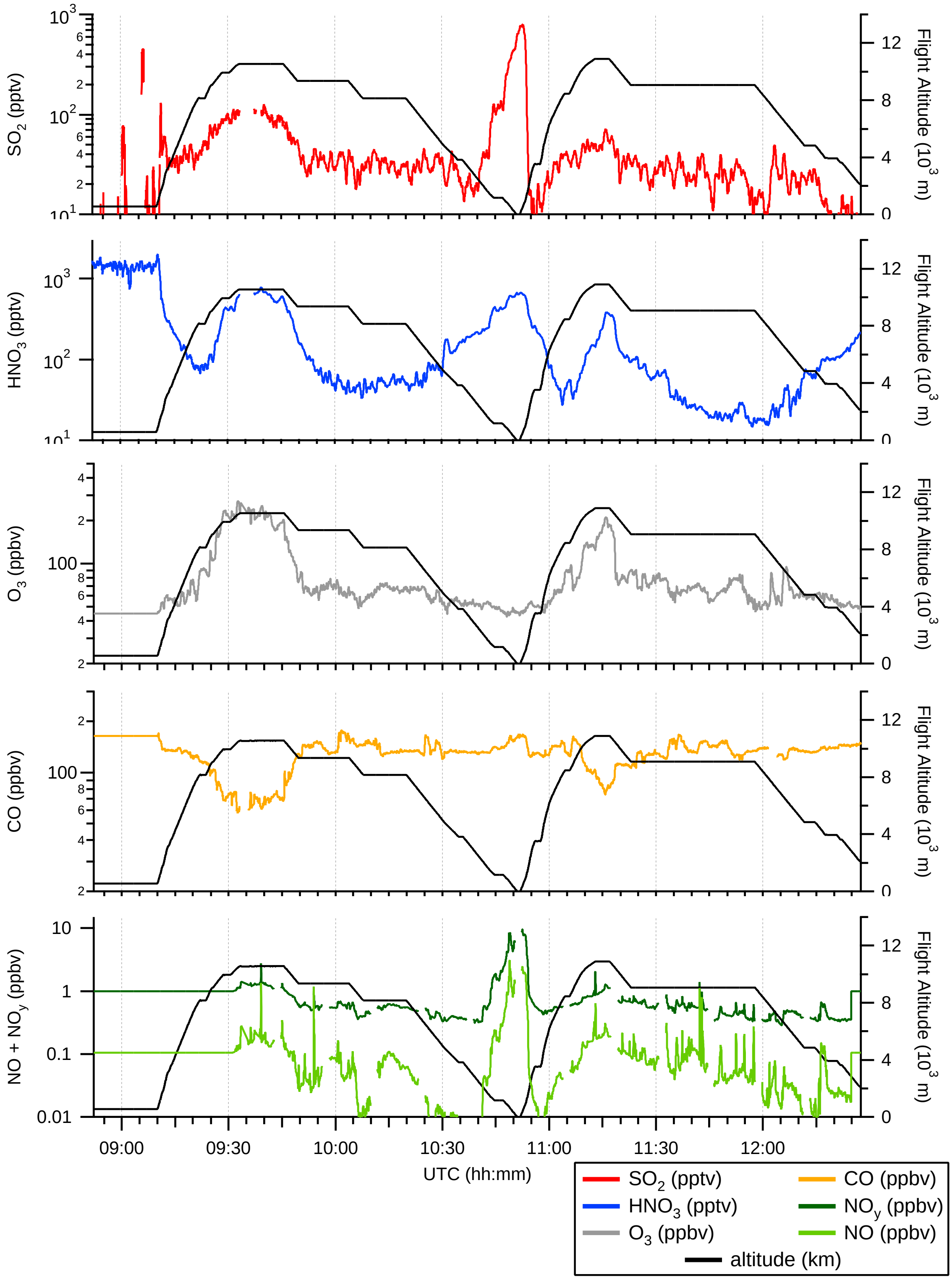

Figure B.8: SO_2 and HNO_3 by MPI-K, O_3, CO, NO, NO_y and altitudes by DLR IPA for the single flight on March 25th — referred to as Flight B

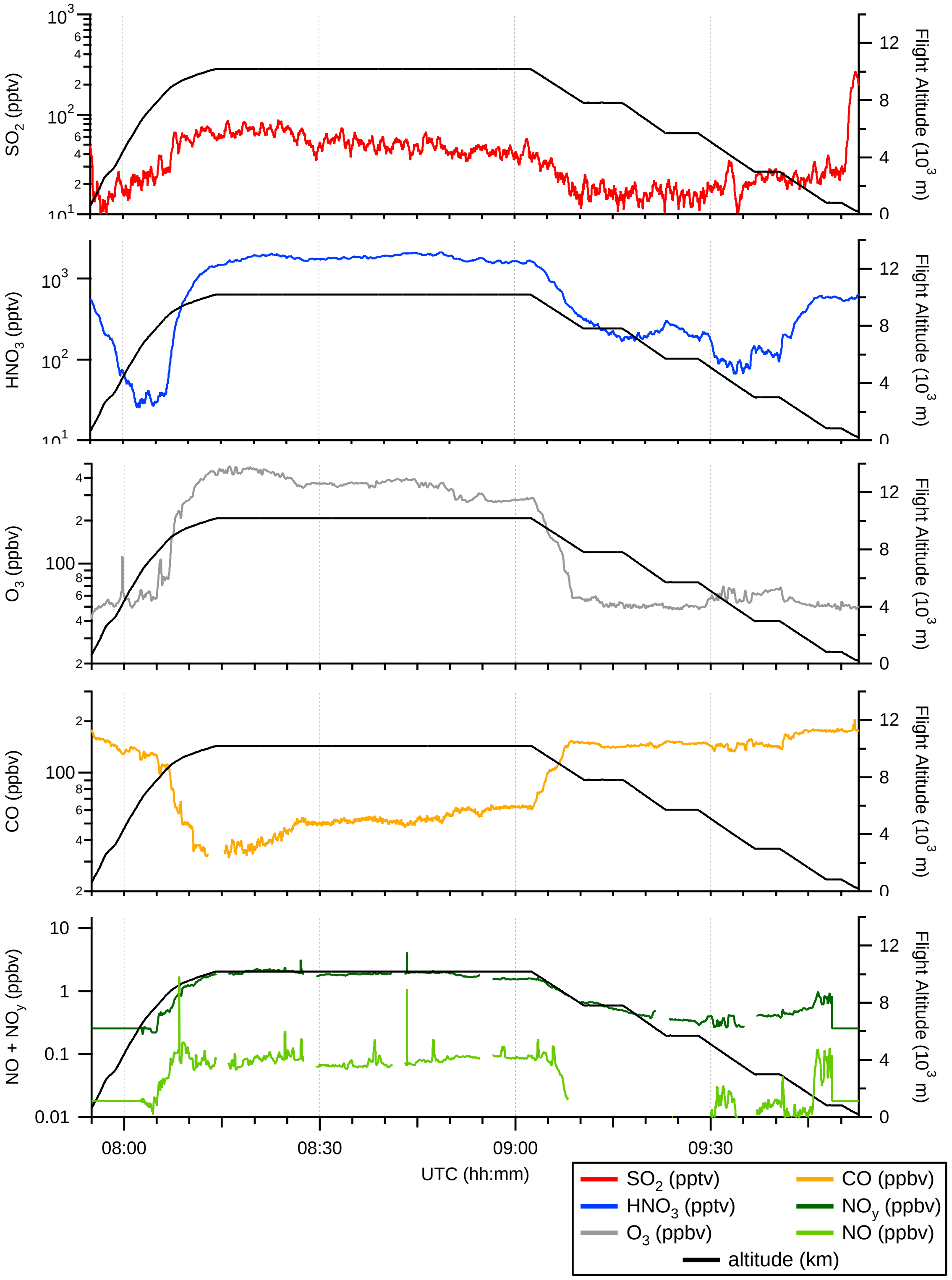

Figure B.9: SO_2 and HNO_3 by MPI-K, O_3, CO, NO, NO_y and altitudes by DLR IPA for the first flight on April 3rd.

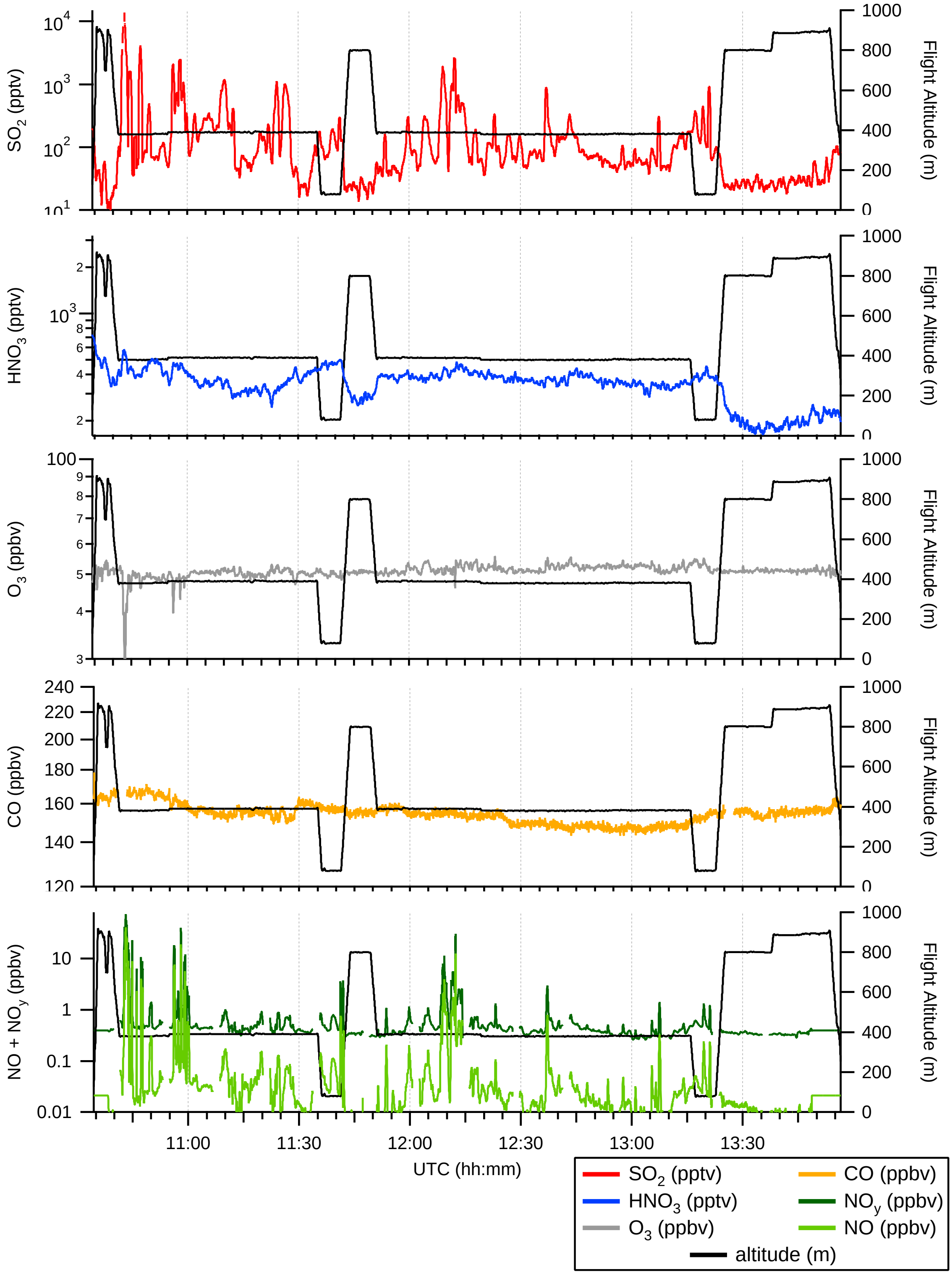

Figure B.10: SO_2 and HNO_3 by MPI-K, O_3, CO, NO, NO_y and altitudes by DLR IPA for the second flight on April 3rd.

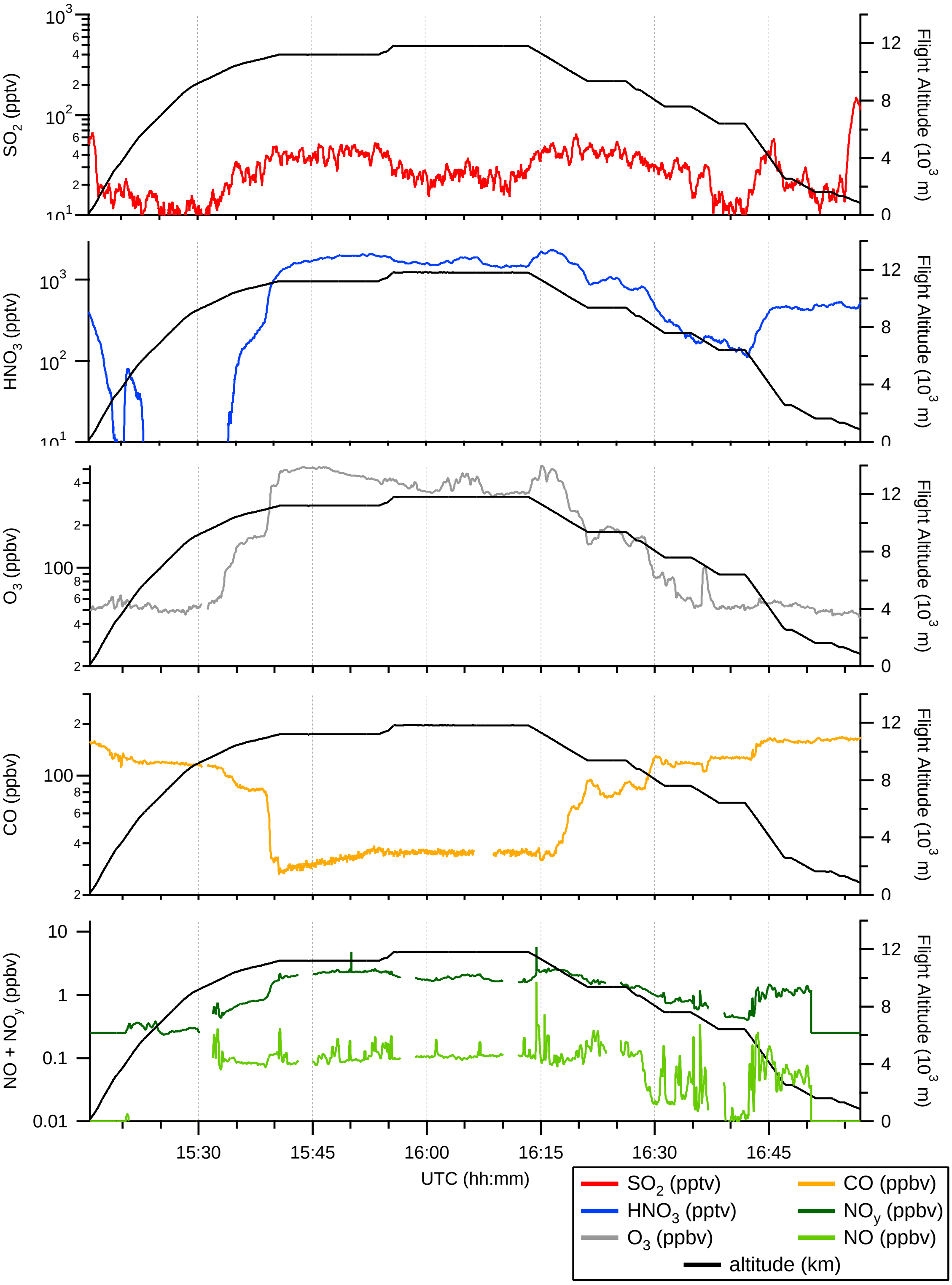

Figure B.11: SO_2 and HNO_3 by MPI-K, O_3, CO, NO, NO_y and altitudes by DLR IPA for the third flight on April 3rd.

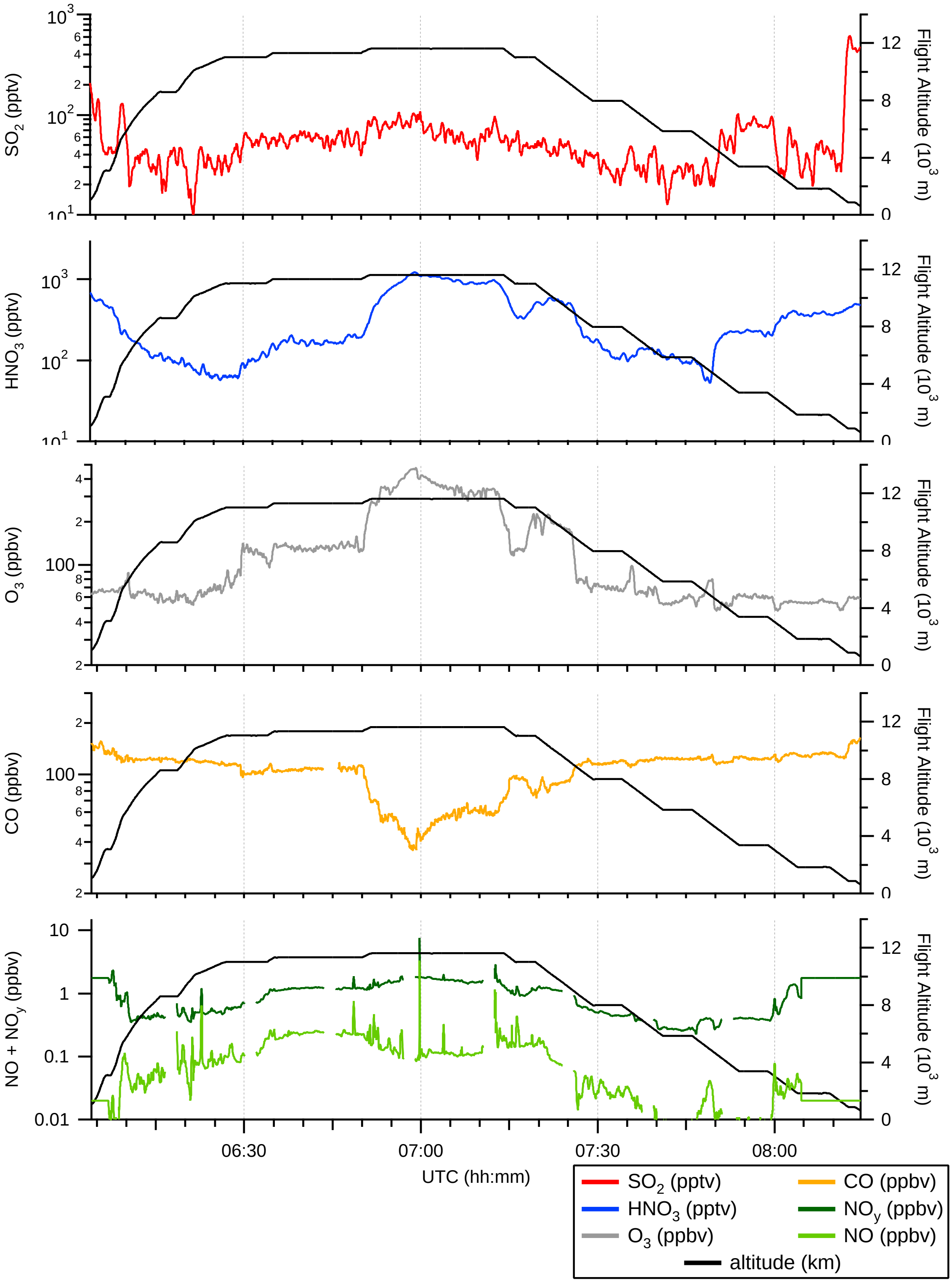

Figure B.12: SO_2 and HNO_3 by MPI-K, O_3, CO, NO, NO_y and altitudes by DLR IPA for the first flight on April 22nd.

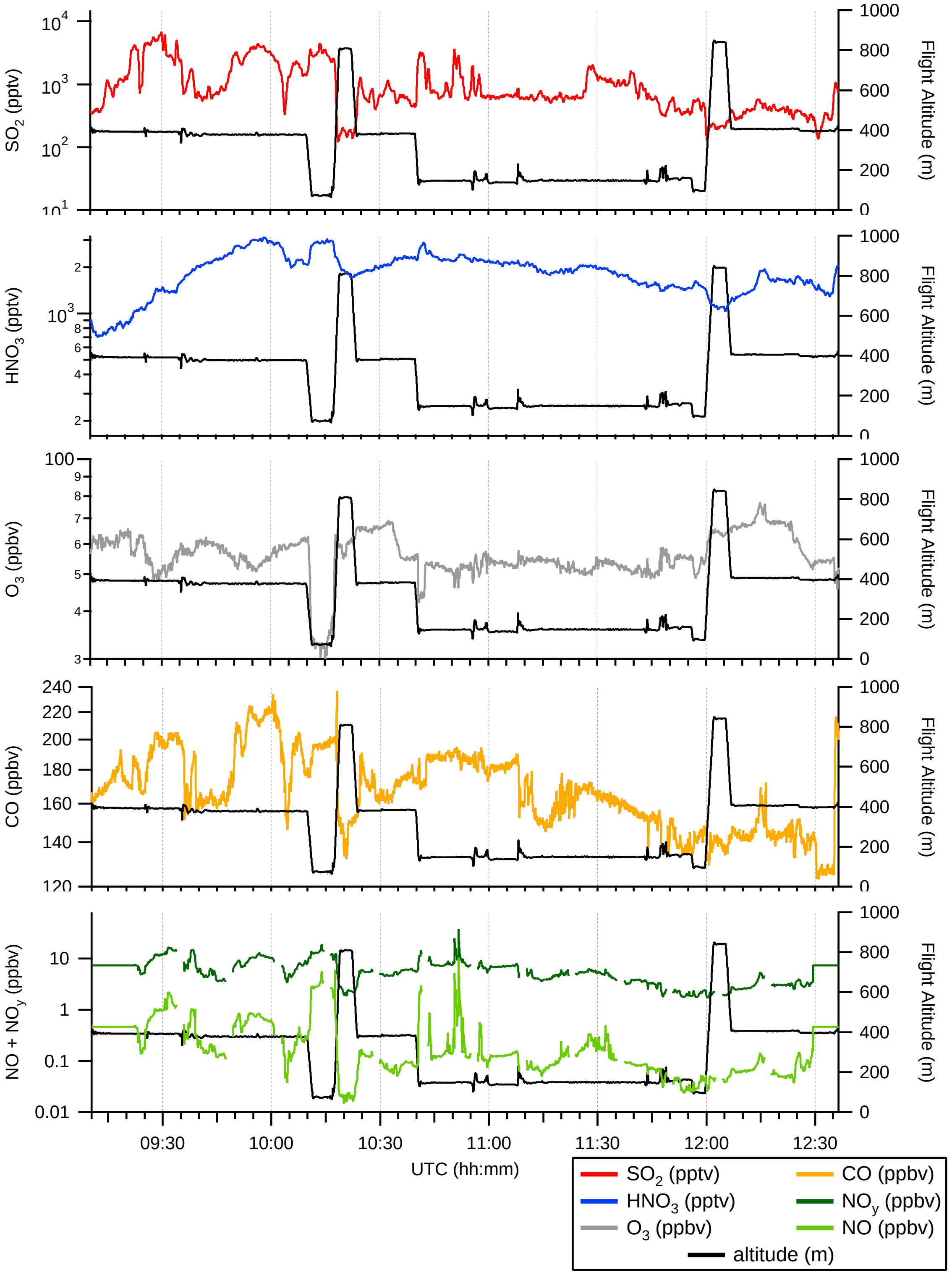

Figure B.13: SO_2 and HNO_3 by MPI-K, O_3, CO, NO, NO_y and altitudes by DLR IPA for the second flight on April 22nd.

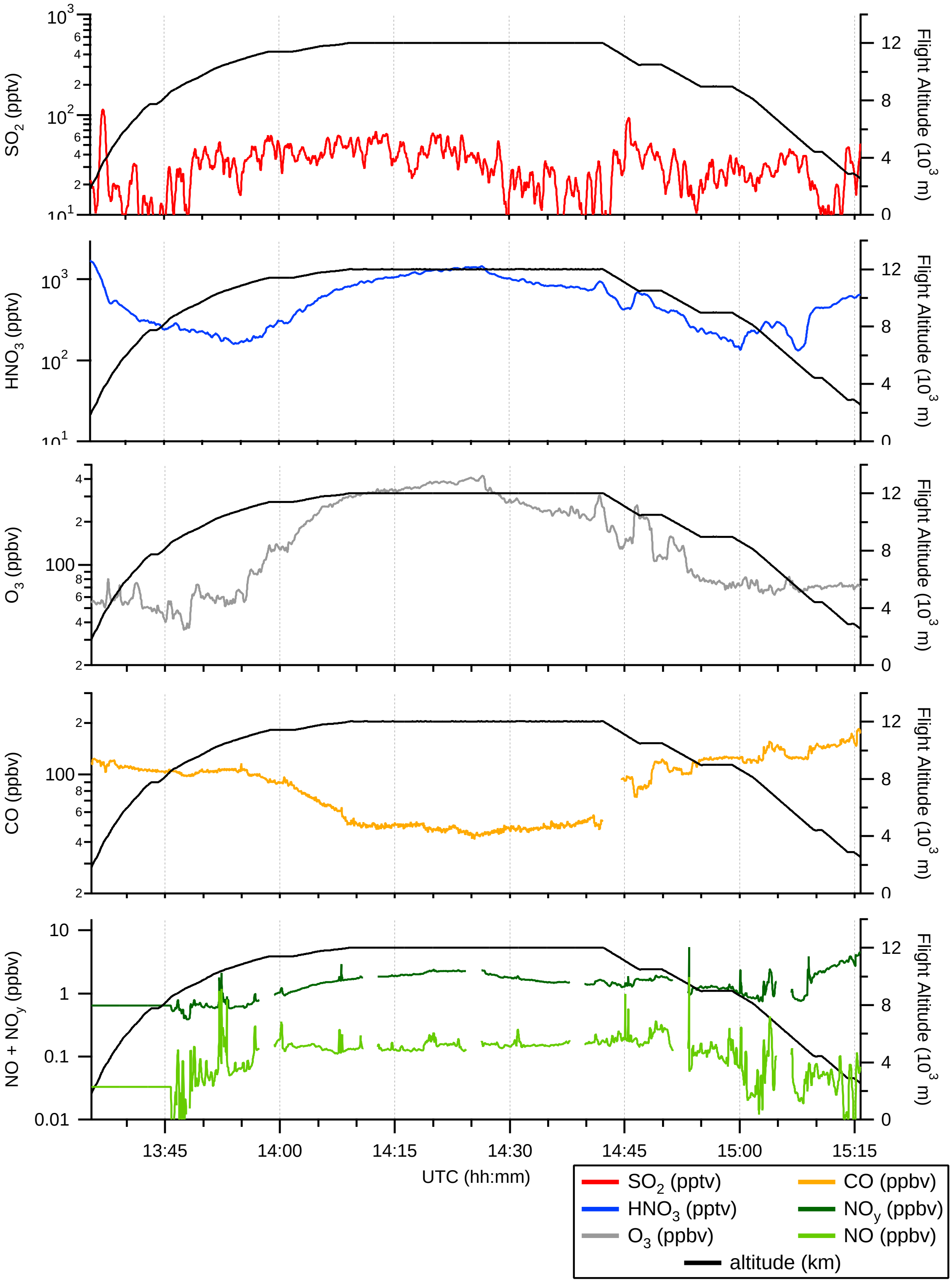

Figure B.14: SO_2 and HNO_3 by MPI-K, O_3, CO, NO, NO_y and altitudes by DLR IPA for the third flight on April 22nd.

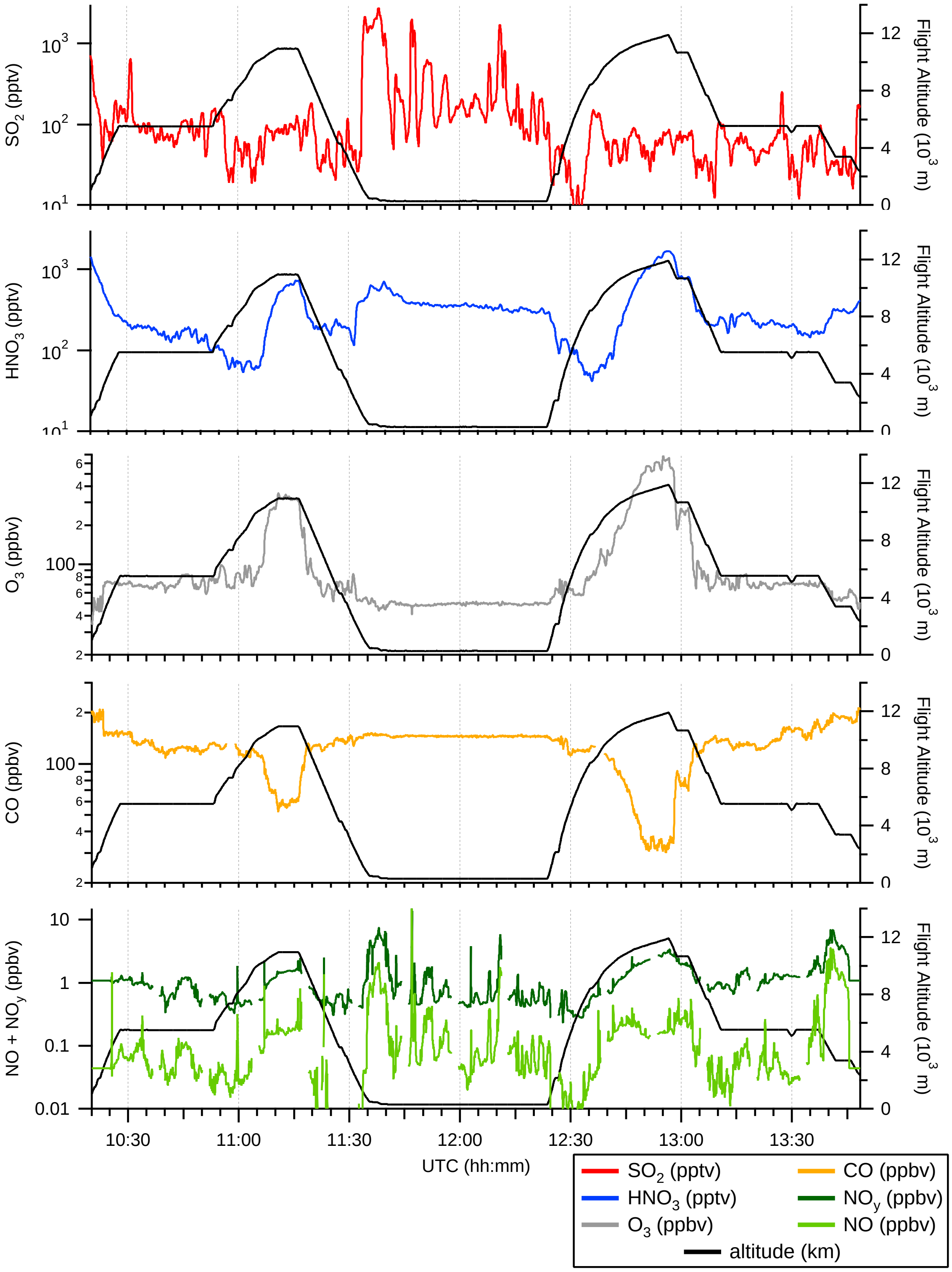

Figure B.15: SO_2 and HNO_3 by MPI-K, O_3, CO, NO, NO_y and altitudes by DLR IPA for the single flight on April 28th.

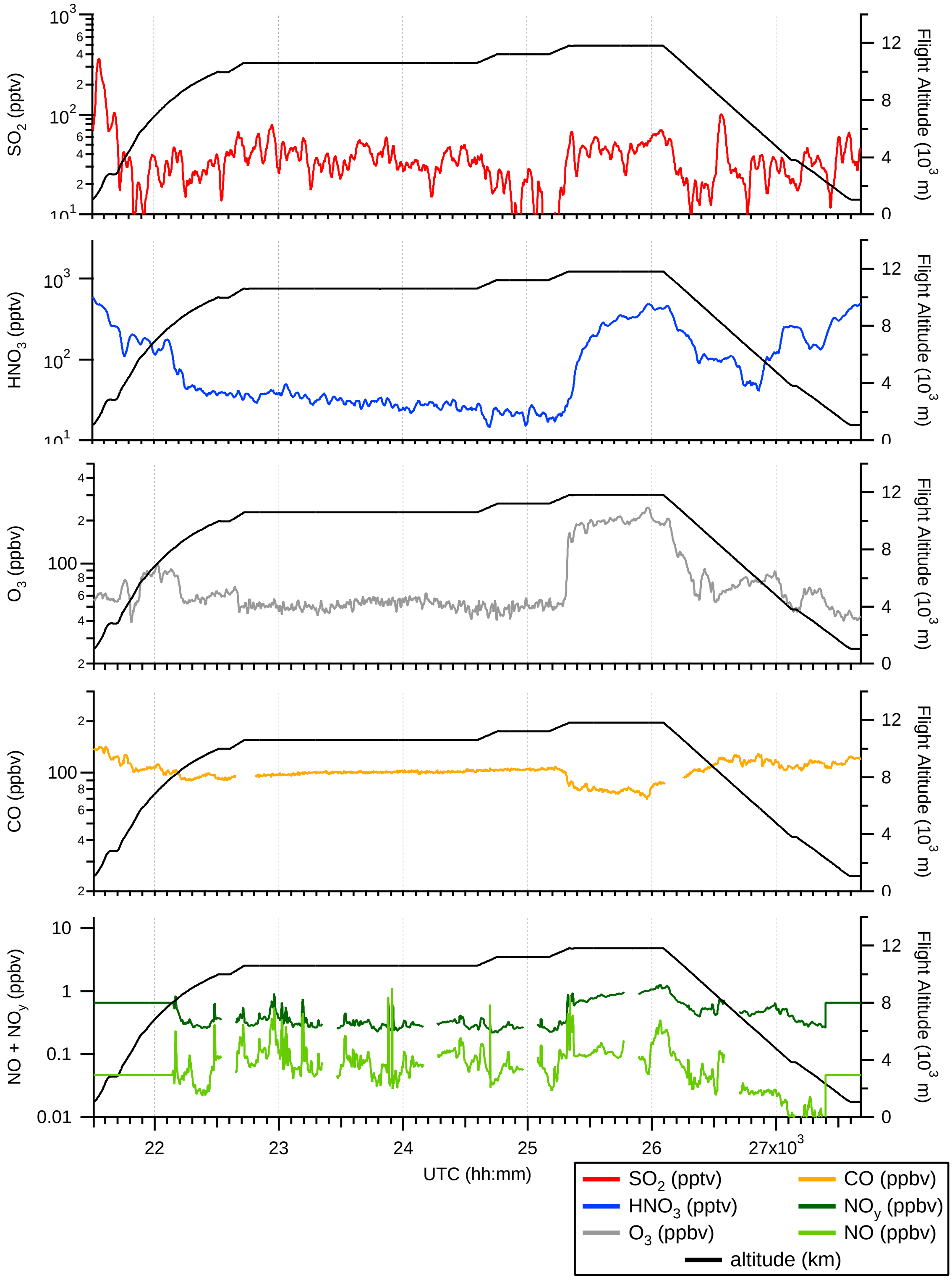

Figure B.16: SO_2 and HNO_3 by MPI-K, O_3, CO, NO, NO_y and altitudes by DLR IPA for the first flight on May 3rd.

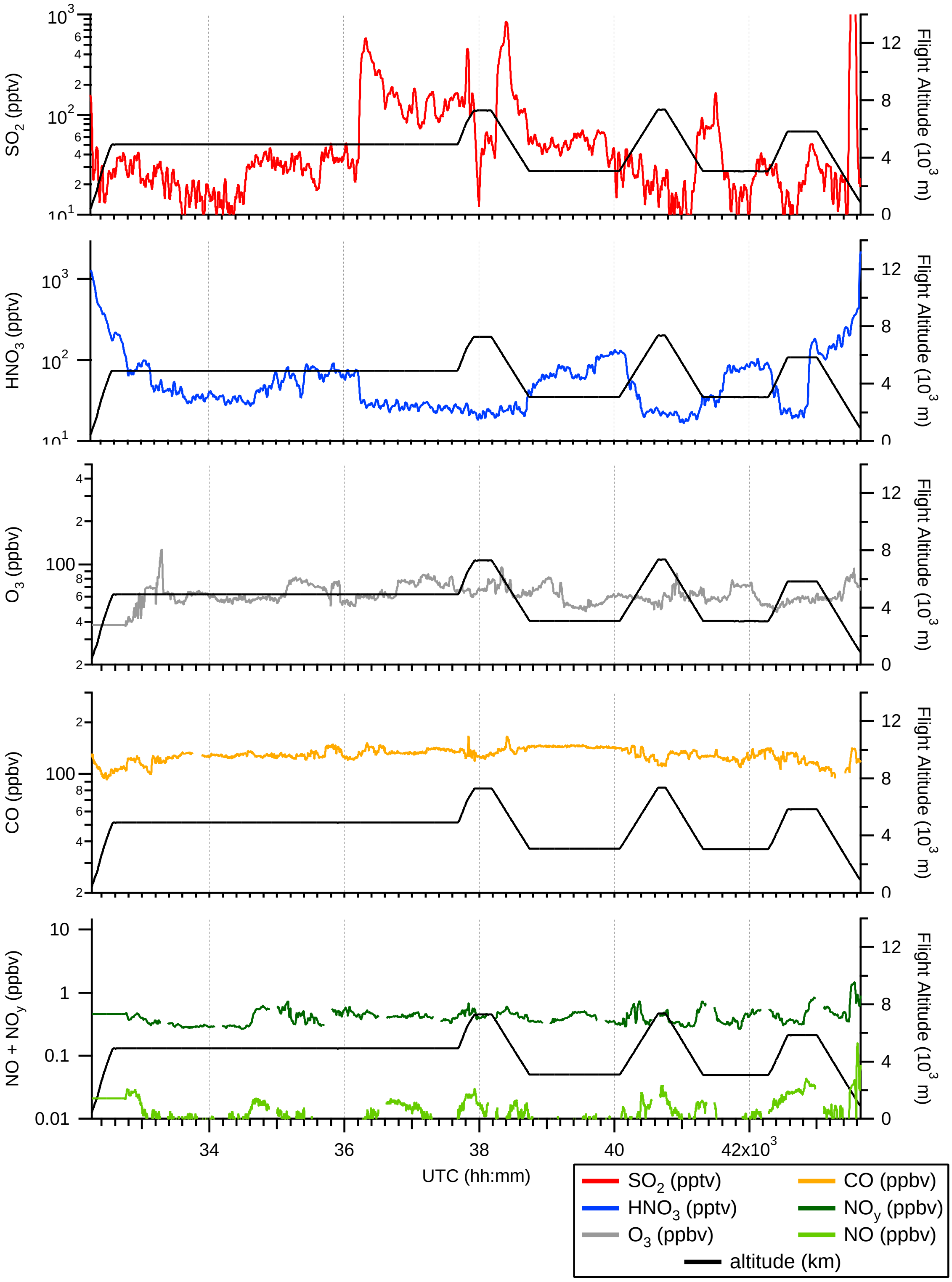

Figure B.17: SO_2 and HNO_3 by MPI-K, O_3, CO, NO, NO_y and altitudes by DLR IPA for the second flight on May 3rd.

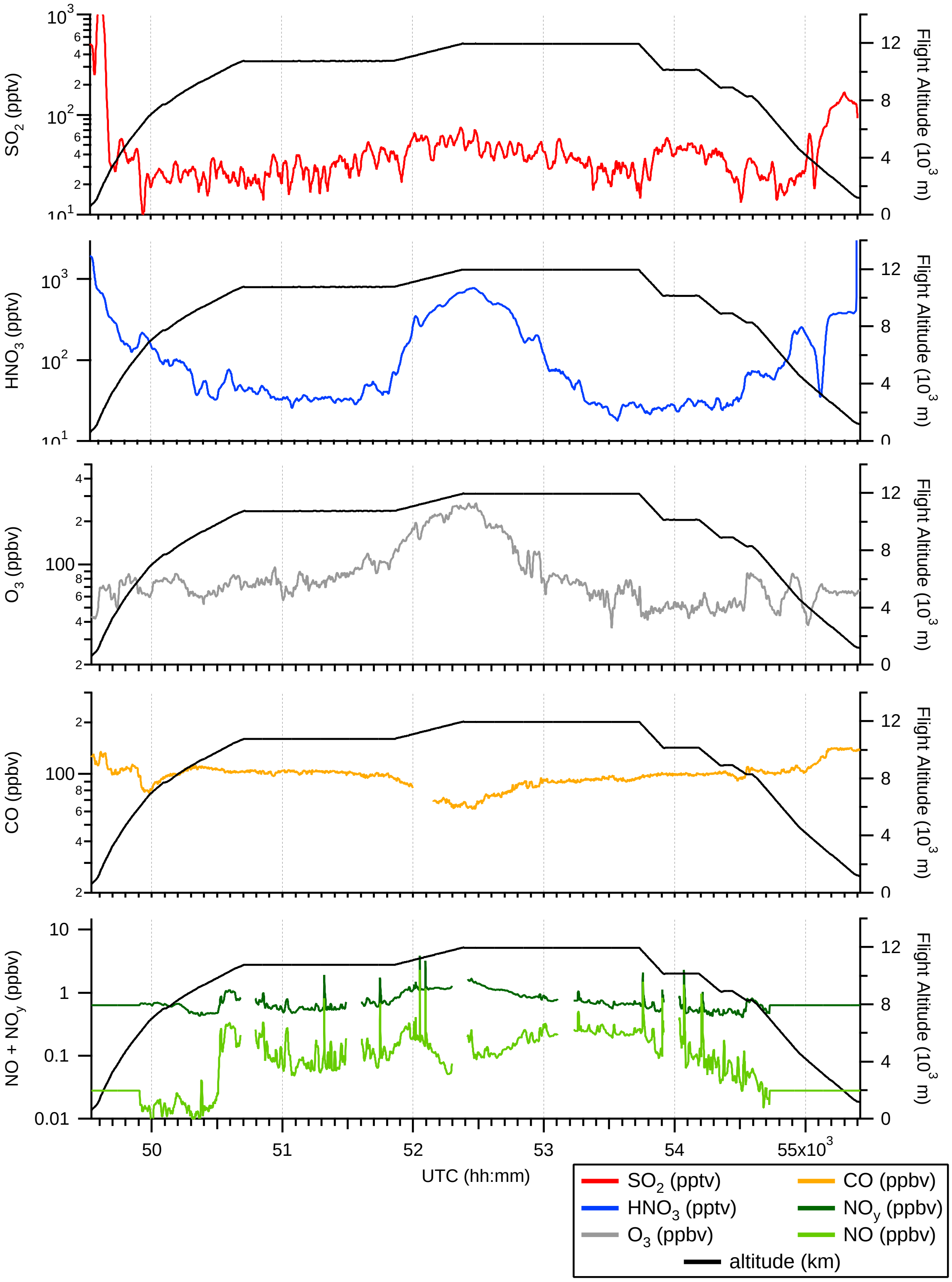

Figure B.18: SO_2 and HNO_3 by MPI-K, O_3, CO, NO, NO_y and altitudes by DLR IPA for the third flight on May 3rd.

Appendix C

AMMA Campaign

C.1 Additional Figures

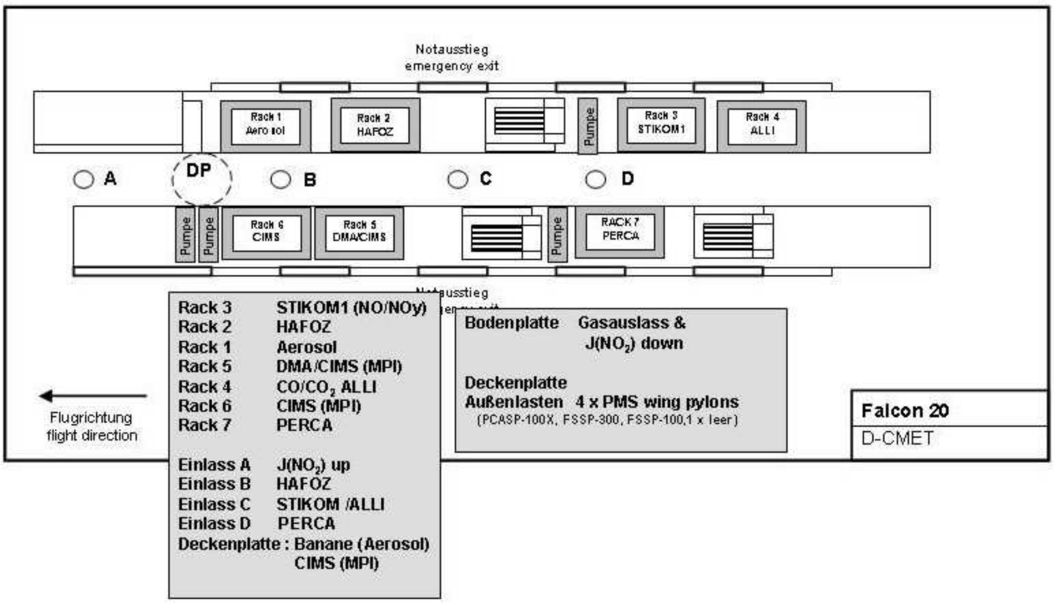

Figure C.1: *Falcon* payload during AMMA-SOP. All instruments were operated by the DLR IPA except for PERCA (University of Bremen) and the CIMS instrument by our group.

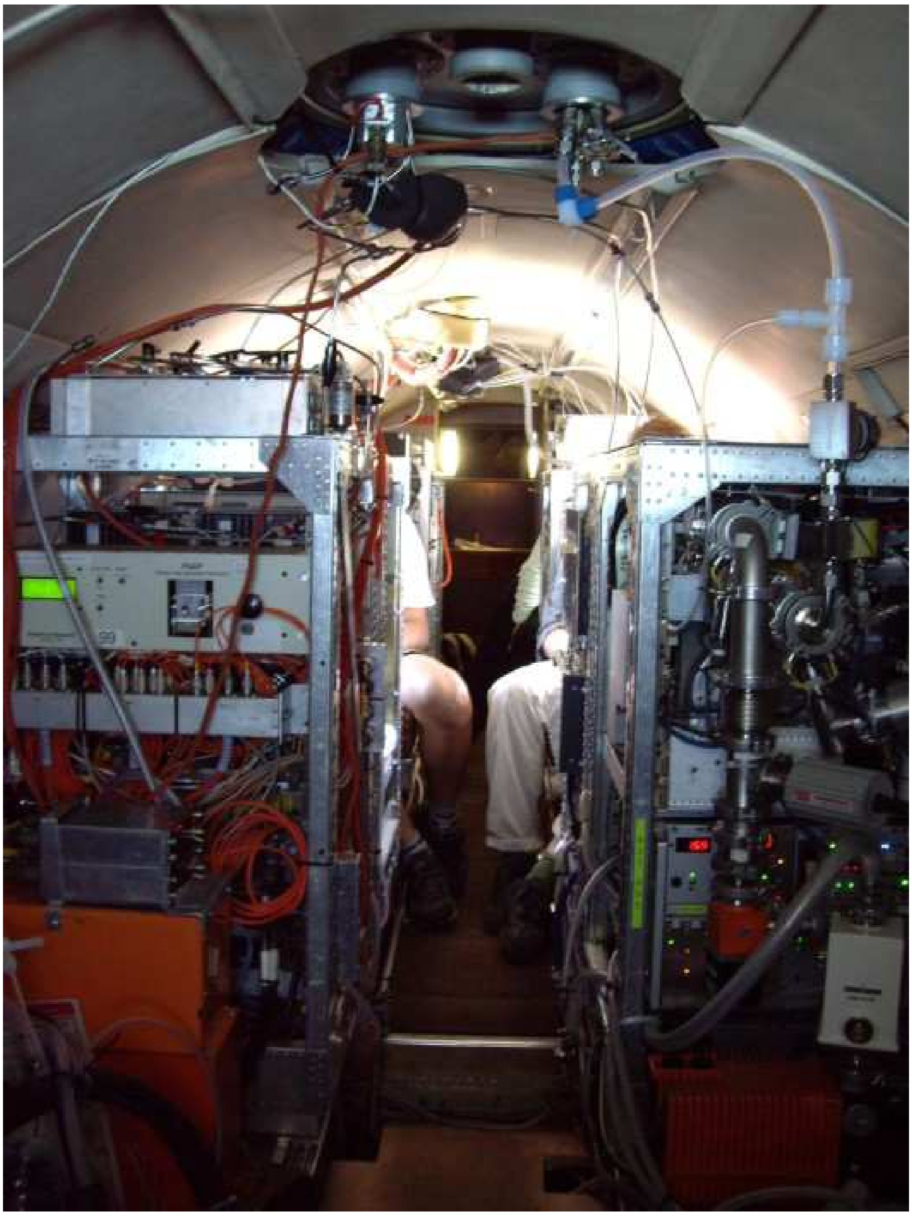

Figure C.2: The interior of the *Falcon* during the AMMA-SOP campaign, looking from front to rear. Our instrument is on the right. Our PFA (Perfluoralkoxy-Copolymer) inlet system that penetrates the ceiling of the aircraft is visible.

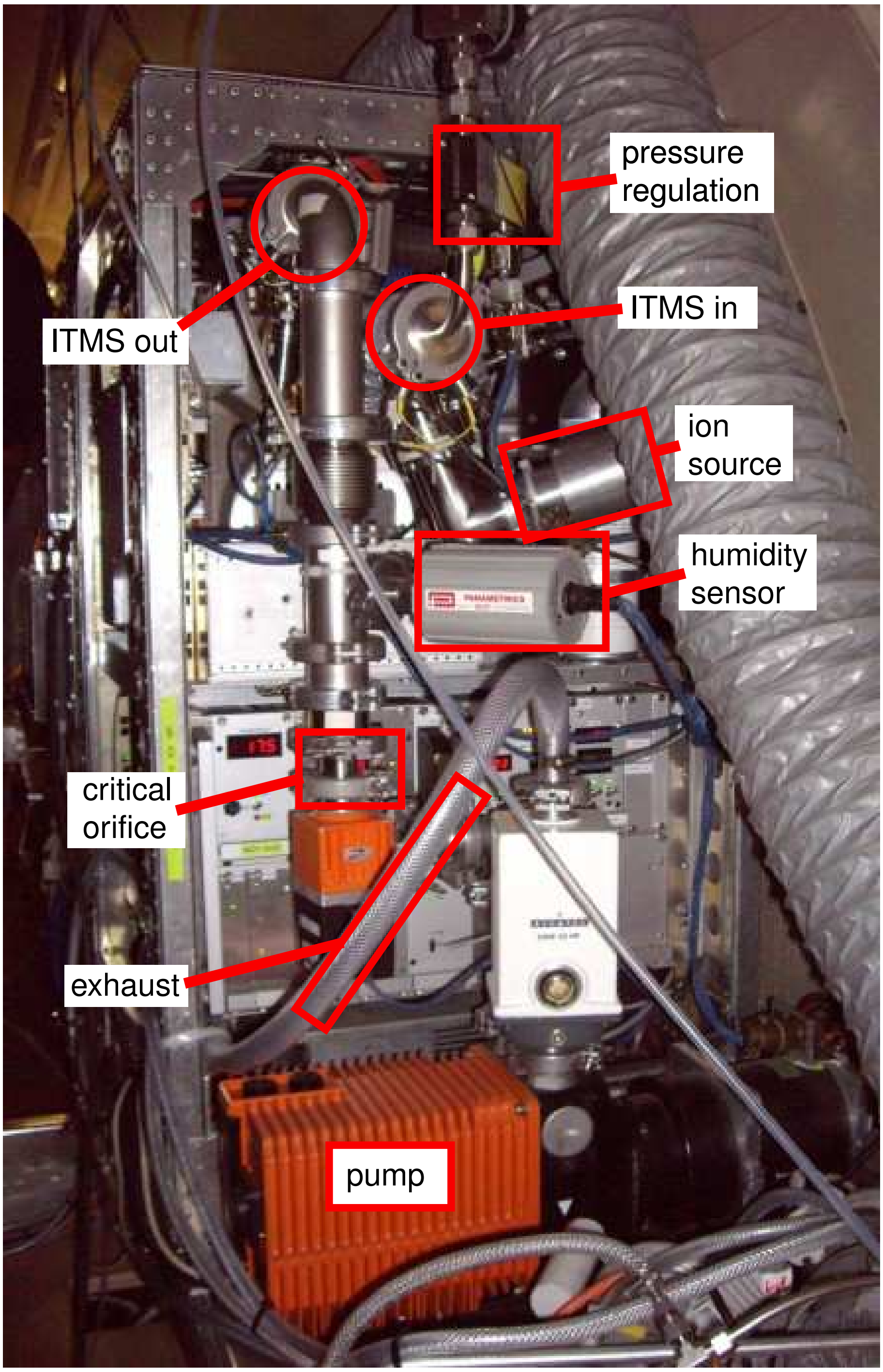

Figure C.3: The CIMS spectrometer setup for AMMA-SOP inside the *Falcon*. The grey hose was part of the external air conditioning. Compare the photograph with the schematic view in figure 3.3

.

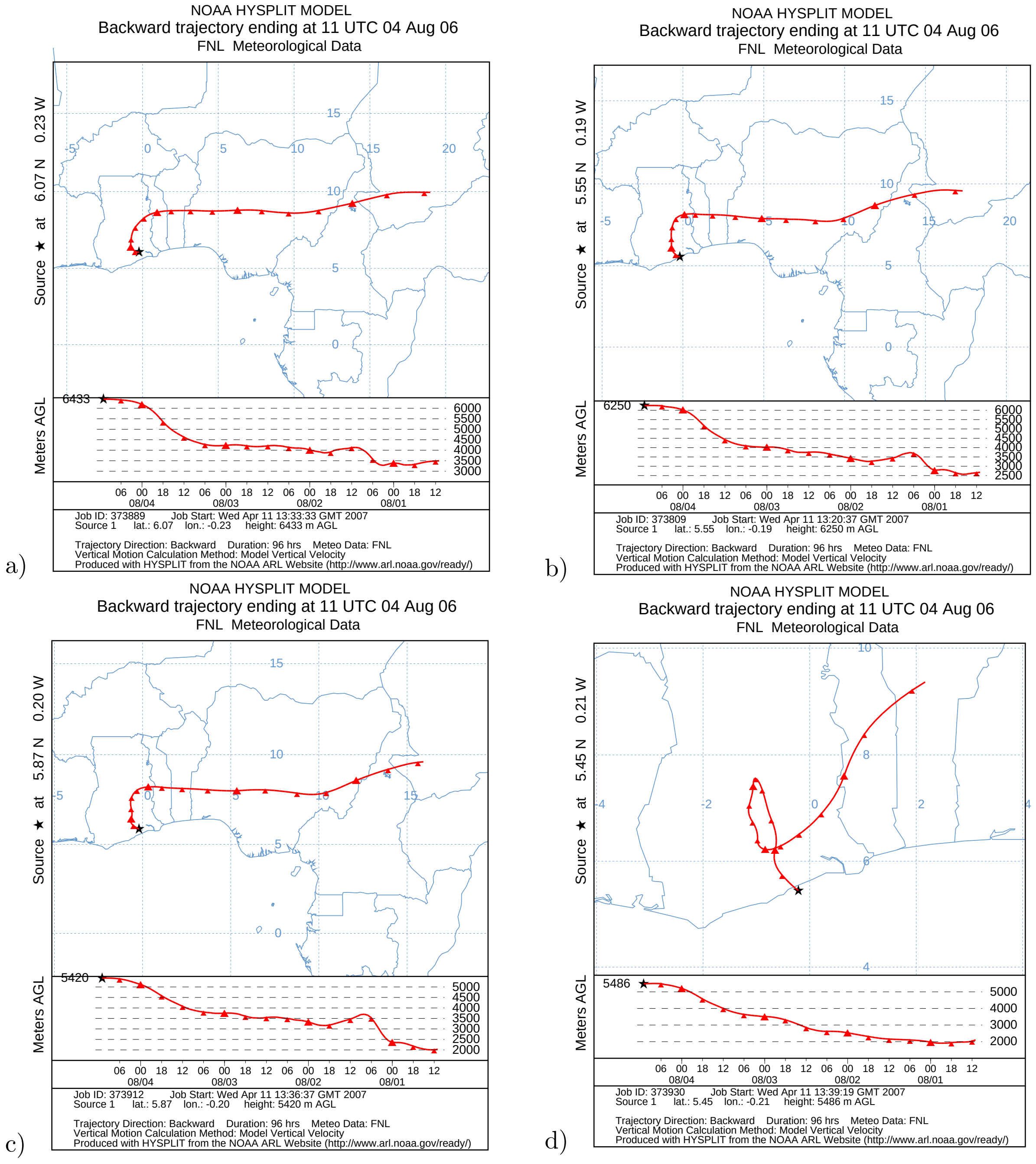

Figure C.4: HYSPLIT 4 day back trajectories [Draxler and Hess, 1998, Draxler and Rolph, 2003], starting on August 4th at 11 UTC.

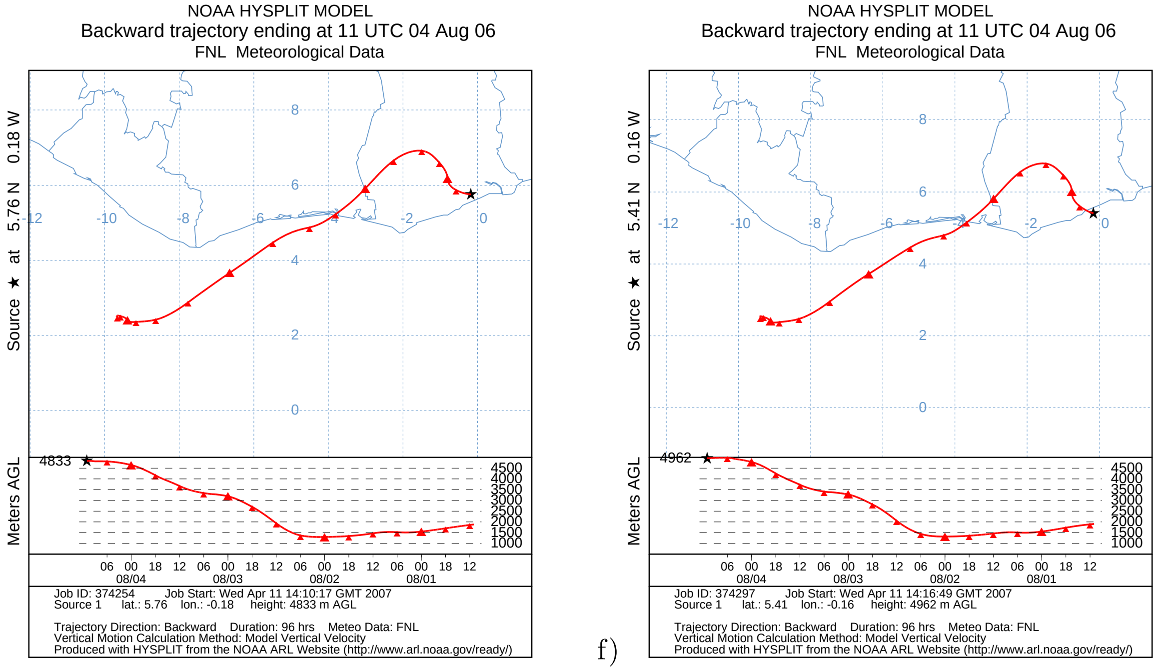

e) f)

Figure C.5: HYSPLIT 4 day back trajectories [Draxler and Hess, 1998, Draxler and Rolph, 2003], starting on August 4th at 11 UTC.

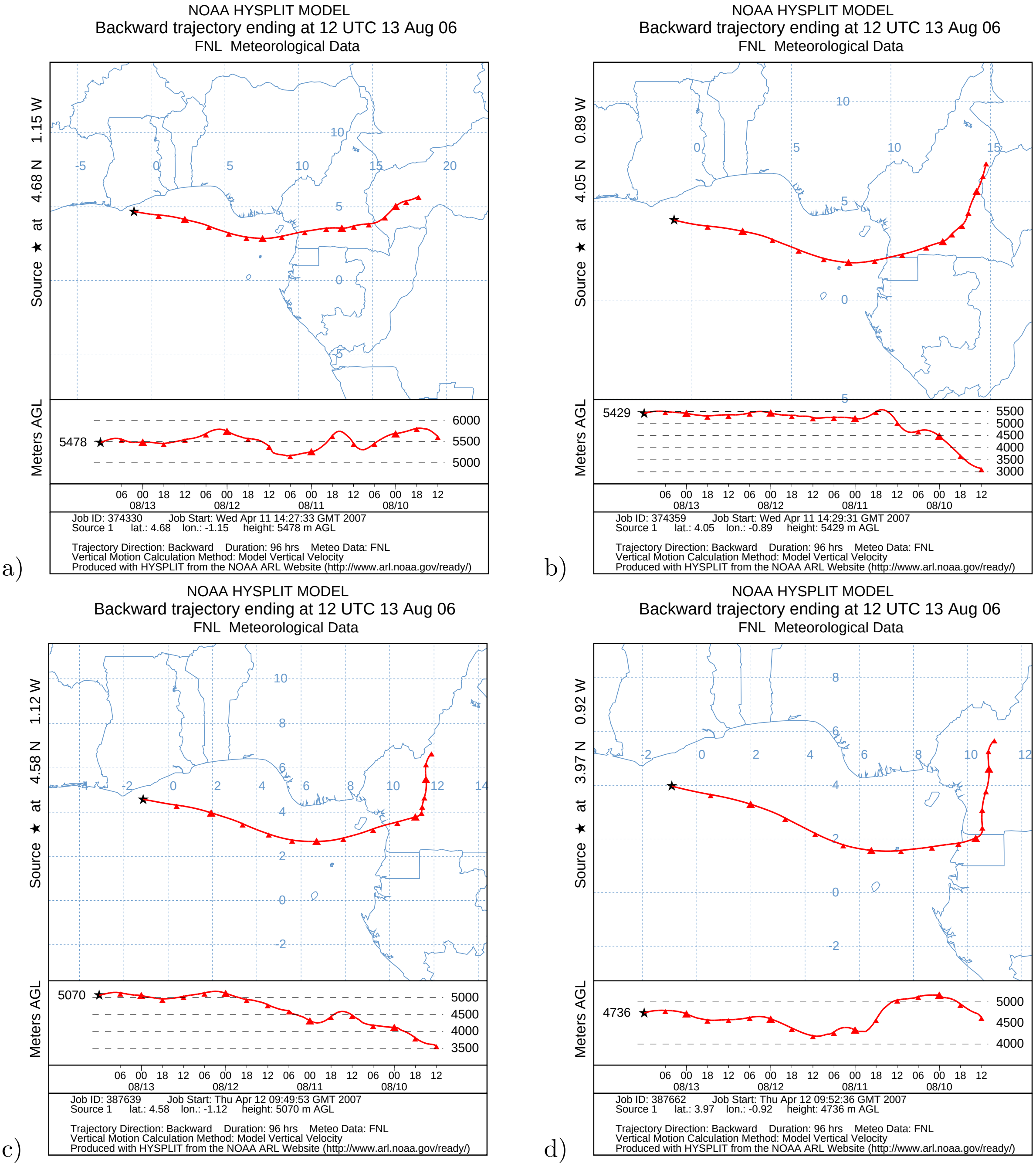

Figure C.6: HYSPLIT 4 day back trajectories [Draxler and Hess, 1998, Draxler and Rolph, 2003], starting on August 13th at 12 UTC.

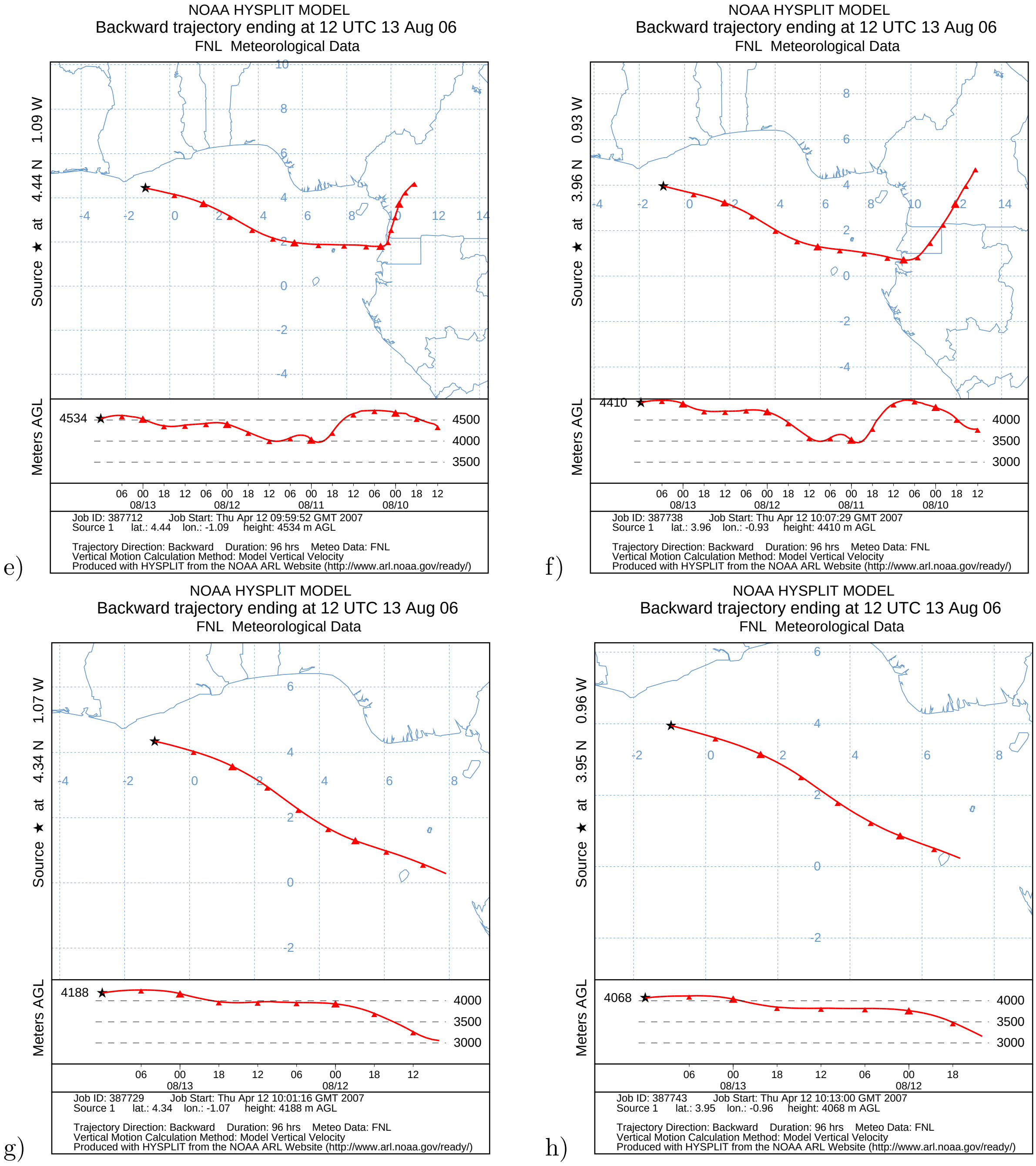

Figure C.7: HYSPLIT 4 day back trajectories [Draxler and Hess, 1998, Draxler and Rolph, 2003], starting on August 13th at 12 UTC. The two bottom trajectories are cut off after about 48 hours backwards, when they reach the equator.

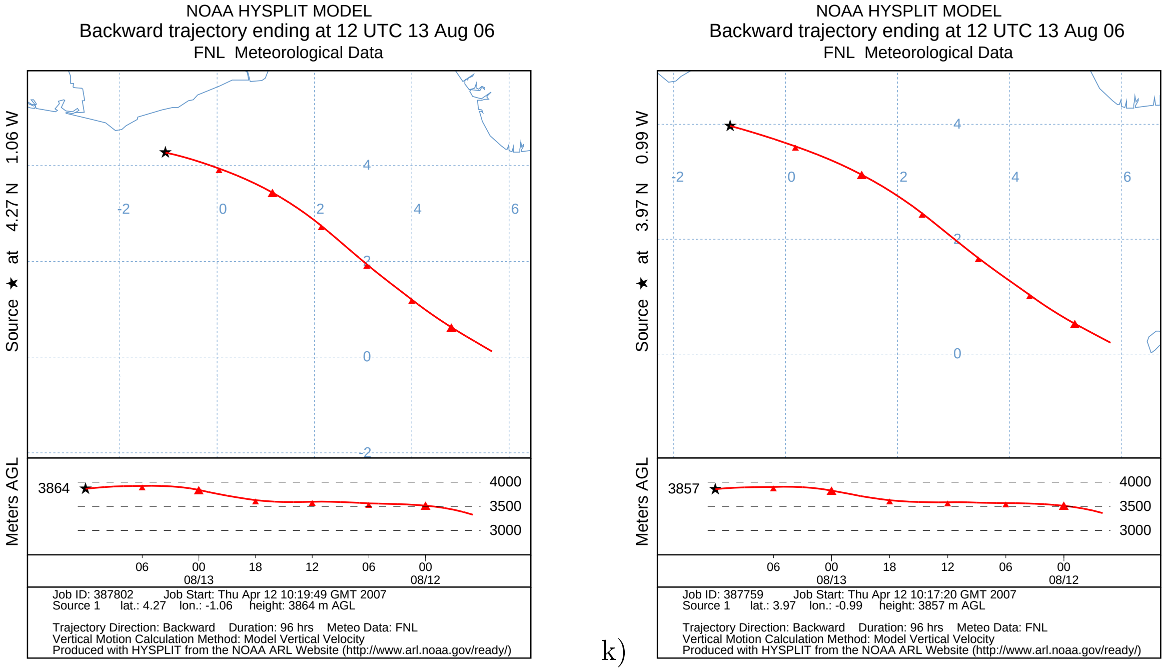

i) k)

Figure C.8: HYSPLIT back trajectories [Draxler and Hess, 1998, Draxler and Rolph, 2003], starting on August 13th at 12 UTC. The trajectories are cut off after about 48 hours backwards, when they reach the equator.

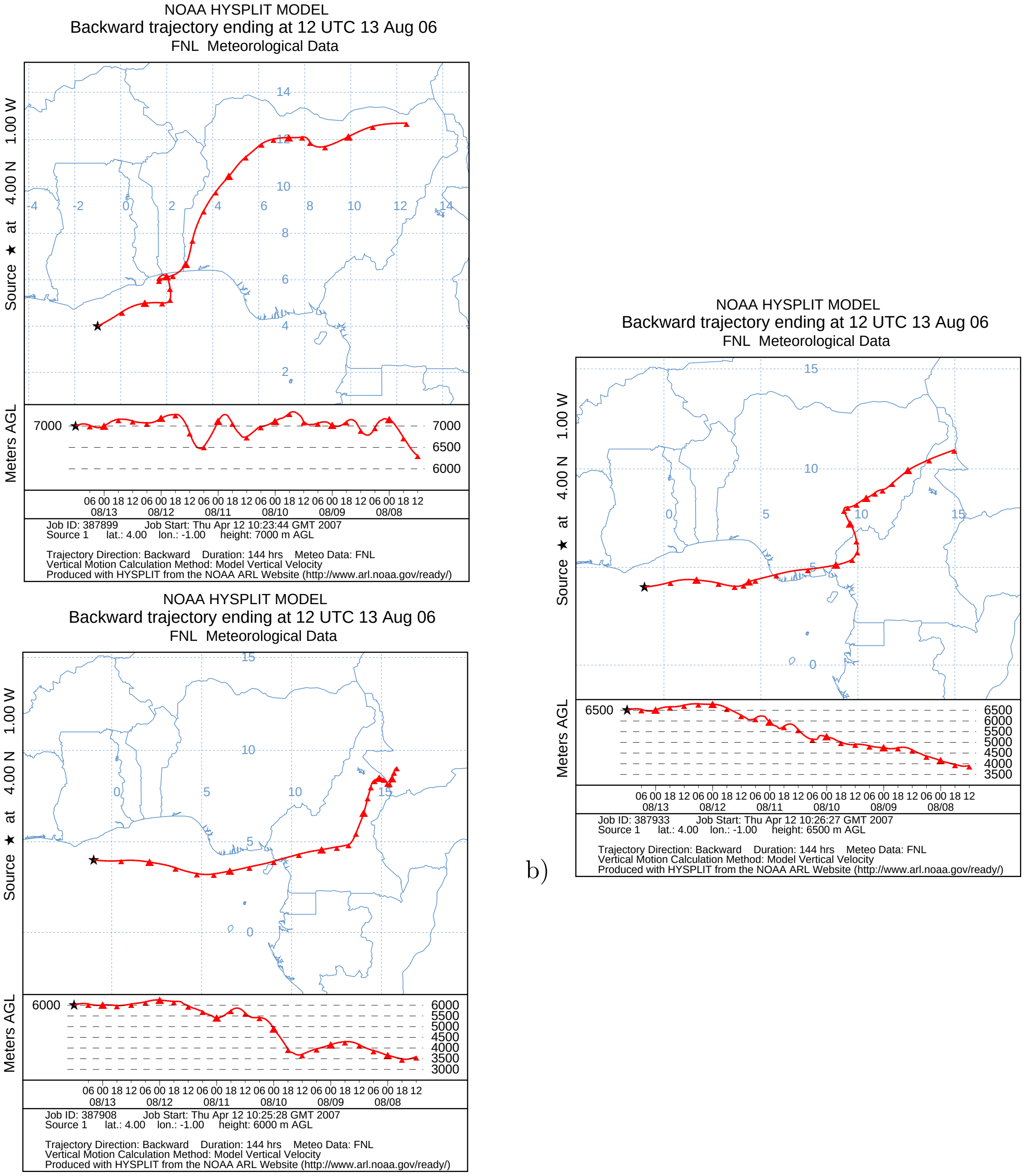

a)

b)

c)

Figure C.9: HYSPLIT 6 day back trajectories [Draxler and Hess, 1998, Draxler and Rolph, 2003], starting on August 13th at 12 UTC.

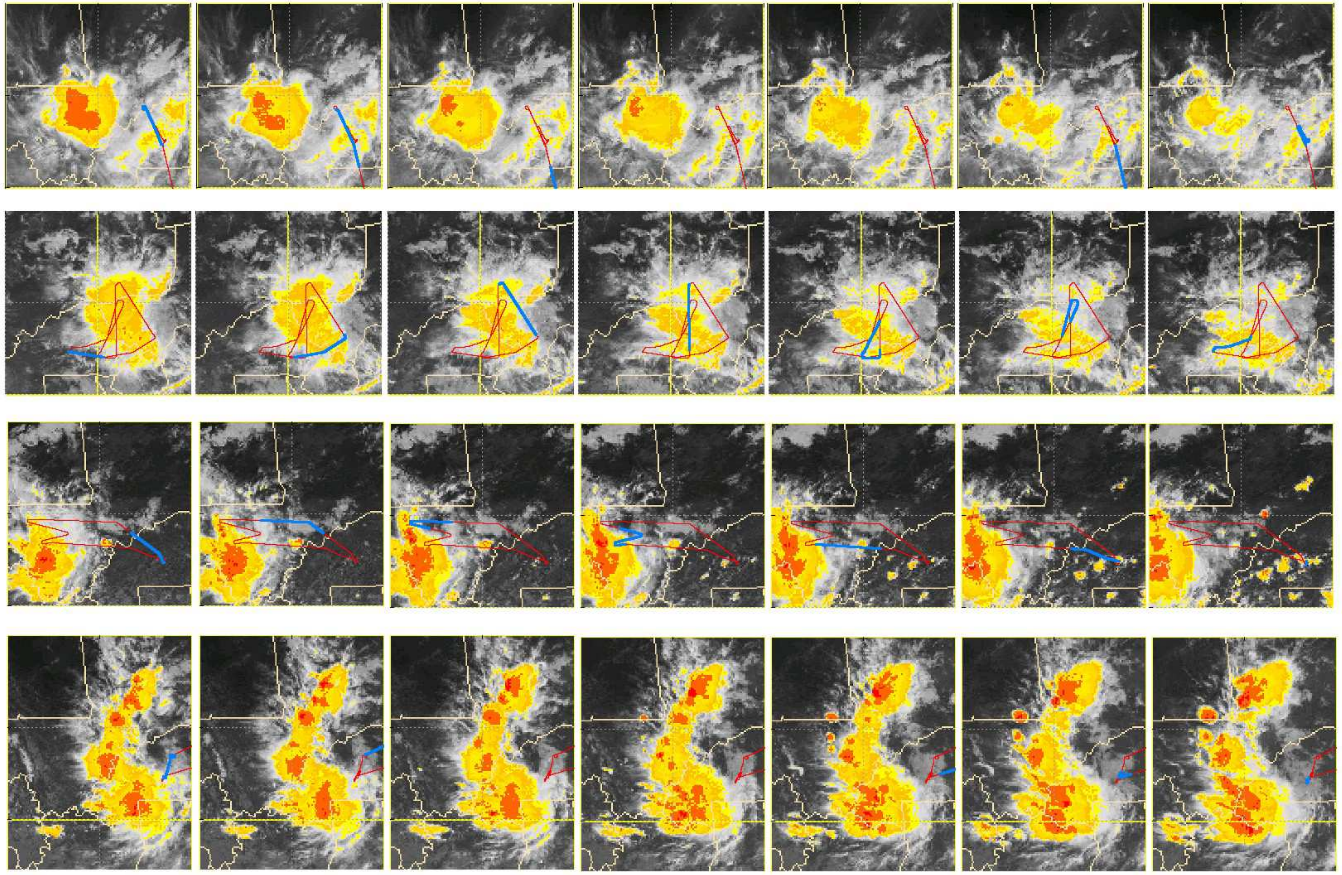

Figure C.10: MCS flights during AMMA-SOP, satellite images of cloud top temperatures: August 4th (top), August 6th (second), August 7th (third), August 11th (bottom). The satellite images can be found on the AMMA website *(http://www.isac.cnr.it/∼utls/m55amma/)*. The colorscale denotes CTT < 225 K (yellow), < 210 K (orange), < 195 K (red). The time interval between two images is 30 minutes. The size of each satellite image covers 10° in latitude and longitude, which corresponds to 1080×1080 km ($10° \times 15° = 1080 \times 1620$ km for August 11th). The flight track of the research aircraft is shown in red, the blue sections mark the location of the aircraft during the first section of each flight.

Bibliography

[Ackerman et al., 2004] Ackerman, A., Kirkpatrick, M., Stevens, D., and Toon, O. (2004). The impact of humidity above stratiform clouds on indirect aerosol climate forcing. *Nature*, 432:1014–1017.

[Bandy et al., 1993] Bandy, A., Thornton, D., and Driedger III, A. (1993). Airborne measurements of sulfur dioxide, dimethyl sulfide, carbon disulfide, and carbonyl sulfide by isotope dilution gas chromatography/mass spectrometry. *J. Geophys. Res.*, 98:23423–23433.

[Berresheim et al., 1995] Berresheim, H., Wine, P., and Davis, D. (1995). *Composition, Chemistry and Climate of the Atmosphere*, chapter Sulfur in the Atmosphere. Van Nostrand Reinhold, New York.

[Bluth et al., 1993] Bluth, G., Schnetzler, C., Krueger, A., and Walter, L. (1993). The contribution of explosive volcanism to global atmospheric sulphur dioxide concentrations. *Nature*, 366:327–329.

[Brahic, 2006] Brahic, C. (2006). Waiting for the monsoon. *Science*, 313:608–609.

[Brasseur et al., 1999] Brasseur, G., Orlando, J., and Tyndall, G. (1999). *Atmospheric Chemistry and Global Change*. Oxford University Press, New York.

[Cooper et al., 2004] Cooper, O., Forster, C., Parrish, D., Trainer, M., Dunlea, E., Ryerson, T., Hübler, G., Fehsenfeld, F., Nicks, D., Holloway, J., Gouw, J. d., Warneke, C., Roberts, J., Flocke, F., and Moody, J. (2004). A case study of transpacific warm conveyor belt transport: Influence of merging airstreams on trace gas import to north america. *J. of Geophys. Res.*, 109.

[Draxler and Hess, 1998] Draxler, R. and Hess, G. (1998). An overview of the hysplit4 modelling system for trajectories, dispersion, and deposition. *Australian Meteorological Magazine*, 47:295–308.

[Draxler and Rolph, 2003] Draxler, R. and Rolph, G. (2003). *HYSPLIT (HYbrid Single-Particle Lagrangian Integrated Trajectory), Model access via NOAA ARL READY Website (http://www.arl.noaa.gov/ready/hysplit4.html).*

[Fiedler, 2004] Fiedler, V. (2004). The Atmospheric Aerosol Precursur Gas Sulfuric Acid: Mass Spectrometric Measurements in the Atmospheric Boundary Layer in Finland and Germany. Diplomarbeit, Universität Heidelberg.

[Giglio et al., 2003] Giglio, L., Descloitres, J., Justice, C., and Kaufman, Y. (2003). An enhanced contextual fire detection algorithm for modis. *Remote Sensing of Environment*, 87:273–282.

[Giles, 2006] Giles, J. (2006). Meteorologists pour into west africa. *Nature*, 442:496.

[Graf et al., 1997] Graf, H.-F., Feichter, J., and Langmann, B. (1997). Volcanic sulfur emissions: Estimates of source strength and its contribution to global sulfate distribution. *J. Geophys. Res.*, 102:10727–10738.

[Hanke, 1999] Hanke, M. (1999). *Development of a Novel Method for Measuring Atmospheric Peroxy Radicals: Calibration, Aircraft-Borne Measurements and Speciated Measurements of HO_2 and RO_2.* PhD thesis, University of Heidelberg.

[Houze Jr., 2004] Houze Jr., R. (2004). Mesoscale convective systems. *Rev. Geophys.*, 42.

[Jost et al., 2003] Jost, C., Trentmann, J., Sprung, D., Andreae, M., McQuaid, J., and Barjat, H. (2003). Trace gas chemistry in a young biomass burning plume over namibia: Observations and model simulations. *J. Geophys. Res.*, 108.

[Kulmala, 2003] Kulmala, M. (2003). How particles nucleate and grow. *Science*, 302:1000–1001.

[Lebel et al., 2005] Lebel, T., Redelsperger, J.-L., and Thorncroft, C. (2005). *The International Science Plan for AMMA, Website (http://amma.mediasfrance.org/international/documents/index).* Paris.

[March and Hughes, 1989] March, R. and Hughes, R. (1989). *Quadrupole Storage Mass Spectrometry.* John Wiley & Sons, New York.

[Olivier and Berdowski, 2001] Olivier, J. and Berdowski, J. (2001). Global emission sources and sinks. In Berdowski, J., Guicherit, R., and Heij, B., editors, *The Climate System*, pages 33–78. A.A. Balkema Publishers/Swets & Zeitlinger Publishers, Lilsse, The Netherlands.

[Paul and Raether, 1955] Paul, W. and Raether, M. (1955). Das elektrische massenfilter. *Zeitschrift für Physik*, 140:262–273.

[Penner, 2004] Penner, J. (2004). The cloud conundrum. *Nature*, 432:962–963.

[Ramanathan et al., 2001] Ramanathan, V., Crutzen, P., Kiehl, J., and Rosenfeld, D. (2001). Aerosols, climate, and the hydrological cycle. *Science*, 297:2119–2124.

[Reiner and Arnold, 1994] Reiner, T. and Arnold, F. (1994). Laboratory investigations of gaseous sulfuric acid formation via $so_3 + h_2o + m \rightarrow h_2so_4 + m$: Measurement of the rate constant and product identification. *J. Chem. Phys.*, 101:7399–7407.

[Roedel, 1994] Roedel, W. (1994). *Physik unserer Umwelt — die Atmosphäre.* Springer Verlag, Berlin.

[Seinfeld and Pandis, 1998] Seinfeld, J. and Pandis, S. (1998). *Atmospheric Chemistry and Physics.* John Wiley & Sons, New York.

[Sorokin et al., 2006] Sorokin, A., Arnold, F., and Wiedner, D. (2006). Formation and growth of sulfuric acid–water cluster ions: Experiments, modelling, and implications for ion-induced aerosol formation. *Atmospheric Environment*, 40:2030–2045.

[Speidel, 2005] Speidel, M. (2005). *Atmospheric Aerosol Particle Formation: Aircraft-Based Mass Spectrometric Measurments of Gaseous and Ionic Aerosol Precursors.* PhD thesis, University of Heidelberg.

[Stohl et al., 2006] Stohl, A., Forster, C., Huntrieser, H., Mannstein, H., McMillan, W., Petzold, A., Schlager, H., and Weinzierl, B. (2006). Aircraft measurements over europe of an air pollution plume from southeast asia - aerosol and chemical characterization. *Atmospheric Chemistry and Physics Discussions*, 6:12611–12670.

[Tu et al., 2004] Tu, F., Thornton, D., Bandy, A., Carmichael, G., Tang, Y., Thornhill, K., Sachse, G., and Blake, D. (2004). Long-range transport of sulfur dioxide in the central pacific. *J. Geophys. Res.*, 109.

[Wang and Crutzen, 1995] Wang, C. and Crutzen, P. (1995). Impact of a simulated severe local storm on the redistribution of sulfur dioxide. *J. Geophys. Res.*, 100.

[Wilhelm et al., 2004] Wilhelm, S., Eickhorn, S., Wiedner, D., Pirjola, L., and Arnold, F. (2004). Ion-induced aerosol formation: new insights from laboratory measurments of mixed cluster ions $\mathrm{hso}_4^-(\mathrm{h}_2\mathrm{so}4)_a(\mathrm{h}_2\mathrm{o})_w$ and $\mathrm{h}^+(\mathrm{h}_2\mathrm{so}4)_a(\mathrm{h}_2\mathrm{o})_w$. *Atmospheric Environment*, 38:1735–1744.

[Wollny, 1998] Wollny, G. (1998). Flugzeugmessungen atmosphrischer Spurengase mittels Ionen-Molekl-Reaktions-Massenspektroskopie: Methodische Untersuchungen zur Reaktionskinetik. Diplomarbeit, Universität Heidelberg.

[Wutz et al., 2000] Wutz, M., Adam, H., Walcher, W., and Jousten, K. (2000). *Handbuch Vakuumtechnik*. Vieweg, Braunschweig/Wiesbaden, 7 edition.

[Yokelson et al., 2003] Yokelson, R., Bertschi, I., Christian, T., Hobbs, P., Ward, D., and Hao, W. (2003). Trace gas measurements in nascent, aged, and cloud-processed smoke from african savanna fires by airborne fourier transform infrared spectroscopy (aftir). *J. Geophys. Res.*, 108.

[Zeng, 2003] Zeng, N. (2003). Drought in the sahel. *Science*, 302:999–1000.

[Zhao et al., 2006] Zhao, C., Tie, X., Brasseur, G., Noone, K., Nakajima, T., Zhang, Q., Zhang, R., Huang, M., Duan, Y., Li, G., and Ishizaka, Y. (2006). Aircraft measurements of cloud droplet spectral dispersion and implications for indirect aerosol radiative forcing. *Geophys. Res. Lett.*, 33.